REFERENCE ONLY

UNIVERSITY OF LONDON THESIS

Degree PhD Year 2005 Name of Author HOWARTH, C.A

Metal-Ammonia-Fulleride Solutions

University College London

A thesis submitted in accordance with the
requirements of the University of London
for the degree of Doctor of Philosophy

Christopher Anthony Howard

January 2005

ProQuest LLC
789 East Eisenhower Parkway
P.O. Box 1346
Ann Arbor, MI 48106-1346

Abstract

This project is the first concerted effort to study the structure of metal-ammonia-fulleride solutions. These novel solutions contain high concentrations of fulleride anions, C_{60}^{n-} (n = 1 to 5). A detailed understanding of the solubility of fullerenes and their derivatives has long been sought after: something this project addresses. The work focuses on the structure of the solutions using the complementary techniques of wide angle neutron diffraction, Small Angle Neutron Scattering (SANS), and Monte Carlo simulations. A highly developed structure is found over the short and intermediate length scales. The results show concentrated solutions of solvent separated, strongly coordinated, fulleride anions, maintained by an intriguing reorganisation of the ammonia solvent around the anions in solution.

In more detail, we find two solvation shells around the C_{60} anions containing around ~45 and ~80 ammonia molecules respectively. The ammonia solvent molecules direct one of their hydrogen atoms towards the centre of the C_{60} anions, allowing the other two hydrogen atoms to complete hydrogen-bonds within and across the shells. The solvation structure of the cation in solution is found to be very similar to its solvation structure in bulk metal-ammonia solutions. The structure and stability of the solutions is found to be dependent on both anionic charge and cation charge density.

The scientific importance of the solutions is demonstrated by the attainment of high quality ^{13}C NMR spectra for the fulleride anions C_{60}^{n-} (n = 1 to 5) for the first time in an identical solvent. Previous limitations of low concentrations, poor quality samples, and restrictions due to the air sensitivity of the anions have been overcome. The data here includes the first ^{13}C NMR spectrum of C_{60}^{5-}. These data reveals that all the carbon atoms have an identical electronic environment in this anion.

Acknowledgements

I would like first and foremost to thank my supervisor Neal Skipper for his guidance, encouragement and friendship over the course of my PhD. A big thank you must also go to Jonathan Wasse and Helen Thompson for their help, expertise and advice throughout.

Particular mention must also be given to Tom Weller for his inspirational, daily enthusiasm for science and to Cecilia Gejke, Arthur Lovell and Mark Ellerby for their friendship and assistance on experiments and in the laboratory. Also thanks to Hayley Spiers, Jon Allen, Helen Walker, Ross Springell and Eamonn Beirne at UCL.

I would like to thank the instrument scientists and sample environment staff who have helped me in this work: Daniel Bowron, Alan Soper, Richard Heenan, Steve King, John Dreyer, Chris Goodway and Mike Yates at ISIS, and Charles Dewhurst and Pierre Palleau at the ILL. Thanks also to Peter Edwards, Matt Lodge and Nick Rees at Oxford for their help with the NMR measurements. I would also like to thank Merck Chemical Ltd. for a CASE award and to Rod Riddle for his help and advice.

Finally, I must thank my parents for their unconditional support and encouragement throughout my life. And, of course, a big special thank you to Debbie White for her unstinting patience, good spirit, friendship and love.

Contents

List of Figures

List of Tables

Introduction

Until Buckminster fullerene, C_{60}, was discovered in 1985 there were only two known allotropes of carbon: graphite and diamond. Since then a plethora of new carbon molecules have been identified, including carbon nanotubes, carbon onions, and many other fullerenes and fullerene derivatives. These new molecules provide us with a rich variety of electronic properties, extensive and varied potential for doping, and numerous derivatives. Many exciting applications have been suggested for fullerenes, including their use in 'bottom-up' nanotechnology, hydrogen storage, solar panels, and superconductors. However, fullerene science is still in its early days, and many fundamental questions still remain to be answered.

A key area of research for the advancement of fullerene science is the study of the solution chemistry and the solvation properties of fullerenes and their derivatives. In particular, fundamental understanding and control of fullerene solutions is required to establish new protocols for characterisation, separation and purification of these molecules. Concentrated, monodisperse solutions of fullerenes are desirable for these techniques, as well as for large scale deposition and processing. In this context a pressing problem is that many fullerenes do not dissolve to high concentrations in common solvents, and tend to form fractal

aggregates in solution.[1,2,3] The lack of suitable solvents becomes more acute for larger carbon nanoparticles. Carbon nanotubes, for example, can only be dispersed in solution by damaging chemical funtionalisation, sonication or strong oxidation.[4]

An important new route to dissolution exploits metal-ammonia solutions.[5] It has been shown that fullerene C_{60} is sequentially and reversibly reduced to C_{60}^{n-} (n = 2 to 5) with increasing metal, and hence electron, concentration in these solutions.[6] The resulting fulleride anions then dissolve to high concentrations. These solutions have been exploited as an intermediate (catalytic) stage in forming the topical A_3C_{60} superconductors (where A = K, Rb, Cs).[7,8,9] However, there has been no concerted attempt to study or characterise the parent solutions themselves. This is even more surprising when one considers that they offer a unique arena in which to study fulleride solvation in a concentrated (colloidal) environment.

This project forms the first systematic effort to understand and exploit metal-ammonia-fulleride solutions. The main aim is to establish the microscopic structure and in particular, the way in which the fullerides are accommodated within the solutions. Key questions centre on the mechanisms of dissolution, and the tendency to form monodisperse or aggregated systems. Here we can exploit controllable parameters such as fulleride charge and cation radius to investigate the subtle balance between the various interactions at play in these solutions. For example; hydrogen-bonding, cation and fulleride solvation, and cation-fulleride pairing.

Scope of Thesis

This thesis presents the first structural studies of metal-ammonia-fulleride solutions. The results have led to a detailed understanding of the solution structure and its dependence on the parameters of fulleride charge and cation charge density.

Wide angle neutron diffraction with isotope substitution has been used to directly measure the microscopic structure. Empirical Potential Structural Refinement (EPSR) analysis of the experimental data has revealed in detail the nature of the fulleride solvation and the inter-solvent structure. This provides new insight into the network of hydrogen-bonds which form to accommodate the fullerides. Small Angle Neutron Scattering (SANS) techniques are employed to investigate the inter-fulleride structure in the solutions.

The experimental results are complemented by classical Monte Carlo (MC) computer simulations. I find close agreement between the simulation and neutron data which demonstrates the suitability of the effective pair potentials selected to investigate the solutions. The simulations are then used to examine the structural dependence on anion charge and species of cation.

Finally, the application of the solutions as a medium for studying discrete fullerides is demonstrated. The first ^{13}C solution NMR shift of the C_{60}^{5-} is measured. A set of fulleride anion NMR spectra (n = 1 to 5) has been measured in an identical solvent for the first time. The quality of the data is significantly better than any ^{13}C spectra of the anions previously reported, and will therefore open up the possibility of the first detailed study of the magnetic and electronic properties of the isolated fulleride anions.

Chapter 1

Background and Motivation

This section aims to brief the reader in the fields applicable to this work, and to introduce the scientific and technological motivation for studying metal-ammonia-fulleride solutions. The chapter reviews the relevant aspects of fullerene science, explains the potential applications of fullerenes, and the importance of solution studies.

1.1 C_{60} Structure

Since its discovery in 1985,[10] Buckminster fullerene C_{60} has been the subject of intensive study and has produced much interesting science.[7,9,11,12] As the third allotrope of carbon, C_{60} automatically generated huge interest. This was augmented by interest in its photogenic high symmetry, cage-like structure, and rich doping potential. The award of the 1996 Nobel Prize for Chemistry[13] is recognition of how these newly discovered molecules have enthused science.

C_{60} has a molecular diameter of approximately 7.0Å,[14] and electronic wavefunctions extending inside and outside by another 1.5Å.[9] It is therefore viewed as a building block of nanotechnology. Essentially a graphene sheet curved in on itself, the fullerenes are an example of a self-contained 2-dimensional surface. All the fullerenes have 12 pentagonal carbon rings, which are responsible for their curvature; it is the number of hexagons carbon rings that change. The C_{60} has 20 hexagons with all pentagons surrounded by five hexagons (see Figure 1.1), making it the most regular and stable of the fullerene family. In fact, the structure is identical to a traditionally stitched soccer ball. Of the 90 edges, the pentagon bond lengths are identical and the hexagons consist of alternate double and single bond lengths (1.40 Å and 1.45 Å).[15,16] There are 30 short 'double bonds' that join two hexagons and 60 longer 'single bonds' that join the hexagon to the pentagon. C_{60}'s symmetry can be well described by a truncated icosahedron.

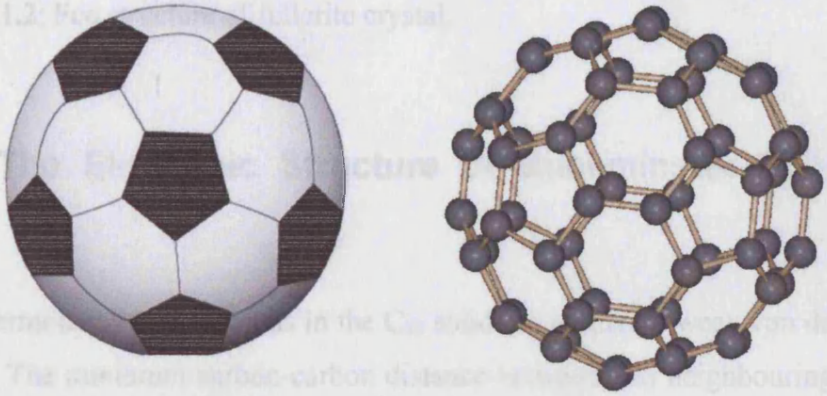

Figure 1.1: The molecular 'soccer ball' structure of C_{60}.

In the crystalline solid, the C_{60}s adopt a face-centred cubic structure,[16,17] with lattice parameter 14.198Å and fullerene separation 10.02Å (see Figure 1.2). The C_{60}s themselves are in almost free rotation about their well defined centres of mass at room temperature. Upon cooling to about 260K, there is a phase transition to an orientationally ordered phase in which the C_{60}s sit in one of two orientational positions, this is known as merohedral disorder.[18] There are three

relatively large interstitial sites per C_{60} in this fcc structure, permitting the accommodation of various dopant atoms[19] (see section 1.8).

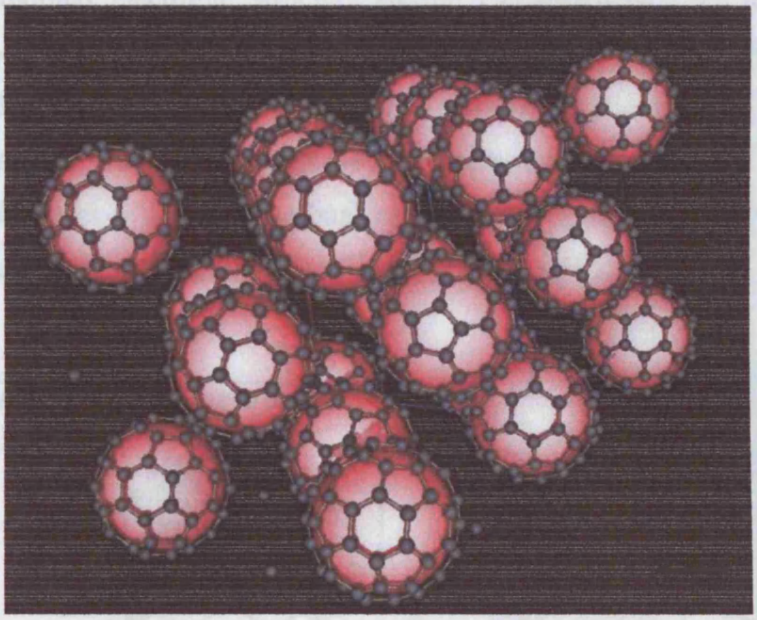

Figure 1.2: Fcc structure of fullerite crystal.

1.2 The Electronic Structure of Buckminster Fullerene, C_{60}

The intermolecular interactions in the C_{60} solid are relatively weak van der Waals forces. The minimum carbon-carbon distance between two neighbouring C_{60}s in the fullerite crystal is about 3Å, as opposed to the 1.4Å nearest intramolecular bond distances. The electronic structure of solid C_{60} and C_{60} compounds are therefore largely determined by the electronic levels of the C_{60} molecule itself.[7,9]

Carbon atoms have 4 valence electrons: $(1s^2)2s^22p^2$. Each carbon atom is bonded to 3 neighbours by σ-bonds similar to those found in graphite. These lay 3-6eV below the Fermi level. The remaining 60 electrons occupy π-orbitals, again analogous to those in graphite. Due to the curvature of the ball, however, these electrons tend to spend more time outside the cage than inside.[9] Another

difference to graphite is that the electrons are not truly delocalised around the six-member rings, due to the fact that the C-C bond lengths are not uniform. These key differences to graphite, and in particular the curvature of the C_{60}, give rise to the rather individual electronic structure of the C_{60} molecule. In the first molecular calculations of the C_{60} molecule, Haddon *et al.* showed that this curvature explains the electronic structure and high electron affinity of 2.7eV. This value was later found by gas phase measurements to be 2.69eV.[20] The results from the Hückel molecular orbital calculations[21] and the corresponding electronic band structure of the fullerite solid are shown in Figure 1.3.

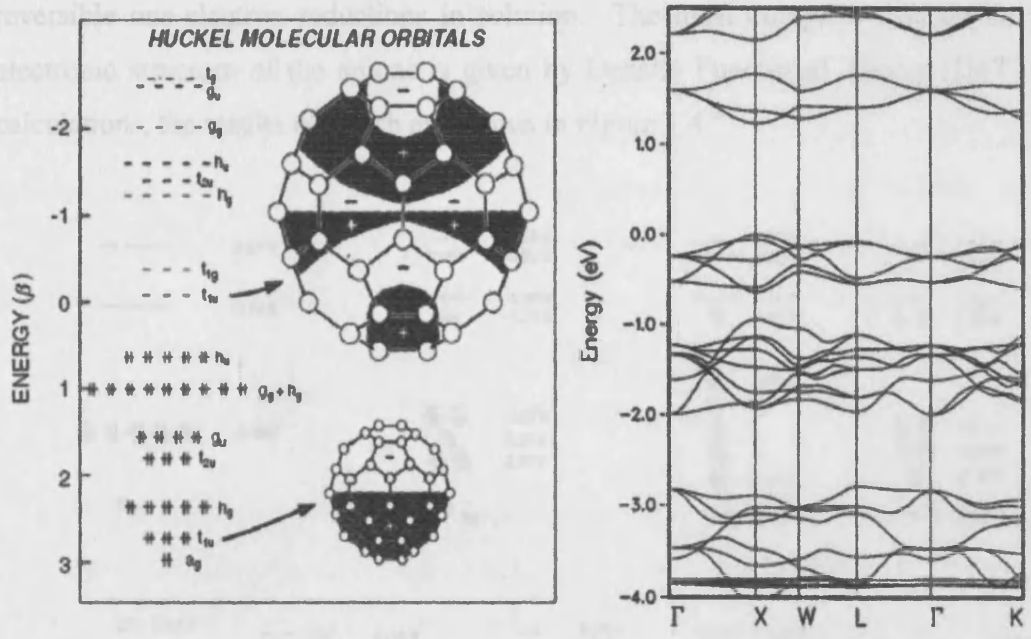

Figure 1.3: Electronic structure of molecular C_{60} from ref [21] and corresponding band structure of fcc solid fullerite from ref [22].

The highest occupied molecular orbital (HOMO) is 5 fold degenerate and completely filled. The lowest unoccupied molecular orbital (LUMO) is triply degenerate. This is followed by another triply degenerate orbital. The presence of the relatively low lying LUMO led to the prediction that C_{60} would be a good electron acceptor. The origin of these two orbitals can be qualitatively understood

as follows: the 12 five membered rings can perhaps be thought of as the origin of 'electron deficient' sites.

In the fcc solid, much of the molecular electronic structure survives: the orbitals near the Fermi level (HOMO and LUMO) form narrow and non-overlapping bands. The distance between the HOMO and LUMO bands is about 1.5eV.[23] The width of the LUMO band is about 0.5eV. The electron accepting nature of the C_{60} solid is perhaps confirmed most clearly by the existence of the A_nC_{60} solids n = 1 to 6 (where A is an alkali metal). This was also beautifully demonstrated electrochemically. Xie *et al.*[24] showed six successive, fully reversible one-electron reductions in solution. The most complete data on the electronic structure of the anions is given by Density Functional Theory (DFT) calculations, the results of which are shown in Figure 1.4.[25]

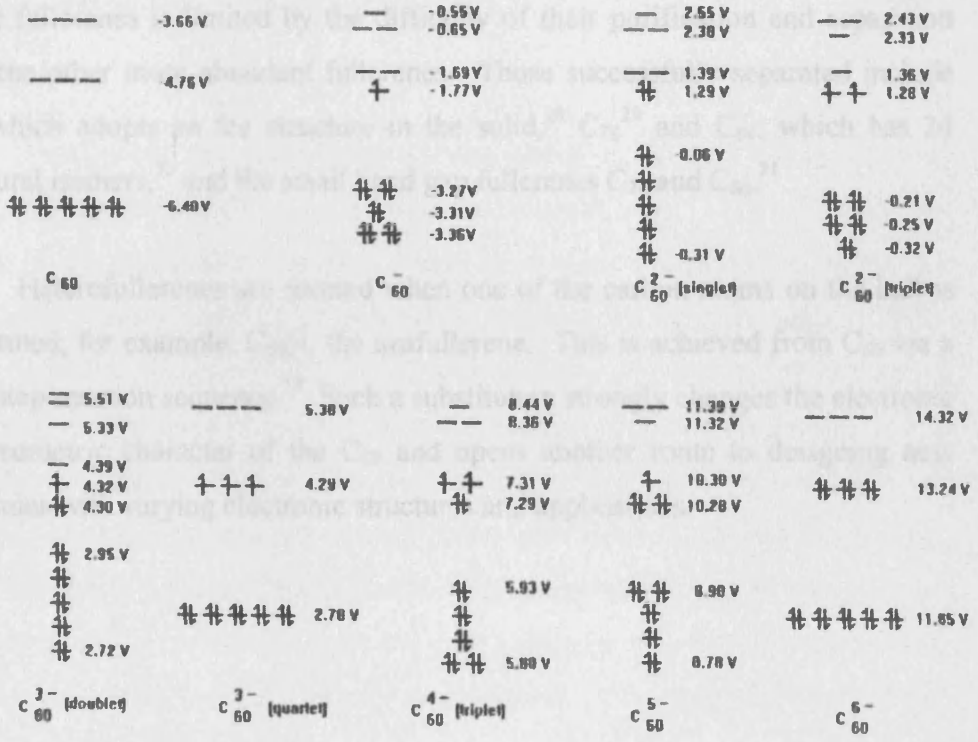

Figure 1.4: Calculated electronic orbital energy patterns of the C_{60} anions from ref [25].

The DFT calculations predict that as electrons are added, all of the fulleride anions undergo Jahn-Teller distortions from the icosahedral symmetry of the C_{60} to lower their symmetry and remove the degeneracy. However, the structural distortions are shown to be subtle and are difficult to detect experimentally.[3] The small size of the distortions is attributed to the rigid nature of the C_{60} and its even distribution of atoms.[25] The 'HOMO-LUMO' gap for all the anions is ~1.1eV.[25]

1.3 Higher Fullerenes and More New Allotropes of Carbon

Since the discovery of fullerene C_{60}, many other fullerenes have been predicted and/or discovered.[26] Inserting an equatorial belt of 10 extra carbon atoms into the C_{60} forms the 'rugby ball' C_{70},[27] which is the next most abundant fullerene formed in the current production methods. Although potentially exciting, the study of higher fullerenes is limited by the difficulty of their purification and separation from the other more abundant fullerenes. Those successfully separated include C_{76}, which adopts an fcc structure in the solid,[28] C_{78}[29] and C_{84}, which has 24 structural isomers,[30] and the small band gap fullerenes C_{74} and C_{80}.[31]

Heterofullerenes are formed when one of the carbon atoms on the ball is substituted, for example, $C_{59}N$, the azafullerene. This is achieved from C_{60} via a three step reaction sequence.[32] Such a substitution strongly changes the electronic and geometric character of the C_{60} and opens another route to designing new molecules with varying electronic structures and applications.

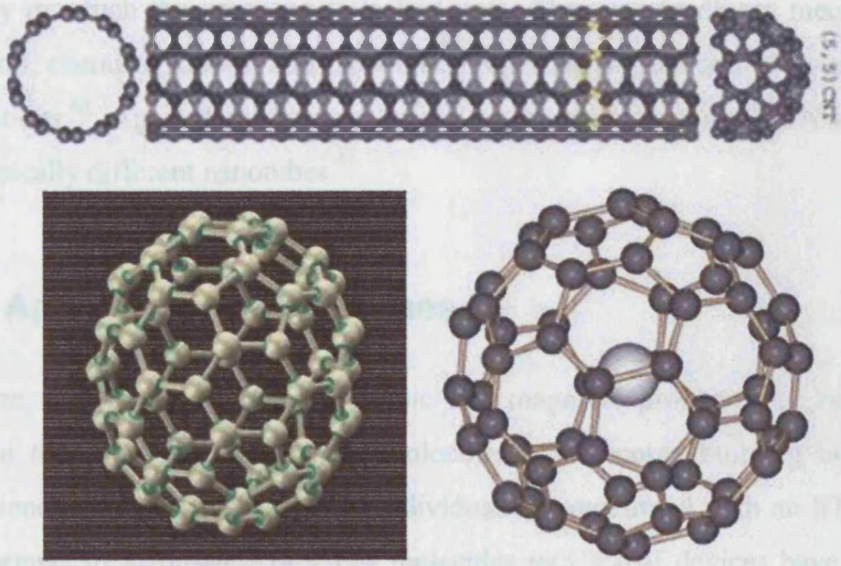

Figure 1.5: Carbon nanostructures: single walled carbon nanotube (top), from ref [33], C_{70} (bottom left), $Li@C_{60}$ (bottom right).

Another class of fullerene is the endohedral fullerene. This is when an atom or atoms are actually situated inside the fullerene cage. La,[34] Sc, Ce, Pr, Ca, Sr, Ba, N, Li, endohedral fullerenes[35] have been made (based mainly on the C_{82} molecule). The enclosed atoms either form bonds to the fullerene cage, or freely reside inside the fullerene. Endohedral fullerenes are produced by either forming fullerenes in the presence of the metallic species, or by implantation.[36] The separation of the endohedral fullerenes from the resulting soot is difficult and typically involves the slow process of high-performance liquid chromatography. The endohedral fullerene $N@C_{60}$[37] has been proposed as a qubit for quantum computing. The fullerene cage not only shelters the nitrogen atom from extraneous charges but also permits manipulation. The long electron spin life times and sharp resonances of these molecules have led quantum computing groups to investigate it for use as a potential qubit.[38]

Single walled nanotubes[39] are possibly the most important new carbon allotrope. Essentially, these consist of a rolled up graphene sheet capped with two

half fullerenes. The electronic properties of these molecules are determined by the way in which the graphene is 'rolled up'. Their extraordinary mechanical, structural, chemical, optical and electronic properties suggest numerous potential applications.[40] Again the science is limited by the separation and purification of electronically different nanotubes.[41]

1.4 Applications of Fullerenes

The size, structure, chemical, electronic and magnetic properties of fullerenes leads to the expectation that these molecules will become building blocks of nanoscience. C_{60} molecules can be individually manoeuvred with an STM tip[42] and attempts to manipulate fullerene molecules into actual devices have yielded encouraging results: a single-molecular electromechanical amplifier[43] and a three electrode, single molecule transistor.[44] Isolated endohedral fullerenes are showing potential as qubits for quantum computers.[38]

Thin films of C_{60} have potential as solar cells[45] and thin films of superconducting doped fullerenes offer an arena for exploring 2D transport properties, and may perhaps form the basis of future circuits. The rich doping potential of fullerenes and the ease of their functionalisation have already yielded a vast number of derivatives. Other applications of C_{60} include lubrication,[46] diamond formation,[47] in solution as optical limiters,[48] hydrogen storage, oxygen detection, and strengthening metals.[49]

1.5 Motivation for Solution Studies of Fullerenes

This thesis focuses on solutions of fullerene anions. The motivation for this research is given in this section.

1.5.1 Separation/Purification of Fullerenes

Although C_{60} was discovered in 1985, it was not until five years later that the real explosion in experimental work on the fullerenes started. The process of forming C_{60} involves evaporating graphite electrodes with a discharge current.[7] The product from this process is a mixture of various carbon structures and fragments. Krätschmer *et al.* discovered that C_{60} dissolved in benzene,[50] albeit to only 1.5mg/ml.[2] This allowed workable quantities of solid 'fullerite' crystal to be precipitated from the dark red solution. Macroscopic amounts of C_{60} crystals were now available. The importance of this result demonstrates the significance of the solution study of fullerenes and their derivatives.

Current methods of producing fullerenes result in a mixture of products. Sorting this mix is not only difficult for the fullerene C_{60}, but needs to be developed further in order to sort out mixtures of other new allotropes of carbons. The main technique currently employed to separate the fullerenes is chromatography. This method is sufficiently efficient for purification of C_{60} and C_{70} which are by far the most abundant fullerenes in the product mix. However, studies into many interesting new types of carbon molecule, such as the larger fullerenes, are hindered by low yields and a slow purification processes. If we can control and understand the dissolution process, it will lead to cheaper and larger scale separation processes, as well as providing useful quantities of the understudied fullerene derivatives and carbon nanoparticles. The presence of the solvated electrons in metal-ammonia-fulleride solutions means that there is a strong possibility of the selectivity of the dissolution of fullerenes based on electronic charge. For example, if a mixture of two types of fullerenes were added to metal-ammonia solutions, the molecule with the highest electron affinity may preferentially pick up the electrons and then dissolve. The solution could be separated from the non-dissolving residue and the ammonia and metal removed by evaporation.

1.5.2 Chemical Manipulation

Metal-ammonia-fulleride solutions have been used to prepare alkali metal-fullerides salts.[7,8,9] This technique extends to other fulleride salts which incorporate metals soluble in liquid ammonia, for example ytterbium, europium and calcium. Preparing solutions of concentrated, controllably charged fulleride anions also allows the introduction of surfactants to the C_{60} or functionalising them completely. This could be important in the synthesis of new fullerene derived molecules. For example, surfactants can be added to C_{60} resulting in molecules which form self-assembled monolayers on water for use in Langmuir-Blodgett deposition techniques.[51,52] The C_{60} can be thought of as a molecular 'pin cushion' for the design of new molecules. An important early example was the preparation of a diamido diacid diphenyl fulleroid derivative designed to inhibit an HIV enzyme.[53,54] This work has further emphasised the need for a detailed understanding for fullerene solvation, and many attempts to functionalise C_{60} have aimed to water solubilise the molecule by introducing hydrophilic chains (see section 1.6.2). A review of fullerene functionalisation is found in ref [55].

1.5.3 Thin Film Deposition

For the next generation of nanodevices, ordered, robust, thin films deposited on desired electrode surfaces are required and, to this end, thin films of fullerenes have been studied with keen interest.[56] The optical properties of C_{60} and the size of its semi-conducting band gap suggest that fullerene films can be used for solar cells.[57] The doping possibilities offer the attractive possibility of conducting thin films with tuneable electronic properties: from semiconducting to superconducting. Many surfaces have been shown to be suitable substrates: Au(111), Ag(111), Ga(110), Si(111), Si(100), Cu(111), Mica, Graphite, CdS, CdSe, MoSc to name a few.[58] A high degree of molecular order has been achieved on Highly Oriented Pyrolytic Graphite (HOPG), and impressively on a self-assembled alkylthiol monolayer (see Figure 1.6)[59,60]

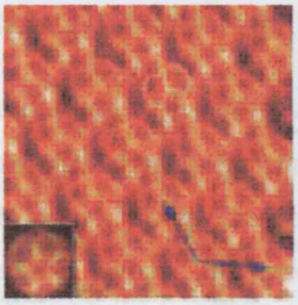

Figure 1.6: STM image of 2D C_{60} crystal formed on an alkylthiol monolayer from ref [60]. Taken at 2K the C_{60} cage structure is clearly visible.

High integrity C_{60} films have only been produced by careful evaporation of the solid. A bulk scale method would be required if fullerene films were to be used on a larger scale. Drop coating, solution based methods yield more porous and less uniformly structured films than the technique of vapour deposition, thought to be due to C_{60} cluster formation in solution,[61] as well as strong surface forces upon evaporation.[51]

Metal-ammonia-fulleride solutions have potential as a means to deposit thin fullerene/fulleride films. This could be done by electrochemical deposition from solution[62] or simply by drop coating directly onto the desired surface.[56] If the solutions studied here consist of high concentrations of solvent separated fullerides, they may be suitable for use in such techniques. Put simply, the solutions have potential to act as paints. The technique of 'colloidal deposition' has been recently proposed as a method to permit the up-scaling of the manufacture of thin films using, for example, epitaxial growth from solution on surfaces.[63,64] Patterned surfaces and careful control of electric fields have been shown to allow 2D controlled deposition,[65,66] e.g., of gold colloidal particles (diameter – 16nm). Similar results have been obtained by simply using solvent evaporation of colloidal solutions.[67]

1.5.4 A Medium for Studying Fulleride Ions

It has been suggested that because of the small ball-ball overlap in the C_{60} solids and salts, the purest way of understanding the properties of these compounds is by studying the isolated fulleride anions.[3] Data from the discrete ions, in solution or in a glassy state, would reflect the intrinsic properties of non-interacting fulleride ions. A major limitation in doing this is the difficulty in finding suitable solvents in which the fullerides do not aggregate as well as being concentrated enough to study. On top of this, the solvent needs to be impurity free and, in particular, isolated from oxygen and water.[3] There have been several attempts to measure the ^{13}C Nuclear Magnetic Resonance (NMR) spectra of the fulleride anions in solution,[3] but the investigation has been limited. The NMR spectra of the fullerides have been studied in different solvents and results from the different fullerides are difficult to compare. The NMR peaks themselves are very small and poorly defined, and the sought after C_{60}^{5-} shift has never been obtained.[3]

A direct measure of the magnetic properties of the discrete ions could also be studied in a glassy state. If the solutions could be quenched to form glassy solids, these could then be studied with a sensitive magnetic probe such as a Superconducting Quantum Interference Device (SQUID).

1.6 Fullerenes in Solution: Previous Work

There has been a concerted effort to investigate the solubility behaviour of fullerenes, and this is well reviewed elsewhere.[2] Until the discovery of C_{60}, pure carbon itself was insoluble. After Krätschmer's discovery, the first work of importance was the by Ruoff *et al.*, who measured a maximum in the temperature dependence of C_{60} solubility in several solutions.[1,68] This behaviour can be explained if it is considered that fullerenes tend to form clusters in solutions. This maximum has been observed in several different solutions of C_{60}.[2] Further evidence for cluster formation is the observed solvochromatic effect: a drastic change in optical/Raman spectra on increase of temp/concentration, as well as further evidence from diffusion studies.[2] Most of these experiments are

conducted in solutions of C_{60} with solvent molecules containing 6-memembered rings such as benzene, as these solvents have been found to dissolve C_{60} to higher concentrations than other solvents. It has been suggested that a magnetic interaction between ring currents in such a solvent molecule and the fullerene itself causes of the formation of these aggregates.[2] The specific surface energy for such an interaction is the same order of magnitude as the interaction energy of neighbouring C_{60}s. Although C_{60} itself seems to be almost insoluble in polar solvents,[2] dissolution of the charged fullerides in such solvents may prove more fruitful. For charged fullerenes there is little data other than electrochemical data, due perhaps to the reactivity of the fullerides with oxygen and water.[3] Table 1.1 gives a list of the solubility of C_{60} in various solvents, including the most soluble, 1,2,3,5-tetramethylbenzene.

Solvent	**Solubility of C_{60} (mg/ml)**
1,2,3,5-tetramethylbenzene	20.80[69]
Toluene	2.90[69]
Benzene	1.50[69]
Chloroform	0.16[70]
n-hexane	0.043[70]
Methanol	0.000035[71]
Water	1.3×10^{-11} [71]

Table 1.1: The solubility of C_{60} in various solvents.

1.6.1 Routes to Solubilisation

There has been a keen recent agenda to find suitable solvents or methods for the dissolution of fullerenes. Water soluble derivatives have been made by attaching polymer chains.[72] Solubilisation has also been attempted by using more than one solvent,[73] and by mixing different types of fullerene in solution.[74] Although these methods have shown some success, the concentrations still remain low and aggregates are still present in many of the resulting dispersions.

Solubilisation in the charge state has not been thoroughly investigated. However, this process was used to isolate the small band gap fullerenes (C_{74}, C_{80}).[31] These fullerenes are kinetically unstable and react upon formation to form polymerised, insoluble solids. Researchers managed to use electrochemical reduction in order to break the bonds and hence solubilise the fullerenes. This permitted their extraction and isolation.[31]

1.7 The Route to Dissolution

Metal-ammonia-fulleride solutions are formed in a two step process. First, an alkali metal is dissolved in liquid ammonia. It is in this solution that the fullerite C_{60} crystal is then reduced and consequently dissolves.

1.7.1 Metal-ammonia Solutions

As long ago as 1808,[75] it was found that alkali metals dissolved in liquid ammonia to form solutions with extraordinary properties. We now know that the alkali metals' valence electrons dissociate in solution and become solvated by the ammonia molecules. This results in the following meta-stable, in solution, reaction:[5]

$$M \leftrightarrow M_s^+ + e_s^-.$$

The presence of the solvated electrons result in solutions with fascinating properties. For example, the metal-amines include the lowest density liquid, liquid metals with higher electronic conductivities than mercury, a metal – non-metal transition and even a suggestion of superconductivity in the glassy solids by Ogg.[5,76,77,78,79] Interestingly, since Ogg's claim made nine years before the BCS theory of superconductivity introduced the idea of electron pairing, evidence for spin paired electrons, as well as other exotic electronic species, have been found.[77,75] Ogg's result, however, has never been repeated.

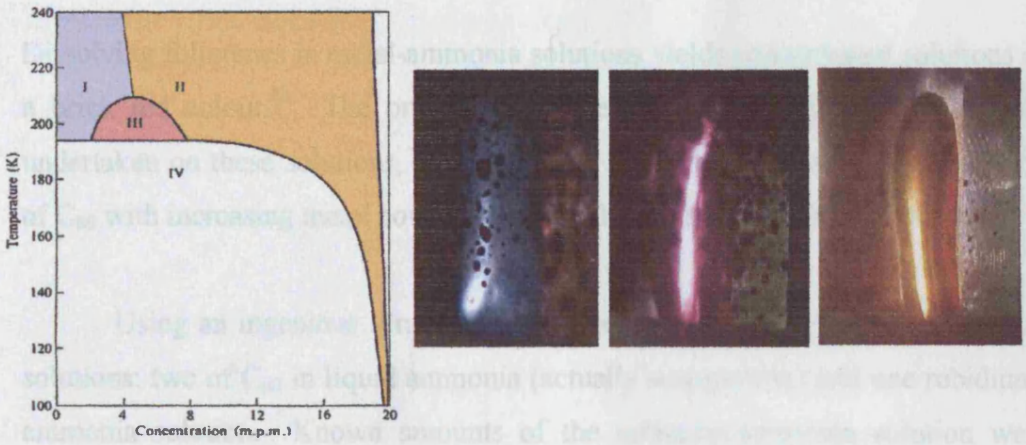

Figure 1.7: Lithium-ammonia phase diagram and photographs of solutions corresponding to the coloured regions I,II and III. Reproduced from ref [80].

This project aims to exploit metal-ammonia solutions as powerful reducing agents due to the presence of the solvated electrons. The solvated electrons give the dilute metal-ammonia solutions their deep blue colour.[5] These solutions are notoriously difficult to make, largely due to the fact that the presence of impurities will cause the solutions to decompose via the following reaction:

$$M_S^- + NH_3 \rightarrow M^+(NH_2^-) + \frac{1}{2}H_2(g).$$

Until recently, the understanding of these solutions was hindered by a dearth of structural data. However, the increasing flux and experimental methods at third generation neutron sources such as ISIS in the UK, has allowed this problem to be addressed. A more detailed understanding of the role of hydrogen-bonding and accommodation of the electronic species has recently been achieved.[81,82,83,85,86]

1.7.2 Metal-Ammonia-Fulleride Solutions: Previous Work

Dissolving fullerenes in metal-ammonia solutions yields concentrated solutions of a brick red colour.[84] The only previous detailed experimental measurements undertaken on these solutions, is proof of the sequential and reversible reduction of C_{60} with increasing metal concentration.[6] This will be explained in detail.

Using an ingenious setup, the experimenters were able to start with three solutions: two of C_{60} in liquid ammonia (actually suspensions) and one rubidium-ammonia solution. Known amounts of the rubidium-ammonia solution were added to one of the other solutions and its IR spectrum was measured. By comparing the results with previously recorded IR spectra, effectively fingerprints for the C_{60} ions, it was found that upon addition of the metal-ammonia solution, the C_{60} is sequentially reduced to C_{60}^{5-}. The C_{60}^{6-} was not seen, however, with the signature spectrum of the solvated electron returning upon further addition of the rubidium-ammonia solution. The IR spectra were so similar to previous measurements (made in dicholormethane, pryridine and benzonitrile) that the authors cited this as evidence for insignificance of cation-anion pairing and solvent effects on the C_{60} anion's electronic structure, although their solutions were relatively dilute. By diluting the solution of C_{60}^{5-} anions with other C_{60}-ammonia mixture, it was shown that the spectrum of the 4-, 3- and 2- were sequentially recovered.

This is key evidence that we can have a homogenous solution of fulleride ions, the charge on the ion depending on the metal, and hence electron concentration, in solution.

1.7.3 Ammonia as a Solvent

Ammonia and other amines are unique in their ability to support electrons. This arises from their propensity to from hydrogen-bonds.[85,86,87] Ammonia can act as a stable solvent for several reactive species, and is used as a catalyst in many

organic synthesis reactions.[88] The structure of ammonia is shown in Figure 1.8. Its physical properties are recorded in Table 1.2.[89]

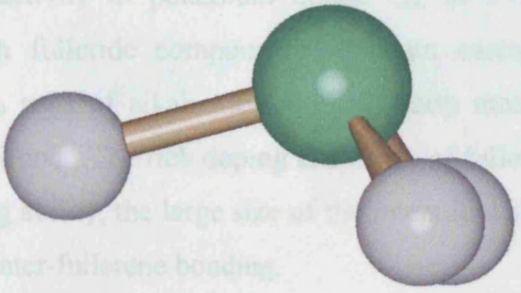

Figure 1.8: A molecular graphics picture of an ammonia molecule.

r_{NH}	1.01Å
r_{HH}	1.62Å
Angle H-N-H	107°
Dielectric Constant, ε	16.5 (at 293K)
Melting Point	195.41K
Boiling Point	239.82K
Density at 240K	0.68g/cm^3
Molecular Weight	17.02g/mol
Dipole Moment	1.847 debye

Table 1.2: Summary of the physical properties of ammonia.[89]

Ammonia molecules complete hydrogen-bonds in the liquid state. An ammonia molecule has only one lone pair to available to accept hydrogen-bonds, which leads to a relatively weak association in the liquid state. The internal energy of ammonia is ~21kJ/mol, approximately half that of water. Recent diffraction experiments show that in liquid ammonia there are, on average, 2.0 hydrogen-bonds per nitrogen atom, with an average N•••H distance of ~2.4Å.[85]

1.8 Doped Fullerenes and Superconductivity

One of the most exciting early papers of fullerene science was the discovery in 1991 of superconductivity in potassium doped C_{60} at 19.2K.[90] Since then, superconductivity in fulleride compounds has been extensively studied and superconducting C_{60} salts of alkali metals, alkali earth metals[91] and rare earth metals[92] have been found. The rich doping chemistry of fullerene C_{60} arises from its electron accepting ability, the large size of the interstitial sites in the solid, and the relatively weak inter-fullerene bonding.

In the case of the alkali metals, it is widely accepted that the metal's valence electron is donated to the t_{1u} band of the fullerite crystal, with the metal cations then situated in the interstitial sites. The geometry of the fcc lattice is such that there are one octahedral and two tetrahedral interstitial sites per C_{60} (sizes 2.06Å and 1.12Å respectively). These are large enough to accommodate many ions and C_{60} has been successfully doped with species other than metals such as iodine.[93] This section concentrates on the alkali metal doped C_{60}s. This is because one of the ways of manufacturing these compounds incorporates the use of alkali metal-ammonia-fulleride solutions. The ammonia is used as a solvent catalyst. Having formed the solutions, the ammonia is subsequently removed leaving behind the C_{60} metal salt. Although this process forms smaller crystals and the solvent can be difficult to remove, there are advantages over the alternative method of intercalation via vapour transport: the ammonia technique can be more easily scaled up, is quicker, and can produce high quality samples if the solvent is sufficiently removed.[7,8,94,95]

If the ratio of metal to C_{60} is 3, then salts are typically formed whereby the fcc structure of fullerite is not altered and the metal ions reside in the interstitial sites. More or less metal ions can be accommodated if there is a lattice reorganisation, typically to either a bcc or bct crystal. The electronic properties of these salts are diverse. As the t_{1u} band is progressively filled, it is intuitive to think that all the salts are metallic up to A_5C_{60}. However, this is not the case and is indicative of non-trivial on ball electron correlations which are not completely

understood. Typical structures of potassium doped fullerides and their electronic properties are shown in Figure 1.9 and Table 1.3.

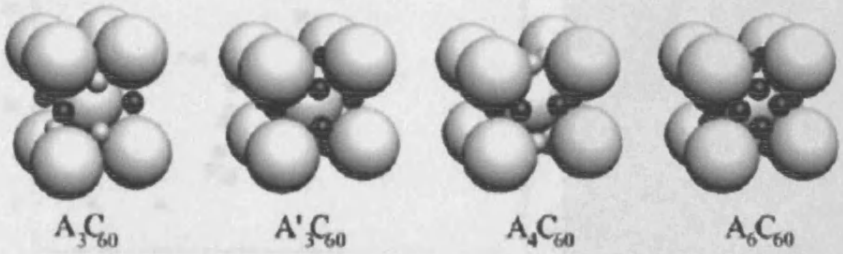

Figure 1.9: Approximate structure of the A_XC_{60} salts from ref [9].

Salt	Structure	Electronic Properties
KC_{60}	Polymeric	Metallic[9]
K_3C_{60}	Face centred cubic	Superconducting $T_c = 18K$[9]
K_4C_{60}	Body centred tetragonal	Semi-Conducting[7]
K_6C_{60}	Body centred cubic	Semi-Conducting[7]

Table 1.3: Properties of potassium salts of C_{60}.

We now concentrate our discussion on the superconducting A_3C_{60} salts, the study of which has yielded famous as well as infamous science.[96,97] For more detail, the reader is pointed towards a series of books and review articles.[7,9,98,99,100,101]

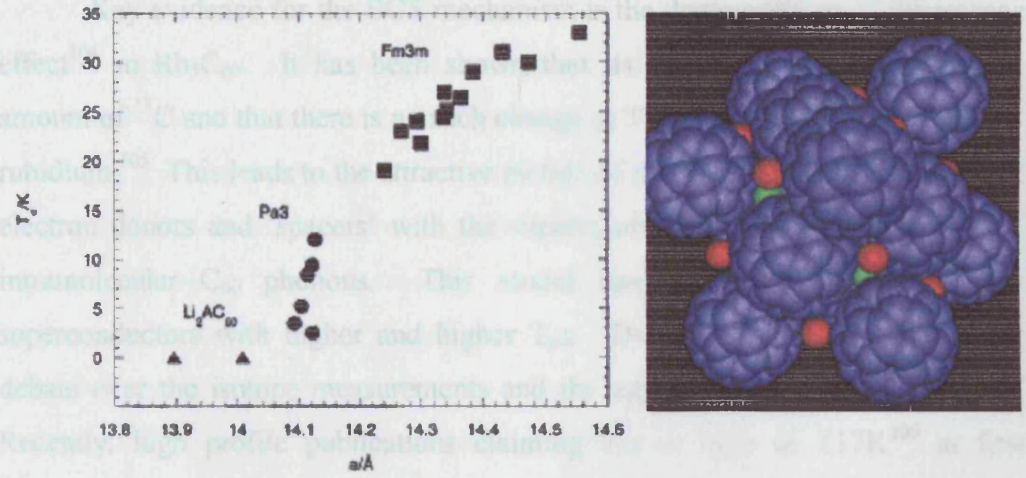

Figure 1.10: The linear relationship between lattice parameter and T_c in the A_3C_{60} fcc superconductors from ref [100] (left), and the structure of an fcc superconductor showing the tetrahedral (green) and octahedral sites (red) (right) from ref [102].

Figure 1.10 shows the linear relationship between T_c and lattice constant. Within this graph, the A_3C_{60} superconductors can broadly be divided into two groups: those with Pa3 symmetry which contain Na^+ ions or smaller, and those which contain K^+ ions or larger, which have the Fm3m symmetry (the fcc structure of solid fullerite). These two symmetries arise from the relative orientation of the C_{60}^{3-}s.[100] The metal ions occupy the octahedral (red) and tetrahedral (green) sites in the crystal, as shown in the same figure, and increase the ball separation without distorting the lattice itself. The T_c's dependence on the lattice is evidence for BCS,[103] phonon mediated, superconductivity. This increase of T_c with lattice parameter can be qualitatively understood: as the lattice increases, the electronic overlap between molecules decreases, reducing the size of the bandwidth, but not the number of states. As a result, the density of states at the Fermi surface increases and this is proportional to its T_c. There is, however, an ongoing debate on the applicability of this model.

Key evidence for the BCS mechanism is the demonstration of the isotope effect[104] in Rb_3C_{60}. It has been shown that its T_c decreases with increasing amount of ^{13}C and that there is no such change in T_c upon changing the isotope of rubidium.[105] This leads to the attractive picture of the metal cations acting only as electron donors and 'spacers' with the superconductivity mediated only by the intramolecular C_{60} phonons. This model stimulated a frantic search for superconductors with higher and higher T_cs. There has, however, been some debate over the isotope measurements and the applicability of the BCS model. Recently, high profile publications claiming T_cs as high as 117K[106] at first intensified interest in these systems, but ultimately led to disillusionment as the papers were retracted. This development led to possible misunderstandings[107] and since the retraction of the papers the research has run a bit cold.

1.8.1 Ammoniation of the C_{60} Salts

A focus of research into the superconductors relevant to this work is the study of the effect of the addition of ammonia to C_{60} salts. Increasing the lattice parameter, and hence the T_c, has been achieved by coordinating the dopant ions with neutral ammonia molecules. It has been shown that the superconducting transition temperature of the salt Na_2CsC_{60} can be increased from 10.5 to 29.6K upon ammoniation. Here ammonia molecules solvate the sodium ions and increase the lattice parameter from 14.132Å to 14.473Å.[108] There has been little further success in recording another dramatic increase in the T_c by this method.

In the case of $(NH_3)K_3C_{60}$ the superconductivity is suppressed.[99] This is accompanied by a change in the lattice symmetry to orthorhombic. The superconductivity has been reported as being recovered at high pressures[109] with the compound still retaining its orthorhombic structure.[110] Interestingly, this forms the only recorded example of a non cubic superconductor among these systems.

In the case of the system $(NH_3)_xNaA_2C_{60}$ ($0.5 < x < 1$, A = K, Rb), the T_c is again suppressed and actually increases with decreasing ammonia content.[99] The ammonia molecules have been found to coordinate the metal ions in the interstitial sites resulting in an off centring of the Na^+ anion, which may explain this trend. Structural data shows that the ammonia, as well as coordinating the cation, forms close hydrogen-bonds (~2.5Å) to the C_{60}^{3-} anions, which may then be the key to understanding the electronic properties of the resulting solids.[111] This 'solvent' arrangement is shown in Figure 1.11 and may be reflected in the structure of the metal-ammonia-fulleride solutions.

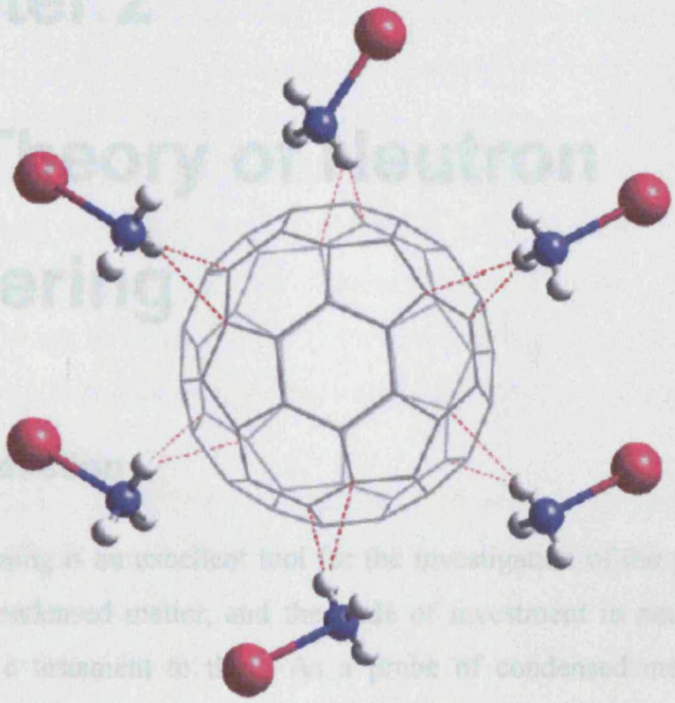

Figure 1.11: The structure of ammonia in $(NH_3)_xNaA_2C_{60}$ from ref [111].

Chapter 2

The Theory of Neutron Scattering

2.1 Introduction

Neutron scattering is an excellent tool for the investigation of the properties and structure of condensed matter, and the scale of investment in neutron facilities worldwide is a testament to this. As a probe of condensed matter, neutrons complement X-rays and electrons.

Firstly neutrons are uncharged and, unlike electrons and X-rays, interact with atomic nuclei rather than their electrons. This means that the neutrons are highly penetrating and typically non-destructive, in contrast to X-rays and electrons. Neutrons can hence also be used to probe the bulk properties or bulk structure of the material under study. The de Broglie wavelength of thermal neutrons (energies of 5 – 100meV) is comparable to interatomic distances as well as certain atomic and molecular excitations. Neutrons also have a magnetic

moment permitting the study of magnetic ordering and magnetic excitations using spin polarised neutrons.

Neutrons are scattered by the strong nuclear force with a magnitude that is dependent on the spin state and composition of the scattering nucleus. X-rays scatter from electrons, the magnitude of scattering for a particular element increasing with atomic number. This means that in using X-ray diffraction, it is very difficult to see a light atom in a system including heavier atoms, or to differentiate between elements of similar atomic number. This is not the case with neutrons. In fact, the magnitude of neutron scattering varies between isotopes of the same element enabling the powerful technique of isotopic substitution. This allows the separation of individual correlation functions from the average correlation function achieved in a diffraction measurement (see Section 2.9). A similar technique called 'contrast matching' can be used in the small angle regime to separate regions of uniform scattering density to investigate the structure of colloidal particles and proteins. The fact that hydrogen significantly scatters neutrons (unlike X-rays) is important and permits the study of proton dynamics, as well as phenomena such as hydrogen-bonding.

This chapter concentrates on the theory of neutron scattering[112] with an emphasis on diffraction and small angle scattering. The final part of the chapter details the mathematics of second order isotopic substitution. The derivation presented here is based mainly on the opening chapters of the book "Introduction to the Theory of Thermal Neutron Scattering" by G. L. Squires,[112] and the reader is referred to this book for more details of specific steps in the derivations.

2.2 Neutron Properties

The neutron is a subatomic nuclear particle; its basic properties are shown in Table 2.1.

Mass	1.775×10^{-27} kg
Charge	0
Spin	½
Magnetic dipole moment	$-1.913\ \mu_N$

Table 2.1: Basic properties of a neutron.

The momentum ***p*** of a neutron is given by:

$$\mathbf{p} = \hbar\mathbf{k}, \qquad 2.1$$

where ***k*** is the neutron's wavevector the magnitude of which is given by $k = \frac{2\pi}{\lambda}$, and λ is the de Broglie wavelength of the neutron.

The neutron's velocity, v, is then given by:

$$v = \frac{\hbar k}{m}. \qquad 2.2$$

The neutron's energy is related to its wavevector by:

$$E = \frac{\hbar^2 k^2}{2m}. \qquad 2.3$$

Typical thermal neutrons of wavelength 1.8Å have a speed of ~2100m/s and energy of ~24meV.

2.2 Definitions

2.2.1 The Scattering Vector, Q

In an individual scattering event, a neutron, incident energy E and wavevector $\boldsymbol{k}$, is scattered by a nucleus. After the event, the neutron has energy E' and wavevector $\boldsymbol{k}'$. By the principal of conservation of momentum:

$$\hbar\mathbf{Q} = \hbar\mathbf{k} - \hbar\mathbf{k}', \qquad 2.4$$

where $\boldsymbol{Q}$ is the **scattering vector** and is defined as:

$$\mathbf{Q} = \mathbf{k} - \mathbf{k}'. \qquad 2.5$$

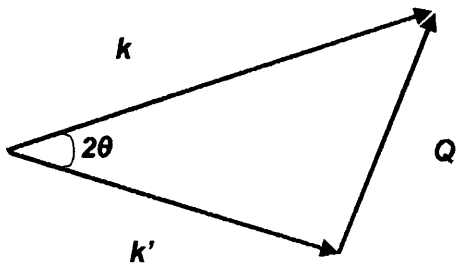

Figure 2.1: Definition of the scattering vector Q, during a scattering event in which a neutron has incident wave vector, $\boldsymbol{k}$ and final wave vector $\boldsymbol{k}'$.

In Figure 2.1 the magnitude of $\boldsymbol{k}'$ is less than $\boldsymbol{k}$: the process is inelastic and some energy is transferred to the scattering nucleus. If the scattering event is elastic, $|\boldsymbol{k}|=|\boldsymbol{k}'|$ and the magnitude of $\boldsymbol{Q}$ is given by:

$$Q = \frac{4\pi \sin\theta}{\lambda}, \qquad 2.6$$

where 2θ is the scattering angle.

2.2.2 Differential Cross Sections

The quantities measured in a scattering experiment are known as cross-sections. A cross-section of scattering gives the ratio of the number of scattering events per unit time to the flux of incident particles. The theory of neutron scattering aims to derive theoretical expressions for these quantities.

The **total scattering cross section**, σ, gives the total number of scattering events *in all directions* per unit flux, and therefore represents the total probability of the scattering:

$$\sigma = \frac{\text{total number of neutrons scattered per second}}{\Phi}, \qquad 2.7$$

where Φ is the flux of the incident neutrons (the number of neutrons through unit area perpendicular to direction of the beam per second).

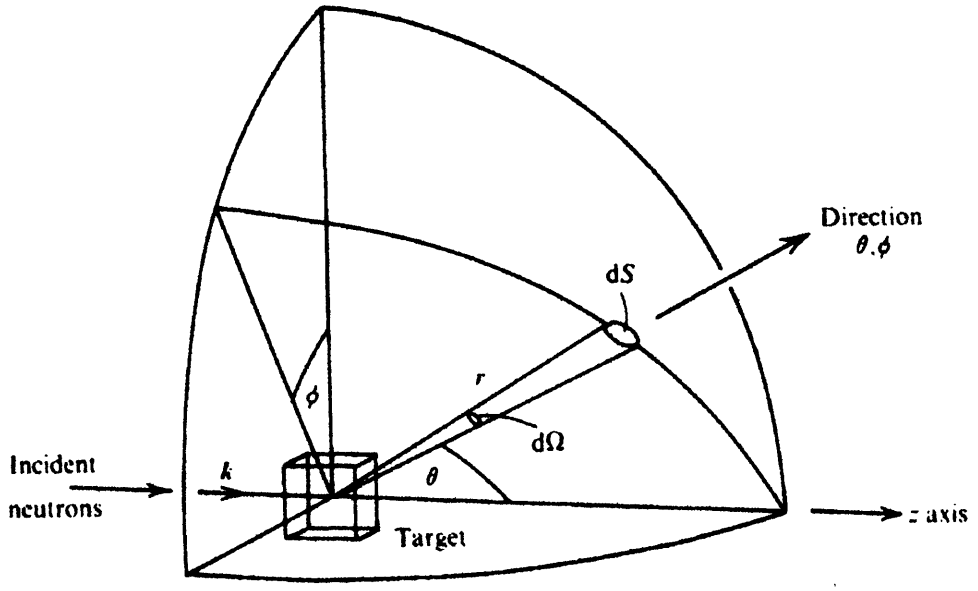

Figure 2.2: The geometry of a scattering experiment taken from ref.[112]

The geometry of the scattering event is shown in Figure 2.2. The incident neutrons are scattered by the sample into a finite element of solid angle $d\Omega$ in the

direction θ, ϕ. If we count these neutrons we obtain the **differential cross section**, i.e. the probability of the incident particles scattering into $d\Omega$. This is given by:

$$\frac{d\sigma}{d\Omega} = \frac{number\ of\ neutrons\ scattered\ per\ second\ into\ d\Omega\ in\ direction\ \theta, \phi}{\Phi d\Omega}. \quad 2.8$$

If we analyse the energy of the scattered neutrons we obtain the **partial differential cross section**:

$$\frac{d^2\sigma}{d\Omega dE'} = \frac{\text{number of neutrons scattered per second into a solid angle } d\Omega \text{ in direction } \theta, \phi \text{ with a final energy between } E' \text{ and } E' + dE'}{\Phi d\Omega dE'} \quad .2.9$$

The cross sections are then related by the equations:

$$\frac{d\sigma}{d\Omega} = \int_0^\infty \frac{d^2\sigma}{d\Omega dE'} dE' \quad 2.10$$

$$\sigma = \int_0^{4\pi} \frac{d\sigma}{d\Omega} d\Omega. \quad 2.11$$

In a neutron scattering experiment, the measured intensity $I(Q)$ (in counts per unit solid angle per second), can therefore be expressed in terms of the partial differential cross-section:

$$I(Q) = \Phi \frac{d^2\sigma}{d\Omega dE'} d\Omega dE'. \quad 2.12$$

2.3 Scattering of Neutrons from a Bound Nucleus

Consider a neutron scattered by a fixed nucleus. During the scattering event, there can be no kinetic energy added to the nucleus. The wavelength of thermal neutrons is of the order 10^{-10}m, much larger than the typical range of the nuclear forces which is of the order 10^{-14} – 10^{-15}m: the incident neutron sees the nucleus as

a point. This means the incident and scattered wavefunctions of the neutron can be approximated to spherically symmetric S-waves[112] (wave theory):

$$\psi_{inc} = e^{ikz}, \tag{2.13}$$

$$\psi_{sc} = -\frac{b}{r}e^{ikr}, \tag{2.14}$$

where k is the magnitude of the wavevector $\boldsymbol{k}$, z is the position of the incoming wave on an axis in the direction of $\boldsymbol{k}$, r is the distance of the scattered wave at position $\boldsymbol{r}$ from the fixed nucleus and b is a constant independent of angles θ, ϕ. The factor of $1/r$ means that the intensity (the square of the amplitude of the wavefunction) decreases with the inverse square of the distance from the source, as is consistent with the inverse square law of all wave motions. The constant b is known as the scattering length of the nucleus. It is a measure of the strength of the scattering interaction and is dependent only on the nucleus from which it is scattered. The scattering length is related to the total cross section by the relationship:

$$\sigma = 4\pi b^2. \tag{2.15}$$

2.4 Scattering from a General System of Particles

We first evaluate an expression for the **differential cross section**. The differential cross section (as defined by equation 2.8) represents the sum of all processes in which the state of the scattering system changes from $\lambda \rightarrow \lambda'$ and the state of the neutron changes from $\mathbf{k} \rightarrow \mathbf{k}'$, and can be expressed as:

$$\left(\frac{d\sigma}{d\Omega}\right)_{\lambda \longrightarrow \lambda'} = \frac{1}{\Phi}\frac{1}{d\Omega}\sum_{\mathbf{k}' in\, d\Omega} W_{\mathbf{k},\lambda} \rightarrow W_{\mathbf{k}',\lambda'}, \tag{2.16}$$

where $W_{\mathbf{k},\lambda} \rightarrow W_{\mathbf{k}',\lambda'}$ is the number of transitions per second from the state $\boldsymbol{k}$, λ to the state $\boldsymbol{k}'$, λ'. The incident and scattered neutron have wavefunctions $\psi_{\mathbf{k}}$ and

$\psi_{\mathbf{k}'}$ respectively. The sum on the right hand side of the equation is taken over all values of $\boldsymbol{k}'$ that lie in $d\Omega$ in the direction θ, ϕ, the values of $\boldsymbol{k}$, λ, λ' remaining constant. This sum can be evaluated using Fermi's Golden Rule, a fundamental result from quantum mechanics:

$$\sum_{\mathbf{k}' \text{ in } d\Omega} W_{\mathbf{k},\lambda} \rightarrow W_{\mathbf{k}',\lambda'} = \frac{2\pi}{\hbar} \rho_{\mathbf{k}'} \left| \langle \mathbf{k}'\lambda' | V | \mathbf{k}\lambda \rangle \right|^2 , \qquad 2.17$$

where $\rho_{\mathbf{k}'}$ is the number of momentum states in $d\Omega$ per unit energy range for neutrons in the state $\boldsymbol{k}'$, and V is the potential between the neutron and the scattering system. This potential is assumed much weaker than the energy of the incident neutrons allowing the neutron's wavefunctions to be represented by spherical S-waves (Born approximation).

The matrix element can be written explicitly as:

$$\left| \langle \mathbf{k}'\lambda' | V | \mathbf{k}\lambda \rangle \right|^2 = \int \psi^*_{\mathbf{k}'} \chi^*_{\lambda'} V \psi_{\mathbf{k}} \chi_{\lambda} d\mathbf{R} d\mathbf{r} , \qquad 2.18$$

where $d\mathbf{R}$ is an element of volume for the nucleus, and $d\mathbf{r}$ is an element of volume for the neutron. χ_{λ} and $\chi^*_{\lambda'}$ are the initial and final states of the wavefunctions of the scattering system respectively.

In order to evaluate $\rho_{\mathbf{k}'}$ and to fix the normalisation constant of the neutron wave functions, the method of box normalisation is used.[112] This assumes the neutron and scattering system to be contained in a large box with sides of length L, allowing $\rho_{\mathbf{k}'}$ [112] to be written as:

$$\rho_{\mathbf{k}'} = \left(\frac{L}{2\pi} \right)^3 \frac{mk'}{\hbar^2} d\Omega . \qquad 2.19$$

The wavefunctions of the neutron become:

$$\psi_{\mathbf{k}} = \frac{1}{L^{3/2}} e^{i\mathbf{k}.\mathbf{r}}, \tag{2.20}$$

$$\psi_{\mathbf{k}'} = \frac{1}{L^{3/2}} e^{i\mathbf{k}'.\mathbf{r}}. \tag{2.21}$$

The incident neutron flux is given by the product of neutrons' density and velocity:

$$\Phi = \frac{1}{L^3}\frac{\hbar k}{m}. \tag{2.22}$$

Substituting equations 2.17, 2.19 and 2.22 into equation 2.16 obtains the expression:

$$\left(\frac{d\sigma}{d\Omega}\right)_{\lambda \longrightarrow \lambda'} = \frac{k'}{k}\left(\frac{m}{2\pi\hbar^2}\right)^2 \left|\left\langle \mathbf{k}'\lambda' \middle| V \middle| \mathbf{k}\lambda \right\rangle\right|^2. \tag{2.23}$$

Given equation 2.18 and that $\chi_\lambda \chi_{\lambda'}$ are normalised, this becomes:

$$\left(\frac{d\sigma}{d\Omega}\right)_{\lambda \longrightarrow \lambda'} = \frac{k'}{k}\left(\frac{m}{2\pi\hbar^2}\right)^2 \left|\int e^{-i\mathbf{k}'.\mathbf{r}} V e^{i\mathbf{k}.\mathbf{r}} dr\right|^2. \tag{2.24}$$

As $\hbar\mathbf{Q} = \hbar\mathbf{k} - \hbar\mathbf{k}'$, this can be rewritten as:

$$\left(\frac{d\sigma}{d\Omega}\right)_{\lambda \longrightarrow \lambda'} = \frac{k'}{k}\left(\frac{m}{2\pi\hbar^2}\right)^2 \left|\int e^{i\mathbf{Q}.\mathbf{r}} V dr\right|^2. \tag{2.25}$$

The range of the scattering potential $V(\boldsymbol{r})$ is assumed to be short due to the relatively small size of the nucleus. This allows $V(\boldsymbol{r})$ to be expressed as a sum of Fermi pseudopotentials from the individual scattering centres, given by:

$$V(\mathbf{r}) = \frac{2\pi\hbar^2}{m}\sum_j^N b_j \delta(\mathbf{r} - \mathbf{r}_j), \tag{2.26}$$

where b_j is the scattering length of the jth nucleus located at position r_j. The Dirac delta function is zero unless the position vector $\boldsymbol{r}$ coincides with $\boldsymbol{r}_j$.

Now, since $\int F(x)\delta(x-x_j)dx = F(x_j)$, equation 2.25 can be written:

$$\left(\frac{d\sigma}{d\Omega}\right)_{\lambda\longrightarrow\lambda'} = \frac{k'}{k}\left|\int b_j e^{i\mathbf{Q}.\mathbf{r}_j}dr\right|^2. \qquad 2.27$$

We now derive an expression for the **partial differential cross-section**. If E and E' are the initial and final energies of the neutron, and E_λ and $E_{\lambda'}$ the initial and final energies of the scattering system, then by the conservation of energy:

$$E + E_\lambda = E' + E_{\lambda'}. \qquad 2.28$$

Mathematically, the energy distribution of scattered neutrons is a delta function:[112]

$$\delta(E + E_\lambda - E' - E_{\lambda'}). \qquad 2.29$$

Given that:

$$\int \delta(E + E_\lambda - E' - E_{\lambda'})dE' = 1, \qquad 2.30$$

the partial differential cross section then is given by:

$$\left(\frac{d^2\sigma}{d\Omega dE}\right)_{\lambda\longrightarrow\lambda'} = \frac{k'}{k}\left|\int b_j e^{i\mathbf{Q}.\mathbf{r}_j}dr\right|^2 \delta(E - E' + E_\lambda - E_{\lambda'}). \qquad 2.31$$

The δ-function for the energy can be expressed as an integral with respect to time:[112]

$$\delta(E - E' + E_\lambda - E_\lambda) = \frac{1}{2\pi\hbar}\int_{-\infty}^{\infty} e^{\frac{i(E_{\lambda'} - E_\lambda)t}{\hbar}} e^{-i\omega t}dt. \qquad 2.32$$

The energy change of the neutron is finite and can be written:

$$E - E' = \hbar\omega \qquad 2.33$$

where ω is positive for energy loss and negative for energy gain.

Substituting into 2.32, the resulting expression can be written:[112]

$$\left(\frac{d^2\sigma}{d\Omega dE'}\right) = \frac{k'}{k}\frac{1}{2\pi\hbar}\sum_{jj'} b_j b_{j'} \int_{-\infty}^{\infty} \left\langle e^{-i\mathbf{Q}\cdot\mathbf{r}_{j'}(0)} e^{i\mathbf{Q}\cdot\mathbf{r}_j(t)} \right\rangle e^{-i\omega t} dt . \qquad 2.34$$

This is for a system in which the scattering length b varies from one nucleus to another. The angular brackets denote an average over all starting times for observations of the system. This is equivalent to an averaging over all thermodynamic states of the system.

2.5 Coherent and Incoherent Scattering

The scattering lengths of nuclei depend on their spin state. Most nuclei have several spin states and, as these states are generally randomly distributed in the sample, the scattering lengths in equation 2.34 can be averaged over all the nuclear spin states for an individual nuclear species. The average values of b and b^2 for the system can be expressed as:

$$\bar{b} = \sum_i f_j b_j \qquad \overline{b^2} = \sum_i f_j b_j^2 , \qquad 2.35$$

where f_j is the relative frequency of the individual scattering length b_j.

Equation 2.34 can then be rewritten:[112]

$$\left(\frac{d^2\sigma}{d\Omega dE'}\right)=\frac{k'}{k}\frac{1}{2\pi\hbar}\left[\begin{array}{l}\left(\bar{b}\right)^2\sum_{jj'}\int_{-\infty}^{\infty}\left\langle e^{-i\mathbf{Q}.\mathbf{r}_{j'}(0)}e^{i\mathbf{Q}.\mathbf{r}_j(t)}\right\rangle e^{-i\omega t}dt+\\ \left(\overline{b^2}-\left(\bar{b}\right)^2\right)\sum_{j}\int_{-\infty}^{\infty}\left\langle e^{-i\mathbf{Q}.\mathbf{r}_j(0)}e^{i\mathbf{Q}.\mathbf{r}_j(t)}\right\rangle e^{-i\omega t}dt\end{array}\right]. \qquad 2.36$$

This separates the **coherent** and **incoherent** contributions to the partial differential cross section. The first term, on the right hand side of equation 2.36, depends on the correlation between the positions of the nucleus j' at time zero and nucleus j at time t. Occasionally j' and j are the same nucleus but in general they are not, as the total number of nuclei is very large. This term gives rise to interference effects and is known as the **coherent scattering**. The coherent scattering therefore provides the structural information of the sample and is the quantity extracted in a diffraction experiment.

The second term is known as the **incoherent scattering** and depends only on the correlations between the same nucleus at different times, providing a measure of the diffusion of atoms. Incoherent scattering does therefore not give rise to interference effects. In general, the incoherent scattering is isotropic and adds a structureless background to the coherent scattering in diffraction measurements.

The neutron scattering lengths can then be defined as:

$$b_{coh}=\bar{b} \qquad 2.37$$

$$b_{inc}=\sqrt{\overline{b^2}-\left(\bar{b}\right)^2}\,. \qquad 2.38$$

There is no obvious correlation between the scattering lengths and the position of elements in the periodic table. This, as mentioned in the introduction, is partly why neutrons can be more useful than X-rays. The scattering lengths are determined experimentally. For example, hydrogen has a large incoherent scattering length of ~25.18fm and a small coherent scattering length ~-3.74fm.

Deuterium has a much smaller incoherent scattering of ~3.99fm but a larger coherent scattering of ~6.67fm.

2.6 Diffraction Measurements

Diffraction is an elastic process and measures the fixed average structure of the system under study. It is therefore only dependent on Q. In a diffraction measurement the 'static approximation' is made: it is assumed that the energy of the incident neutron is very much greater than the energy transfer in the neutron-nucleus interaction, i.e. $E >> h\omega$ and that $k \approx k'$. Neutron diffractometers effectively integrate over all energy transfers, obtaining an ensemble averaged 'snap-shot' view at t=0.[113] However, the approximation does not hold completely true for liquids and in particular light elements, therefore inelastic corrections must be applied to diffraction data as well (see Chapter 3).

If we then integrate equation 2.36 with respect to energy, like the neutron detectors, we obtain an expression for the differential cross section:

$$\left(\frac{d\sigma}{d\Omega}\right) = \frac{1}{N}\left(\bar{b}\right)^2 \sum_{j,j'=1} \left\langle e^{-i\mathbf{Q}.(\mathbf{r}_j(0)-\mathbf{r}_{j'}(0))} \right\rangle + \left(\overline{b^2} - \left(\bar{b}\right)^2\right). \qquad 2.39$$

If the scattering system is isotropic the exponential term in 2.39 can be simplified as the distance between two nuclei j and j' is given by:

$$\mathbf{r}_{jj'} = \left|\mathbf{r}_j - \mathbf{r}_{j'}\right| \qquad 2.40$$

so,

$$\left\langle e^{-i\mathbf{Q}.(\mathbf{r}_j(0)-\mathbf{r}_{j'}(0))} \right\rangle = \frac{\sin Qr_{jj'}}{Qr_{jj'}}. \qquad 2.41$$

The density function is defined as:

$$\rho(r) = \rho_0 g(r), \qquad 2.42$$

where $g(r)$ is the pair correlation function and gives the probability of finding an atom at a distance r from an arbitrary atom.

This allows the measured differential cross-section to be written (after the subtraction of zero angle scattering) as:

$$\frac{d\sigma}{d\Omega} = \left(\overline{b^2} - \left(\bar{b}\right)^2\right) + \left(\bar{b}\right)^2 \int 4\pi r^2 \rho_0 \left[g\ (r) - 1\right] \frac{sin(Qr)}{Qr} dr \,. \qquad 2.43$$

2.7 Faber-Ziman Formalism

The partial structure factor, $S_{\alpha\beta}(Q)$, contains the information about correlations between the two atomic species α and β in Q-space, and is defined as:

$$S_{\alpha\beta}(Q) - 1 = \frac{4\pi\rho_0}{Q} \int_0^\infty r[g_{\alpha\beta}(r) - 1]\sin(Qr)dr \,. \qquad 2.44$$

The differential cross-section measured in a neutron scattering experiment, containing N chemical species can therefore be written as a weighted sum of the different structure factors, arising from the correlations between different pairs of atoms:

$$\frac{d\sigma}{d\Omega} = \sum_{\alpha=1}^{N} c_\alpha \overline{b_\alpha^2} + \sum_{\alpha=1}^{N}\sum_{\beta=1}^{N} c_\alpha c_\beta \bar{b}_\alpha \bar{b}_\beta [S_{\alpha\beta}(Q) - 1] \qquad 2.45$$

where c_α and c_β are the atomic fractions of α and β.

We define the total structure factor, $F(Q)$, which contains the information of the structure of a scattering system, the second term in 2.45, as:

$$F(Q) = \sum_\alpha \sum_\beta c_\alpha c_\beta \bar{b}_\alpha \bar{b}_\beta [S_{\alpha\beta}(Q) - 1] \,. \qquad 2.46$$

The total structure factor is therefore the neutron weighted sum of all the individual partial structure factors. It is the quantity extracted during a diffraction experiment after having subtracted self scattering and incoherent scattering. The total pair distribution function is given by:

$$G(r) = \sum_{\alpha}\sum_{\beta} c_{\alpha} c_{\beta} \bar{b}_{\alpha} \bar{b}_{\beta} [g_{\alpha\beta}(r) - 1]. \qquad 2.47$$

The individual $g_{\alpha\beta}$ is a sine Fourier transform of the $S_{\alpha\beta}(Q)$ and can be calculated via:

$$g_{\alpha\beta}(r) - 1 = \frac{1}{r 2\pi^2 \rho_0} \int_0^{\infty} Q[S_{\alpha\beta}(Q) - 1] \sin(Qr) dQ. \qquad 2.48$$

From this the average number of atoms of type β surrounding type α, between radii r_1 and r_2 is given by:

$$\bar{n}_{\beta}^{\alpha} = 4\pi n_0 c_{\beta} \int_{r_1}^{r_2} r^2 g_{\alpha\beta}(r) dr, \qquad 2.49$$

where n_0 is the atomic number density of the sample.

2.8 Small Angle Neutron Scattering

An expression for the partial differential cross-section was derived. This can be simplified if the magnitude of Q is very small compared with interatomic distances. In this case, the exponential factors do not vary much from atom to atom and it is not possible to separate the contribution of individual atoms. For coherent elastic scattering 2.34 becomes:

$$\left(\frac{d\sigma}{d\Omega}\right) = \left| \int b(r) e^{iQ \cdot r} dr \right|^2, \qquad 2.50$$

where $b(r)$ is the average scattering length density. This is calculated by summing the coherent scattering lengths over a small volume and dividing by that volume. This integral extends over the whole sample.

If the sample is of identical particles of uniform scattering, b_P, in a uniform matrix scattering density, b_S, equation 2.50 can be written:[114,115]

$$\left(\frac{d\sigma}{d\Omega}\right) = (b_P - b_S)^2 N_P V_P^2 P(Q) S(Q), \qquad 2.51$$

where N_P is the number concentration of the particles and V_P is the volume of one scattering body. The $S(Q)$ and the $P(Q)$ are the functions which contain the information on the shape and distribution of the particles in solution. The $P(Q)$ is known as the 'form factor'. This provides information on the shape of the particles, and describes how the differential cross section is modulated by interference effects of the scattering from different parts of the same scattering body. The $S(Q)$ is known as the 'structure factor' and is analogous to equation 2.44. The $S(Q)$ provides information on the interaction of particles in solution, i.e. it describes how the differential cross section is modulated by interference effects of the scattering from different scattering bodies.[115]

2.9 Second Order Isotopic Substitution

Neutrons scatter differently from different isotopes of the same atomic species. This means that one can take a measurement, repeat the measurement having changed the isotope of one of the atomic species, subtract one measurement from the other to leave only correlations from the substituted atoms. This technique is most accurate for isotopes with a large difference in their scattering lengths, such as deuterium (b_D = 6.67fm) and hydrogen (b_H = -3.74fm).

This method can be extended if a third experiment is undertaken in which the scattering length is changed further (using a mix of H and D, for example). In combination with the first two measurements, one can extract more information.

In the case of the hydrogen substitution, the partial structure factors, $S_{HH}(Q)$, $S_{XH}(Q)$ and $S_{XX}(Q)$, where H refers to substituted hydrogen atoms and X refers to any non-substituted atom, can be obtained. Extracting these functions is the technique of second order isotopic substitution.[85]

After incoherent, inelastic, absorption and background subtractions, the quantity obtained from a diffraction experiment is the total structure factor, $F(Q)$:

$$F(Q) = \sum_{\alpha\beta} c_\alpha c_\beta b_\alpha b_\beta \left[S_{\alpha\beta}(Q) - 1\right], \qquad 2.52$$

where $S_{\alpha\beta}(Q)$ is the Faber-Ziman partial structure factor defined above in equation 2.44.

In the case of second order hydrogen/deuterium isotopic substitution, this can be written as the sum of the three partial structure factors:

$$F(Q) = c_X^2 b_X^2 \left[S_{XX}(Q) - 1\right] + 2c_X c_H b_X b_H^2 \left[S_{XH}(Q) - 1\right] + c_H^2 b_H^2 \left[S_{HH}(Q) - 1\right], \qquad 2.53$$

where the composite coherent scattering length b_X and concentration, c_X are defined by:

$$b_X = \sum_{\alpha \neq \beta} \frac{c_\alpha b_\alpha}{c_X} \qquad \text{and} \qquad c_X = \sum_{\alpha \neq \beta} c_\alpha . \qquad 2.54$$

Since $c_H = (1 - c_X)$, the $S_{HH}(Q)$ structure factor can then be calculated as follows:

$$S_{HH}(Q) = \frac{xF_H(Q) + (1-x)F_D(Q) - F_{HD}(Q)}{c_H^2 \left[xb_H^2 + (1-x)b_D^2 - b_{HD}^2\right]} \qquad 2.55$$

where subscripts H and D refer to the hydrogenated and deuterated samples respectively, and HD as a mixture sample, x being the fraction of the light sample in this mixture. Therefore:

$$b_{HD} = xb_H + (1-x)b_D . \qquad 2.56$$

Similarly the $S_{XH}(Q)$ and $S_{XX}(Q)$ partial structure factors are calculated from the following equations:

$$S_{XH}(Q)-1=\frac{F_H(Q)-F_D(Q)-c_H^2\left(b_D^2-b_H^2\right)\left[S_{HH}(Q)-1\right]}{2c_Xc_Hb_X\left(b_H-b_D\right)} \qquad 2.57$$

$$S_{XX}(Q)-1=\frac{F_H(Q)-2c_Hc_Xb_Hb_X\left[S_{XH}(Q)-1\right]-c_H^2b_H^2\left[S_{HH}(Q)-1\right]}{c_X^2b_X^2}. \qquad 2.58$$

The weighting factors for the partial terms contributing to the composite partial structure factors are:

$$S_{XH}(Q)-1=\frac{\sum_{\alpha\neq H}c_\alpha b_\alpha\left[S_{\alpha H}(Q)-1\right]}{c_Xb_X} \qquad 2.59$$

$$S_{XX}(Q)-1=\frac{\sum_{\alpha\neq H,\beta\neq H}c_\alpha b_\alpha c_\beta b_\beta\left[S_{\alpha\beta}(Q)-1\right]}{c_X^2b_X^2}. \qquad 2.60$$

Chapter 3

Experimental Details and Data Reduction

3.1 Introduction

Making metal-ammonia-fulleride solutions involves the techniques of high integrity vacuum systems, gas feed, the manipulation of toxic and air sensitive substances and cryogenics. A large part of this project was spent devising and refining experimental techniques and methods. This chapter describes these experimental details and outlines the methods used for the data reduction of the neutron scattering experiments.

Metal-ammonia-fulleride solutions are made by dissolving fullerite C_{60} crystal in a metal-ammonia solution. This is done by condensing a known amount of ammonia gas onto pre-weighed, stoichiometric amounts of fullerite powder and alkali metal. The mechanism of the dissolution of the fullerene is a two stage process. At first, the metal dissolves in liquid ammonia; its electrons dissociate

and are solvated along with the metal ions.[5,85,83] The fullerene C_{60} then sequentially picks up the electrons and the resulting fulleride anions dissolve to form homogenous solutions.[6] This process is visible as a colour change of the solution. The blue of the dilute metal-ammonia solution arising from the presence of the solvated electron, becomes dark reddish brown upon addition of the fullerite due to the presence of the fulleride, see Figure 3.1.[5,8]

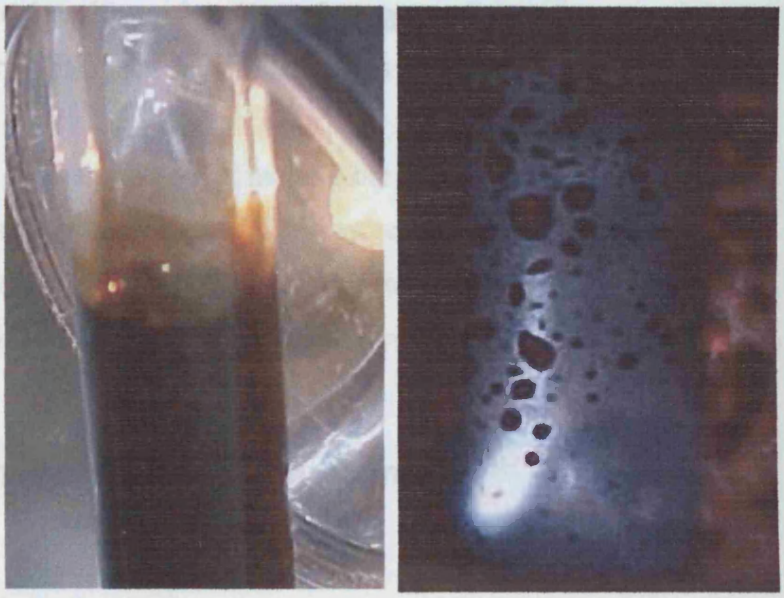

Figure 3.1: Dark red potassium-ammonia-fulleride solution (left), blue (dilute) metal-ammonia solution (right).

Metal-ammonia solutions themselves are meta-stable and, over a period of time, will decompose to form the metal amide and hydrogen gas. Due to the presence of the solvated electrons, these solutions are highly reducing and hence extremely reactive. It is essential to eliminate impurities and pay careful attention to the sample environment conditions in order not to accelerate this decomposition. However, it has been found that once the fulleride is in solution, and all the electrons have been 'picked up', the decomposition of the solutions is greatly decelerated and stable solutions of anions have been kept for several

months (see Chapter 7). The fullerides themselves react readily with oxygen and water and must be isolated from them at all times.[3,116]

The individual components of the metal-ammonia solutions are very reactive and difficult to handle in their own right. Ammonia is highly corrosive to many materials and a toxic gas under standard conditions; high pressures or low temperatures are required to maintain it in the liquid state. Alkali metals react violently and readily with water and oxygen and therefore must be manipulated in an inert dry atmosphere, such as an argon glovebox.

A generic method of making the solutions will be detailed, followed by experiment specific designs. The key requirements in all cases are temperature control, gas feed, a vacuum around an inert cell to prevent icing, and a valve on the cell so that it can be sealed in the glovebox.

3.2 Sample Preparation: Generic

3.2.1 C_{60}, Fullerene

Fullerite, C_{60} was bought from SES Research, Texas, USA, of a typical purity 99.95% and is a crystalline black powder. To remove any adsorbed species, the powder was heated to 200°C under a dynamic vacuum prior to use. This was done for at least 24 hours after which the powder was not exposed to air. It has been shown that fullerene C_{60} can polymerise under UV/visible light,[117] so the fullerite powder was always kept in an opaque container. The warning that C_{60} might be carcinogenic by Kroto himself[118] was heeded and due care was taken when handling the powder.

3.2.2 Preparing the Gas Handling Equipment

Many past studies of metal-ammonia solutions have been hampered by the unpredictable reactivity of the samples. It is likely that low integrity vacuums and

the presence of impurities were the source of such decompositions. Recently, using high integrity gas handling equipment, samples of metal-ammonia solutions have been shown to be stable for more than 48 hours during neutron diffraction experiments.[81,82,83,85] The general method used in these experiments was therefore followed in order to ensure the highest quality samples. It was of paramount importance to remove any impurities from the set-up. If the alkali metal or alkali metal-ammonia solution degraded slightly, the stoichiometry of the solution would be significantly altered and the charge on the anion in solution changed.

Due to the corrosive nature of liquid ammonia to many materials, the gas handling equipment (gas-rig) was made out of stainless steel Swagelok® components with PTFE seats on the valves. Prior to experiments, the gas-rig was leak tested with a helium leak detector. Once the rig was completely leak tight, it was evacuated, using a turbo pump, to pressures of $\sim 10^{-6}$ millibar, for at least 24 hours before the experiment. The gas-rig would then be maintained in a state of vacuum to ensure no contamination. A photograph and schematic diagram of the gas-rig is shown in Figure 3.2.

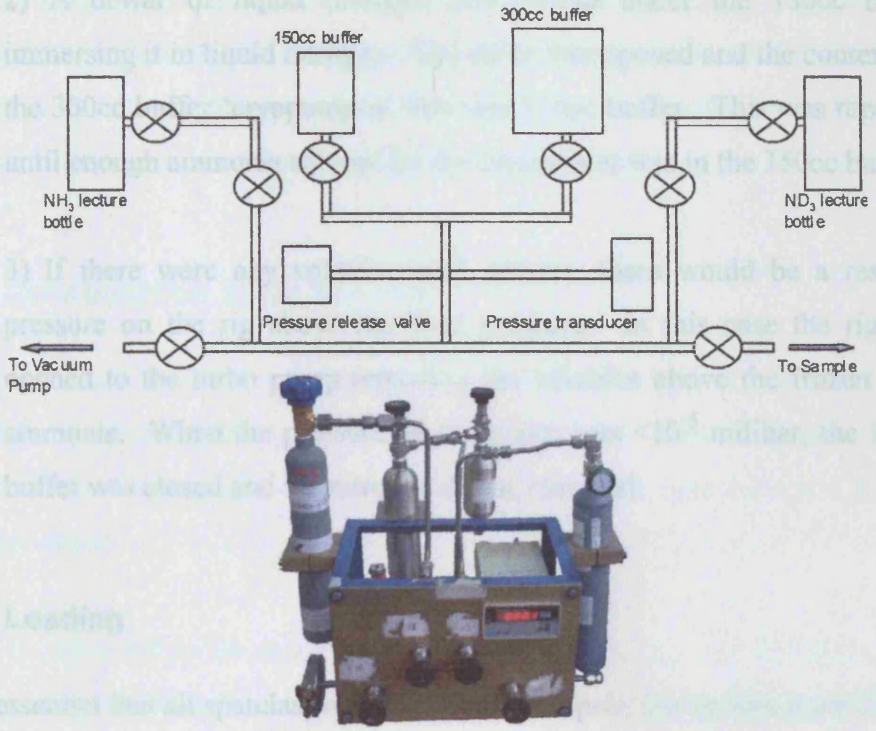

Figure 3.2: The gas handling equipment: schematic diagram and photograph.

3.2.3 Purification of Ammonia Solvent

The ammonia, NH_3, was bought from Aldrich at the highest purity available. The deuterated samples were all of atomic % D greater than 98% and were bought from Promochem. It found that the ammonia often had small amounts of volatile gases dissolved in it. Any volatile impurities affected the pressure reading on the gas-rig and hindered the condensation of ammonia. Before the experiment the amount of ammonia required for the condensation was decanted from the large NH_3 lecture bottle to the 150cc buffer. This ensured that if there was a failure in the gas-rig, only a small amount of ammonia gas would be released. To do this, as well as purify the gas, the following procedure was used:

1) An amount of solvent (<1.6bar) was decanted from the ammonia lecture bottle into the 300cc buffer and the pressure in the rig recorded.

2) A dewar of liquid nitrogen was placed under the 150cc buffer immersing it in liquid nitrogen. The valve was opened and the contents of the 300cc buffer 'cryopumped' into this 150cc buffer. This was repeated until enough ammonia solvent for the experiment was in the 150cc buffer.

3) If there were any volatile gases present, there would be a residual pressure on the rig above the base pressure. In this case the rig was opened to the turbo pump removing the volatiles above the frozen solid ammonia. When the pressure on the pump was $<10^{-5}$ milibar, the 150cc buffer was closed and the nitrogen dewar removed.

3.2.4 Loading

It was essential that all spatulas, weighing boats, scalpels, the sample can/cell, and the fittings used, were thoroughly cleaned to remove any impurities. This was done by washing with deionised water, then acetone and iso-propanol before drying in a vacuum oven at about 80°C for at least 4 hours. The utensils were then placed in a dry Argon glovebox with oxygen and water levels of <1ppm. The metal and C_{60} would be weighed to the nearest ten thousandth of a gram and placed in a tube or cell which is then sealed with a valve before removing from the glovebox.

3.2.5 Calculating the Amount of Gas Required

Having calculated the numbers of moles of ammonia required for a given concentration of solution, the ideal gas equation was used to calculate the differential gas pressure, measured on the gas-rig, which was equivalent to the amount of ammonia liquid that was required:

$$\Delta P = \frac{nR\Delta T}{V}, \qquad 3.1$$

where the pressure – P, is in known volume – V (the 300cc buffer), R is the molar gas constant ($8.314 m^2 kg s^{-2} mol^{-1} K^{-1}$), and T is the temperature of the gas. The pressure in the rig was always kept below ~1.6bar to ensure that using the ideal gas equation was a valid approximation.

3.2.6 Condensation of the Solvent

The material and geometry of the container (cell), the type of valve, and the method for maintaining the temperature at ~230K varied. Here follows a generic method for condensing a known amount of ammonia gas onto fullerene powder and alkali metal:

1) Weighed stoichiometric amounts of alkali metal and fullerene, C_{60}, powder are loaded into a cell in a dry Argon glove box. The valve on the cell is then closed.

2) The cell is connected to the gas-rig via a 1/8" stainless steel capillary and evacuated up to the valve. When the pressure reaches ~10^{-6} mbar, the valve at the top of the cell is opened to evacuate the argon above the sample again to ~10^{-6} mbar. The cell is then cooled to 230K.

3) The pump is closed to the gas-rig and the gas-rig to the sample. The required pressure or 1.6bar of NH_3 is let from the 150cc into the 300cc buffer. The 150cc buffer is then sealed and the valve to the capillary opened slowly, allowing the solvent to condense in the cell and the metal and fullerite dissolve. The initial and final pressure of ammonia gas in the 300cc buffer is recorded. This process is repeated until the amount of ammonia required has condensed onto the sample.

4) The valve on 300cm^3 buffer is then closed and the valve to the capillary opened. The pressure displayed on the transducer is now a measure of the vapour pressure above the liquid sample. This permits the monitoring of

any decomposition of the sample (evolution of hydrogen), or any cold leaks that may develop.

5) After the experiment, a dewar of liquid nitrogen is placed under the $150cm^3$ cylinder and the ammonia is carefully cryopumped from the cell and the arms of the gas-rig, until all the solvent is safely trapped. This cylinder is then sealed.

3.2.7 A_XC_{60} Salts

Pumping off the ammonia until the salt is 'dry' leaves an ammoniated C_{60} salt.[8] This compound is soluble in liquid ammonia and can be used to remake the solutions studied here. Solutions prepared using this method took much longer to homogenise. However, this method allows small, but stoichiometrically accurate, solutions to be prepared. This was achieved using a small amount of salt from a larger pre-made batch, in which the errors on the components' masses are much less. Where possible, when condensing directly onto the salt, the cell containing the solution was placed in a low temperature ultrasonic bath to accelerate the dissolution. De-ammoniation of the salt, to leave the A_XC_{60} salts requires heating under dynamic vacuum at 150°C for ~48 hours.[7]

3.3 Neutron Scattering

Neutron scattering is the predominant experimental technique used in this work. Therefore the experimental details and data reduction procedures that were followed are explained in detail:

3.3.1 Neutron Production

The neutron experiments in this work were performed on two different instruments at two different facilities which produce their neutrons via two different processes. The wide angle neutron diffraction was performed on

SANDALS at the ISIS facility at the Rutherford Appleton Laboratory, Didcot, UK. ISIS produces its neutrons by the process of spallation. The small angle neutron scattering was performed on the D22 instrument on the reactor source at Institute Laue-Langevin (ILL), Grenoble, France.

3.3.1.1 Neutron Production: Spallation

Neutrons are produced at ISIS by the bombardment of a pulsed beam of protons onto a heavy metal (tantalum) target.[119] This process is called spallation and it releases neutrons with a range of energies. The neutrons are slowed down to useable speeds with moderators and then collimated to produce a short pulse of neutrons which has a range of energies. The energy spread means that different neutrons arrive at a fixed detector at different times. The pulses of neutrons are produced at a rate of 50Hz. On the assumption of elastic scattering, their 'time of flight' (tof) can be related to the momentum transfer Q:

$$tof = \frac{L}{v} = \frac{m_n L \lambda}{h}, \qquad 3.2$$

therefore:

$$Q = \frac{4\pi \ sin\theta}{\lambda} = 4\pi \frac{m_n L sin\theta}{h \times tof}, \qquad 3.3$$

where L is the total flight path between the moderator and the detector, v is the velocity of the neutron and m_n is the neutron mass.

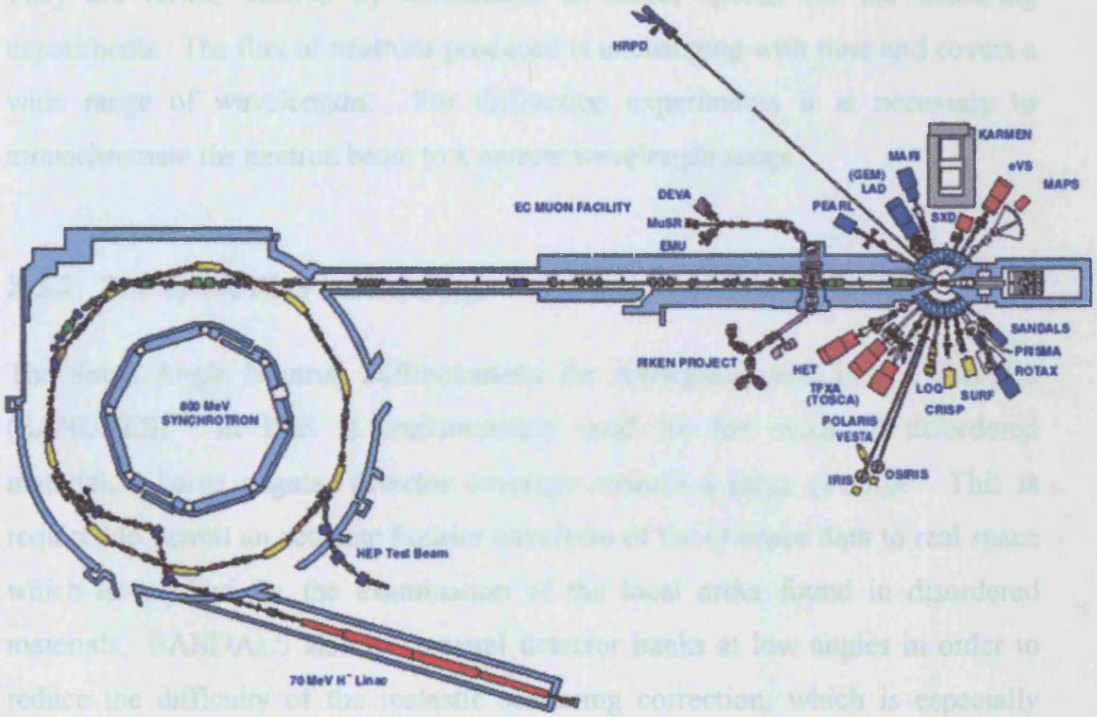

Figure 3.3: Neutron production at the ISIS facility from ref [119].

Figure 3.3 shows the method of production of the pulsed proton beam at ISIS. The protons start out as hydrogen H^- ions formed by the ionisation of hydrogen gas. The H^- ions are then accelerated along a linear accelerator to energies of ~70MeV before injection into the synchrotron. Upon entry to the synchrotron the beam passes through aluminium oxide foil stripping the H^- ions of their electrons. A harmonic RF system pushes the resulting protons into bunches as they are accelerated around the ring to energies of ~800MeV. At this energy the protons are 'kicked out' of the ring towards the tantalum target. For more details, see reference [119].

3.3.1.2 Reactor Source

The neutrons at the ILL are produced by a nuclear reactor. The reactor operates at a power of 57MW producing neutrons from the fission of a fuel element enriched with ^{235}U. The neutrons are slowed down in order to maintain the fission reaction.

They are further slowed by moderators to useful speeds for the scattering experiments. The flux of neutrons produced is unchanging with time and covers a wide range of wavelengths. For diffraction experiments it is necessary to monochromate the neutron beam to a narrow wavelength range.

3.3.2 The SANDALS Instrument

The Small Angle Neutron Diffractometer for Amorphous and Liquid Samples (SANDALS)[120] at ISIS is predominantly used for the study of disordered materials. Large angular detector coverage ensures a large Q-range. This is required to permit an accurate Fourier transform of the Q-space data to real space which is required for the examination of the local order found in disordered materials. SANDALS also has several detector banks at low angles in order to reduce the difficulty of the inelastic scattering correction, which is especially relevant if the sample contains hydrogen. The neutrons scattered at low angles are less energetic than those scattered at high angles, and therefore result in less inelastic recoil. SANDALS uses neutrons which are slowed by a liquid methane moderator to wavelengths of 0.05 – 6Å. The instrument has 18 detector banks comprising a total of 1260 zinc sulphide detectors giving angular coverage of 3.8° to 39°. This corresponds to a calculated Q-range of ~0.1 to 50 $Å^{-1}$. There have been some problems with the low angle detectors, which, at the time of writing this thesis, have led to a complete overhaul of the instrument. The measurements in this thesis, therefore, typically have a low-Q cut off at 0.5$Å^{-1}$.

3.3.2.1 SANDALS Sample Environment

The sample cell was made from a titanium-zirconium alloy and was of flat plate geometry with a 1.0mm path length and 1.0mm wall thickness. These short lengths are required to minimise multiple scattering and absorption. The cell designs and photograph are shown in Figure 3.4. The composition of the cell was such that the can is overall a null coherent scatterer (68% Ti and 32% Zr). Figure 3.5 shows the can on the end of the CCR candlestick and a schematic of the SANDALS instrument.

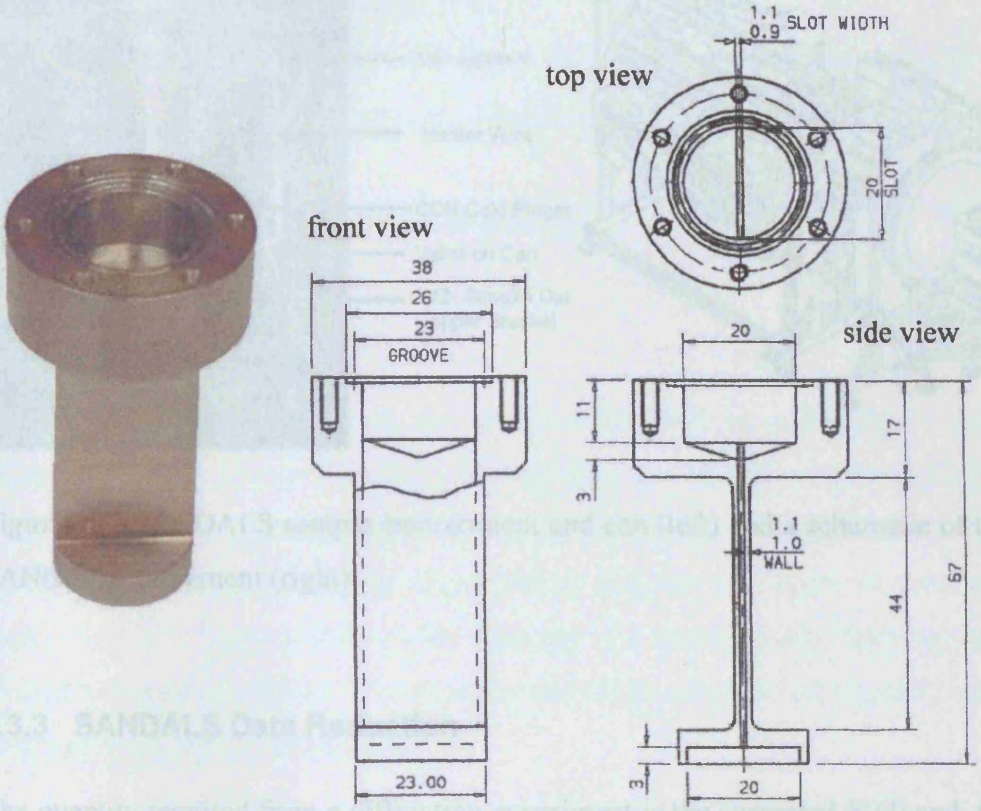

Figure 3.4: Titanium/Zirconium SANDALS can photograph and design. Distances are in mm.

The cell was loaded in an argon glovebox and a gold O-ring seal used to attach the valve assembly. The sample was then connected to the stainless steel capillary on the end of the candle stick (see Figure 3.5). To cool the sample to 230K a closed cycle refrigerator (CCR) was used. The sample was attached to the cold head using a copper bracket containing computer controlled heating elements, attached at the top and bottom of the bracket, to maintain the temperature at 230K. To prevent ammonia condensing in the capillary rather than the can, it was necessary to apply heat to the capillary via a heating wire. By setting the temperature on the bottom of the bracket to ~5K above the top, it was possible to use convection currents to accelerate the dissolution process.

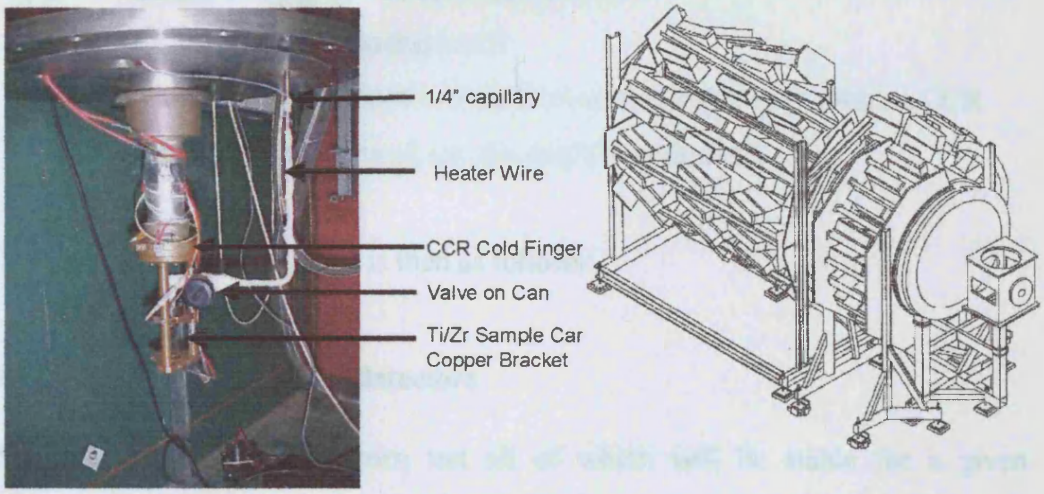

Figure 3.5: SANDALS sample environment and can (left) and a schematic of the SANDALS instrument (right).

3.3.3 SANDALS Data Reduction

The quantity required from a diffraction experiment is the corrected $F(Q)$ and, for a reliable Fourier transform to real space, this must be of high quality and normalised. The method followed for data correction may be separated into logical steps. These steps, the routines used, and the theory behind them are explained in more detail then given here in the ATLAS manual.[113] Data reduction methods for SANDALS experiments are also detailed in the SANDALS Survival Guide.[121] Since the data in this work was analysed, a more user-friendly routine for reducing the data has become available. This is called GUDRUN[122] and, as well as requiring only one input file for the entire data reduction process, it also analyses the results detector by detector rather than first averaging the results over the individual detector banks, as is the case in the ATLAS routines.

To obtain a fully corrected $F(Q)$ the following scattering experiments are required:

1. Sample + container + CCR

2. Empty cell + CCR (sample background)
3. CCR (empty cell background)
4. Vanadium slab, which is measured on the candle stick with no CCR
5. Vanadium background, i.e. the empty candle stick

The data reduction procedure is then as follows:

1) PURGE_D: Purging the detectors

SANDALS has 1260 detectors, not all of which will be stable for a given experiment. The program PURGE_D outputs a list of the unstable detectors which must not be included in the analysis. In this work, if there is more than a 10% variation in the spectra for an individual detector in a series of runs, and more than a 2% variation from all the detectors in a specific bank, the detector is discarded from the analysis. This is performed for all samples and typically ~800 detectors were used in the analysis.

2) NORM: Normalisation to the incident spectrum

The routine NORM corrects for detector dead-time, removes the unstable detectors (using the output from PURGE_D), and then normalises the data by dividing by the monitor spectrum. This normalisation is required, at this stage, to allow for variations in the wavelength flux which may arise from temperature fluctuations in the moderators. The program then converts the tof signal to Q-space and merges the spectra from individual detectors into 18 groups corresponding to the 18 detector banks.

3) CORAL: Absorption and multiple scattering corrections

The routine CORAL corrects for any neutrons that have been absorbed by the sample or that are scattered more than once. The program requires a wavelength dependent absorption cross section for all the samples. These are obtained either by using an already measured cross section, which was the case for the vanadium

and Ti/Zr can, or using the ratio of the transmission data from sample and background, and fitting a polynomial.

4) ANALYSE: Calibration of the instrument

The actual scattering measured by SANDALS is modified by an instrument dependent term $P(Q)$:

$$I^E(Q) = \left[\frac{d\sigma}{d\Omega}\right] P(Q) \qquad 3.4$$

Vanadium is a completely incoherent scatterer and because of this, the differential cross section of vanadium can be estimated with a reasonable degree of accuracy. It is therefore used in this routine to estimate $P(Q)$ and then normalise all the data sets to units of barn. The routine also applies the multiple scattering and absorption corrections as well as subtracting the background. The output is given as the 18 groups of detector banks.

5) SUBSELF: Inelastic and self-scattering corrections

The static approximation does not hold exactly true for neutron scattering from a liquid, and the measured diffraction pattern includes inelastic contributions, which must be corrected. The standard inelastic correction is Placzek correction.[123] Placzek showed that the inelastic contribution is essentially independent of the detailed dynamics but could be estimated to a first approximation using only nuclear mass, sample temperature, incident neutron energy and geometry, and efficiency of the neutron detection process. This approximation breaks down for light elements and cannot be applied to samples containing large amounts of hydrogen, such as those measured in this work. The routine SUBSELF uses an empirical method assuming that the inelastic contributions can be approximated by a smooth function. The routine then fits a low order polynomial to the underlying shape of the data without fitting any features. This is then subtracted from the data in all the detector groups.

6) MERGE: Merging the detector banks

The final stage is to merge the data from the individual detector banks to a continuous average, $F(Q)$. The data can now be transformed to real space or converted into partial structure factors.

3.3.4 The D22 Instrument

D22 is a Small Angle Neutron Scattering (SANS) instrument at the ILL. A schematic of D22 is shown Figure 3.6. The instrument has one of the highest neutron fluxes in the world for a SANS instrument. D22 uses a velocity selector to choose a monochromatic beam of wavelength between 4.5 and 40Å.

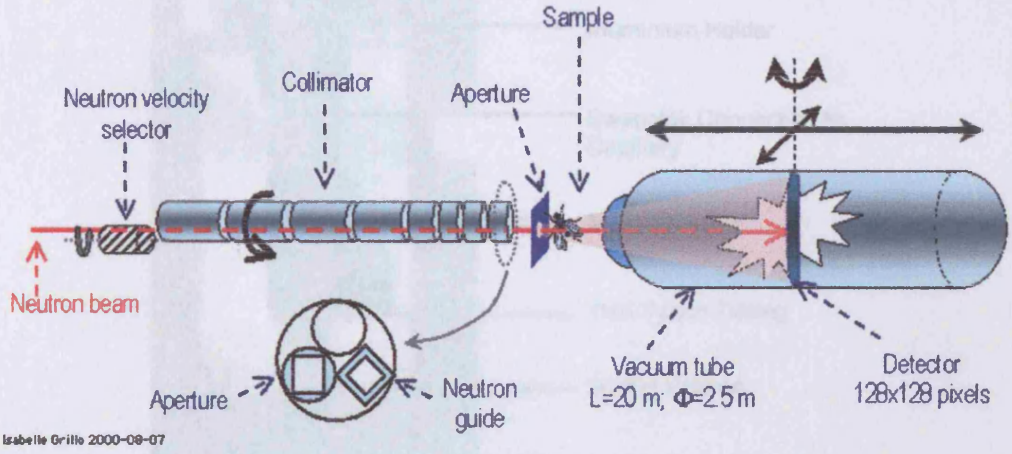

Figure 3.6: The D22 instrument at the ILL from ref. [124].

The neutron detector is housed in an evacuated 20m long, 2.5m wide cylindrical chamber. The detector itself is a ^{3}He area multidetector and has an area of 96 × 96 cm with a pixel size of 0.75 × 0.75 cm. The detector moves inside the vacuum tube so that it covers distances of between 1.35m and 18m from the sample. The detector can also be translated, by a small amount, perpendicular to the incident beam in order to increase the maximum Q coverage. In all, the instrument can then cover a Q-range from 10^{-4} to 0.85Å^{-1} but this requires several different configurations of the detector's position and wavelength selection.

3.3.5 D22 Sample Environment

The sample cell used was of flat plate geometry with a 2.0mm path length, custom designed for the experiment. The cell was made from crystalline quartz which has very little scattering at low-Q. The cell comprises of a flat plate, 1mm wall thickness, quartz cuboid, fused to an 8mm OD quartz tube. The tube permits the connection of the quartz to the gas-rig as well as serving as a mixing volume for the dilution of the sample. The sample set up is shown in Figure 3.7.

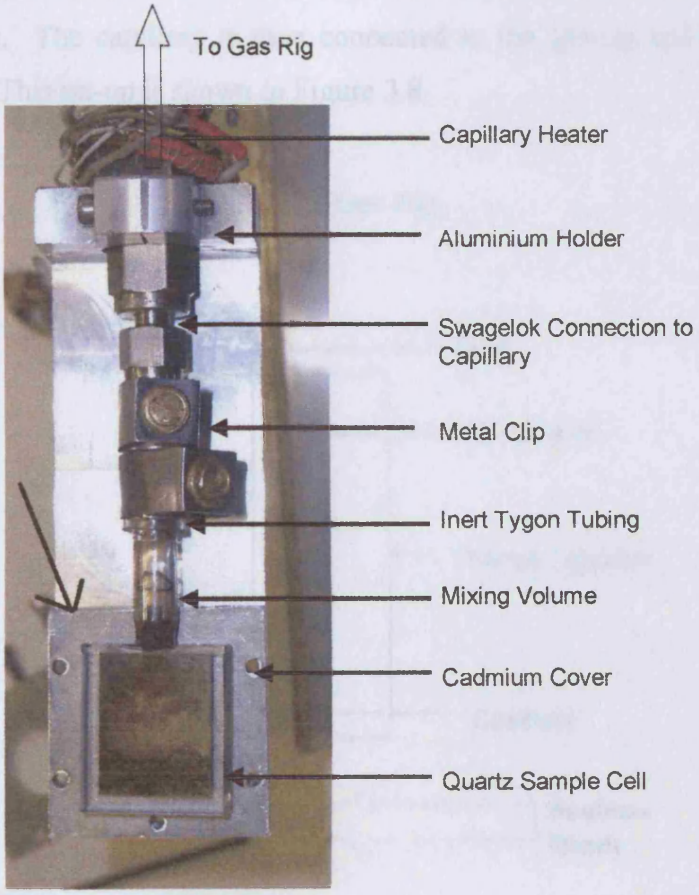

Figure 3.7: Setup of the sample cell for use on the D22 SANS instrument.

The sample cell was connected to the bottom of the cryostick using inert Tygon® tubing and metal clips, as shown in Figure 3.7. The sample cell is fixed in place on an aluminium bracket attached to the cryostick. During the

experiments a cadmium cover, only the back half of which is shown in the figure, was screwed in place in front of the sample cell. This has a circular aperture in it which is slightly less than the beam size.

A specially modified glovebox at the ILL permits the connection of the sample cell to the cryostick without exposure to air. Once connected to the cryostick, the sample valve assembly is leak tested. The cryostick is then lowered into the cryostat which is maintained at ~230K. Inside the cryostick the capillary is wrapped in a heater wire which prevents the condensation of ammonia gas in the capillary. The capillary is then connected to the gas-rig and the ammonia condensed. This set-up is shown in Figure 3.8.

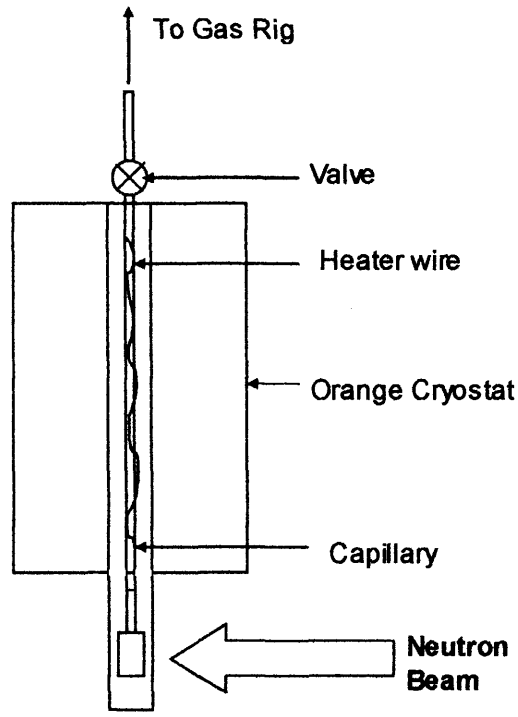

Figure 3.8: A schematic of the sample set up on the D22 SANS instrument.

3.3.6 D22 Data Reduction

The small angle approximation means that the data reduction is far less complicated and time consuming for SANS experiments than the wide angle

diffraction data. The D22 data was analysed using the program GRASP,[125] a user-friendly program designed for the reduction and inspection of multi-detector SANS data. The general stages in the analysis procedure are presented here in brief. For more detail, the reader is referred to the GRASP manual.

The flux of neutrons scattered into a solid angle element $\Delta\Omega$ during a monochromatic SANS experiment is given by:

$$I(Q) = I_0 \Delta\Omega \eta t A T \frac{\partial\sigma}{\partial\Omega}(Q), \qquad 3.5$$

where T is the transmission of the neutrons through the sample, η is the detector efficiency, I_0 is the incident flux, t is the pathlength and A is the cross-sectional area of the beam.[115] The scattering is measured using an area detector element of dimensions $dx \times dy$ at a distance L and scattering angle θ from the sample such that $\Delta\Omega = \frac{dx \times dy}{L^2}$.

The differential cross section $\frac{\partial\sigma}{\partial\Omega}(Q)$ provides the SANS information and is the quantity we aim to extract. The data is analysed per detector element. In the experiment performed in this work, the background was taken to be the scattering from the pure solvent, circumventing the need for an empty instrument measurement. The transmission, T, is measured with each SANS sample measurement. The sample transmission used here is calculated as the transmission of the sample divided by the transmission through the solvent. The detector efficiencies are calculated using a water standard, the scattering of which is known. This is also used to calibrate the scattering to convert the scattering intensity to a value of scattering cross section per unit volume per unit solid angle, in units of cm^{-1}. The GRASP program, in order to merge the results from the different detector positions, implements a solid angle correction as well as accounting for the decrease in neutron flux with distance from the sample. As the scattering in this case is isotropic, the corrected and normalised 2-dimensional

data was then reduced to an averaged 1-dimensional plot of normalised intensity, I vs Q.

3.4 Nuclear Magnetic Resonance Sample Environment

The Liquid NMR Spectrometer requires the sample to be made in a quartz tube of 5mm diameter and ~17cm in length. The tube is lowered deep inside the spectrometer and spun. This requirement eliminates the use of a gas feed technique. A process was therefore developed in which the solutions were made, frozen, and then sealed in the NMR tubes. If sealed correctly, when the tubes warmed up to room temperature, the solution is held liquid by the pressure in the tube (ammonia liquefies at ~9bar).

The small volume of the quartz tubes meant that typically only ~40mg of solute was required for the solutions. To ensure that the stoichiometric ratio of fullerides to metal was accurate, larger batches of salts were therefore made first. The salt was then weighed and loaded in the NMR tube in a glove box. This was connected to the gas-rig via an o-ring locking connector. The solution was sealed in the tube as follows:

1) The ammonia is condensed onto the fulleride powder in the normal way using an acetone/dry ice bath to maintain the temperature at ~230K. The quartz tube is then removed from the bath and quickly wiped (to remove the flammable acetone) before being immersed in a liquid nitrogen dewar, so that the solution freezes completely.

2) The back buffer is emptied and the valve to the pump then opened so that there is a vacuum above the solid sample.

3) With the torch on an intense blue flame the NMR tube is then heated at one of the points indicated in Figure 3.9, about 10cm above the frozen

sample, until it glows white. When the quartz glows white, the cell wall collapses slightly. At this point the flame is removed.

4) This is repeated at the two other points on the tube. If one increases the caving of the tube walls symmetrically across the three points, the tube walls collapse to meet in the middle. At this point the cell is sealed.

5) The sealed tube is then removed by heating just above the seal until the quartz melts completely.

6) The sealed tubes are then kept frozen in liquid nitrogen until the experiment. They are then warmed to room temperature to place in the spectrometer. The spectrometer has a cryostat and the actual measurements were taken at ~223K.

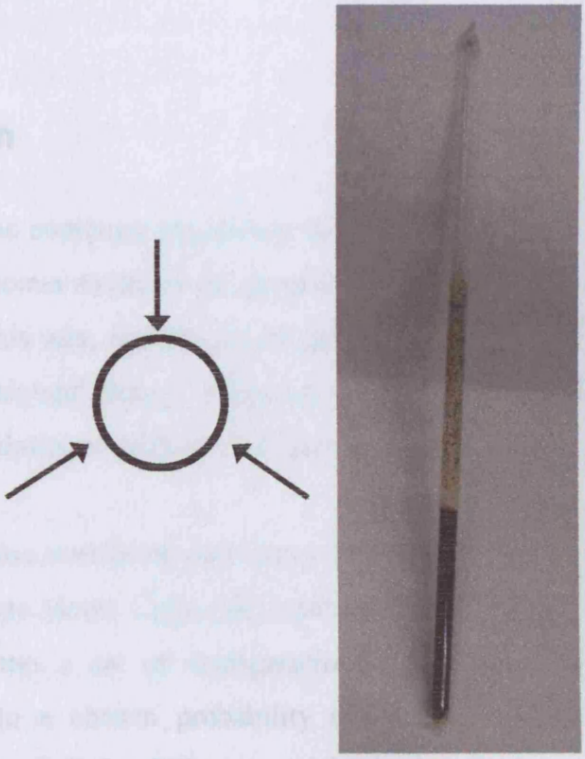

Figure 3.9: NMR sample manufacture. The three points to apply the acetylene/oxygen blow torch to the NMR tube, viewed from above (left). A sealed NMR tube containing potassium-ammonia-fulleride solution (right).

Chapter 4

Simulation Theory

4.1 Introduction

The aim of an atomistic computer simulation is to determine ensemble averages for a system, starting from a model of the geometries and interactions between the atoms/molecules. In this way, insight can be gained into systems that cannot be easily described by analytical theory. However, the usefulness of simulations is dependent on the availability of reliable input potentials.

The two atomistic simulation techniques that provide thermodynamic and structural information are Monte Carlo (MC) and Molecular Dynamics (MD). An MC simulation generates a set of configurations for a system of interacting molecules according to a chosen probability ensemble. An MD simulation calculates the momenta of all the different particles in the system and follows the trajectory of those particles with time, according to Newton's equations of motion. Whilst an MD simulation provides dynamical information and MC does not, MC has the advantage of typically taking less computer time to equilibrate for

homogeneous systems. The main aim of this work is to establish the equilibrium structure of the solutions, therefore MC simulations are used.

The Metropolis Monte Carlo (MMC) method produces a statistical ensemble with a Boltzmann distribution of energies. The MC code used throughout this work was *Monte*[126] which has successfully been used to examine the solvent ordering surfaces,[127] the hydration of ions in polar liquids, layered structures such as clays,[128] and metal-ammonia solutions.[129] The basic theory is detailed in the first half of this chapter.

The second half of this chapter presents the theoretical background to the recently developed technique of Empirical Structural Potential Refinement (EPSR).[130,131,132] This method starts with a standard MMC simulation of a system and then refines the interatomic potentials in that system until it reproduces an ensemble that is consistent with experimentally measured diffraction data. A complete set of pair distribution functions can then be extracted and questions can be asked concerning the 3-dimensional structure, in addition to the distance, r, averaged over all directions in an experiment. The basic theory as well as important ideas behind the technique will be discussed.

The EPSR technique, used in conjunction with isotopic substitution, although only recently developed, has already thrown light on several problems, for example, alcohol-water mixtures,[133,134] electron cavities and hydrogen-bonding in lithium-ammonia solutions,[135] the structure of bulk water,[136] and solvated ions in water.[137] The EPSR method does not claim to allow exact thermodynamical quantities to be determined, but may provide a more accurate version of the classical potentials used in simulations.[138]

4.2 Metropolis Monte Carlo

The MC technique was first developed for the canonical ensemble (N,V,T), via the Metropolis method, where the number of particles – N, volume of ensemble – V, and temperature – T, are fixed. The technique has been extended to other ensembles such as the isothermal-isobaric, (N, p, T) in which the ensemble's volume can fluctuate and pressure (p) is kept constant.

The work in this thesis uses both the canonical and the isothermal-isobaric ensembles. A basic outline of the method is first presented for the (N, V, T) simulations and followed by the extension to the (N, p, T) distribution.

A system of N molecules is set up such that each molecule is randomly placed in a cubic box of predefined side length, L, and there are no molecular overlaps. The number density is fixed by the density of the system. The molecular configurations are specified by a coordinate vector $\boldsymbol{X}^N$:

$$\mathbf{X}^N = (\mathbf{X}_1, \mathbf{X}_2, ...\mathbf{X}_N), \qquad 4.1$$

where $\boldsymbol{X}_1$ are the coordinates for molecule 1, $\boldsymbol{X}_2$.for molecule 2 etc. Within this molecule, individual atomic sites are specified with positional, $\boldsymbol{R}_i$, and angular, $\boldsymbol{\Omega}_i$, coordinates:

$$\mathbf{X}_i = (\mathbf{R}_i, \Omega_i). \qquad 4.2$$

An average property of the ensemble is then calculated from the configuration. In the (N, V, T) ensemble this is U, the total average internal energy of the system. This is calculated using specified interatomic pairwise potentials, summed over all the pairs of atoms in the ensemble:

$$U = \sum_{i=1}^{N} \sum_{j>i}^{N} V_{ij}(r_{ij}). \qquad 4.3$$

Here, V_{ij} is the potential between a pair of atoms i and j, and r_{ij} is the distance between these atoms.

A molecule is then selected and a trial move performed on it. The selection process is an essential part of the simulation. Selecting a configuration at random would be likely to pick out a high energy state, which would not occur often at equilibrium. This would be a very inefficient sampling method. Instead, it is arranged such that the state is selected with a probability equal to its probability of appearing in thermal equilibrium. This is done via an irreducible Markov chain, a weighted sampling procedure that satisfies the following conditions:

1) Each step, in a series of configurations, is dependent only on the single previous step.
2) That the system is *ergodic*. That is, every state can be reached from any other in a finite number of steps.
3) That the condition of *detailed balance* or *microreversibility* is observed: once in equilibrium (once the Markov process has converged), the probability of transition from state r to r' is equal to the probability of the transition of state r' to r.

The Metropolis method for constant N, V and T ensemble, satisfies these conditions and proceeds via the following algorithm:

The probability of the configuration before the move is given by:

$$P_a \propto \exp\left(\frac{-U_{X_a^N}}{kT}\right). \qquad 4.4$$

Then the move is performed. The probability of a new (b) configuration is given by:

$$P_b \propto \exp\left(\frac{-U_{X_b^N}}{kT}\right). \qquad 4.5$$

Therefore:

$$\frac{P_b}{P_a} = exp\left(\frac{-(U_{X_b^N} - U_{X_a^N})}{kT}\right) = exp\left(\frac{-\Delta U}{kT}\right). \qquad 4.6$$

If $\Delta U<0$, the configuration is accepted.

If $\Delta U>0$, the configuration is accepted with probability of $\frac{P_b}{P_a}$ or rejected and we return to our previous configuration.

The procedure is repeated iteratively and eventually U reaches its asymptotic value and equilibrium is reached. The physical size of the trial move is kept small and adjusted so that roughly half the moves will be accepted.

In the isothermal-isobaric ensemble, an average property of the system is selected which takes into account the change in volume. Therefore the algorithm is identical but ΔU in equation 4.6 is given by ΔH:

$$\Delta H = \left(U_{X_b^N} - U_{X_a^N}\right) + p\left(V_{X_b^N} - V_{X_a^N}\right) - (N + \frac{2}{3})k_B T \ln\left(\frac{V_{X_b^N}}{V_{X_a^N}}\right), \qquad 4.7$$

where V is the (dynamic) volume and p is the (constant) pressure.

4.3 Interatomic Potentials

The interatomic interaction potentials, V_{ij}, used in this work consist of Lennard-Jones and Columbic potentials (see equation 4.8). The '6 term' represents van der Waals attractions between atoms via electron dispersion forces. The '12 term' represents the short range repulsive interaction between two atoms due to the

Pauli Exclusion Principle. A typical interatomic potential, in this case for the interaction between two ammonia nitrogen atoms, is shown in Figure 4.1. In the case of ammonia, effective Coulomb potentials are used on the component atoms in order to represent the electrostatic moment of the molecule.

$$V_{ij}(r_{ij}) = \frac{q_i q_j}{r_{ij}} + 4\varepsilon_{\alpha\beta}\left[\left(\frac{\sigma_{\alpha\beta}}{r_{ij}}\right)^{12} - \left(\frac{\sigma_{\alpha\beta}}{r_{ij}}\right)^{6}\right], \qquad 4.8$$

where α, β represent the types of atom i, j respectively. The values of the range parameter, $\sigma_{\alpha\beta}$, and well depth parameter, $\varepsilon_{\alpha\beta}$, are taken from the literature for the various molecules.

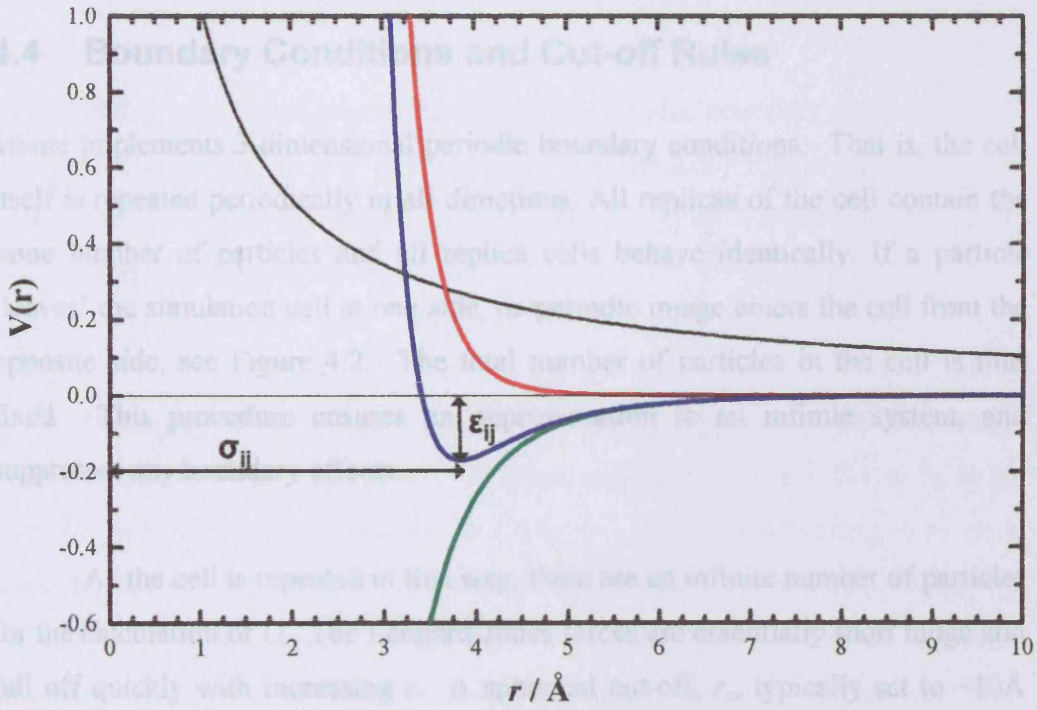

Figure 4.1: Interatomic potentials between two ammonia nitrogen atoms: Interatomic potentials between two ammonia nitrogen atoms: $V(r_{ij}) = A + B + C$, where $A = \frac{q_i q_j}{r_{ij}}$, $B = 4\varepsilon_{\alpha\beta}\left(\frac{\sigma_{\alpha\beta}}{r_{ij}}\right)^{12}$ and $C = -4\varepsilon_{\alpha\beta}\left(\frac{\sigma_{\alpha\beta}}{r_{ij}}\right)^{6}$. Key: black curve – A, red – B, green – C and blue – the Lennard-Jones potential, B + C.

When the species of two atoms differ, the values of these parameters are calculated via the Lorentz-Berthelot mixing rules in terms of their values for the individual atoms:

$$\varepsilon_{\alpha\beta} = (\varepsilon_\alpha \varepsilon_\beta)^{\frac{1}{2}} \quad , \quad \sigma_{\alpha\beta} = \frac{1}{2}(\sigma_\alpha + \sigma_\beta). \qquad 4.9$$

Although classical potentials can closely describe the system, their accuracy is limited. Typically, potentials are calculated from experimental data for specific systems. When other systems are being investigated, a comparison to experiment is the only way to examine how closely the selected potentials can describe the simulated system.

4.4 Boundary Conditions and Cut-off Rules

Monte implements 3-dimensional periodic boundary conditions. That is, the cell itself is repeated periodically in all directions. All replicas of the cell contain the same number of particles and all replica cells behave identically. If a particle 'leaves' the simulation cell at one side, its periodic image enters the cell from the opposite side, see Figure 4.2. The total number of particles in the cell is thus fixed. This procedure ensures an approximation to an infinite system, and suppresses any boundary effects.

As the cell is repeated in this way, there are an infinite number of particles for the calculation of U. The Lennard-Jones forces are essentially short range and fall off quickly with increasing r. A spherical cut-off, r_c, typically set to ~10Å (see Figure 4.2), is therefore used in the calculation of U. Beyond this cut-off, the Lennard-Jones forces are small but not negligible. *Monte* calculates a small correction to the potential energy beyond r_c, by assuming that the density is uniform beyond this cut-off, i.e. the pair correlation function is 1 for $r>r_c$.

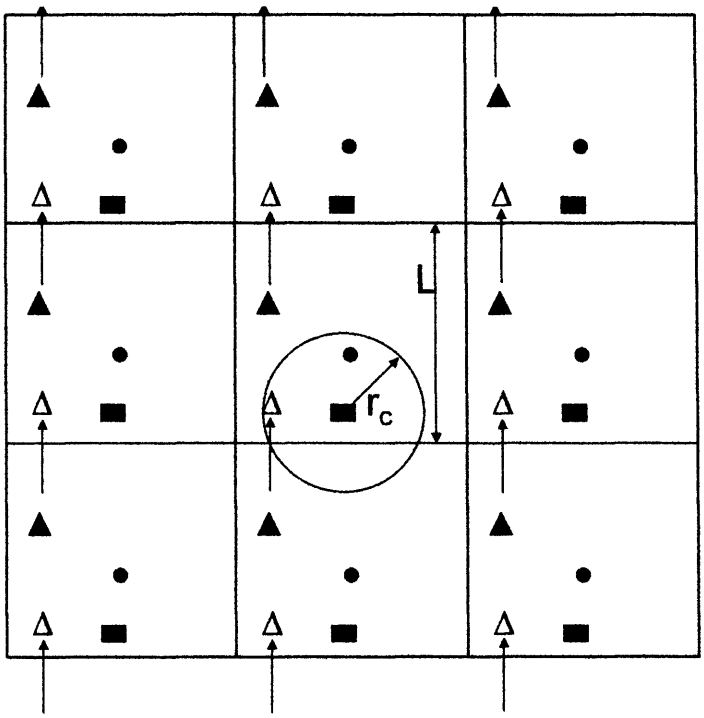

Figure 4.2: A diagrammatic representation of periodic boundary conditions. As the solid triangle leaves the box at the top, its periodic image (clear triangle) enters the box from the bottom. The cut-off, r_c, for Lennard-Jones energy calculations is also shown.

In the case of the Coulombic forces however, the forces are long range, falling off as r^{-2}. A similar cut off, therefore, can not be applied; forces from the periodic images must be considered. This is a slowly converging sum in 3-dimensions. *Monte* calculates this efficiently by implementing the Ewald sum technique[139] which exploits the periodicity of the system to ensure the rapid convergence of this sum. The Ewald sum essentially separates the overall infinite sum into two finite series: one in real space, the other in reciprocal space. The choice of the two cut-off values for this sum, as well as the parameter α which is used in the sums, is crucial in the sum's accuracy and hence the calculation of the internal energy, U.

4.5 Empirical Potential Structural Refinement

A diffraction experiment results in a 1-dimensional average function representing a sum of the individual correlations, from all the pairs of atoms in the sample under study. The technique of EPSR aims to derive as much information as possible from the diffraction measurements regarding the correlations between all the pairs of atoms, in three dimensions.

The EPSR method produces a 3-dimensional box of particles which is consistent with diffraction data measured for a particular experiment. The technique effectively uses the diffraction data as a constraint against which to refine a simulation of the system. Starting with an equilibrated MC simulation based on initial 'seed' potentials, the EPSR procedure then, by comparing the simulation to the diffraction data at every step, iteratively modifies these potentials by a small perturbation until the new potentials recreate the diffraction data. The technique has been developed for liquids and disordered systems and, as such, does not claim to 'solve' the diffraction data for the structure found. Disordered systems have no unique structural solutions and EPSR only claims to find a configuration which is consistent with the data. The technique allows known prior information such as molecular geometry, dispersion forces, overlap and electrostatic constraints to be 'built into the refinement procedure'.[130] The discrepancies between the diffraction pattern and the initial MC simulation are attempted to be accounted for by the EPSR technique.

4.5.1 The EPSR Procedure

An outline of the EPSR technique is given here. For a more detailed account of the theory, as well as a discussion on the nature and physical significance of the empirical potential, the reader is referred to the EPSR papers by Soper and the EPSR manual.[130,131,132]

The initial configuration is set up with the correct number composition, density and temperature. The positions and orientations of the molecules are

randomised and non-overlapping. A Metropolis Monte Carlo routine is then invoked. This initial routine is less sophisticated than *Monte* in that it does not rigorously take account of the periodic long range forces, but otherwise proceeds in the same way.

Whereas *Monte* uses molecules with fixed rigid geometries (bond lengths), the EPSR model will eventually be refined against diffraction data, so variations in intramolecular bond lengths must be allowed. The potential energy U, is then split into an intermolecular contribution (as defined in equation 4.8 above), using 'seed' potentials taken from the literature, and an intramolecular contribution. Eventually a third term, the empirical potential, will be added. The intramolecular potentials are defined by assuming the atoms in the same molecule will interact via a harmonic potential. The total (dimensionless) intramolecular energy is given by:

$$U_{intra} = C\sum_{i}\sum_{\alpha,\beta\neq\alpha}\frac{\left(r_{\alpha_i\beta_i} - d_{\alpha\beta}\right)^2}{2\omega_{\alpha\beta}^2}, \qquad 4.10$$

where $d_{\alpha\beta}$ is an average atomic distance, $r_{\alpha_i\beta_i}$ is the actual atomic separation of atoms α, β, and C is determined by comparing the simulated structures at high-Q. $\omega_{\alpha\beta}$ is an effective broadening function where

$$\omega_{\alpha\beta}^2 = \frac{d_{\alpha\beta}}{\sqrt{\mu_{\alpha\beta}}} \quad , \quad \mu_{\alpha\beta} = \frac{M_\alpha M_\beta}{\left(M_\alpha + M_\beta\right)} \qquad 4.11$$

and M_α is the mass of atom α, in atomic mass units. The use of such a broadening function removes the need to define a separate Debye-Weller factor for each intramolecular distance which greatly reduces computational time.

There are four types of move in EPSR: whole molecule translations, whole molecule rotations, rotations of molecular head-groups and intramolecular atomic

moves. The acceptance of intramolecular moves is based solely on the change in the intramolecular internal energy ΔU_{intra}.

The initial MC simulation is run until the energy of the system reaches its asymptotic value, at which point the user must convince himself/herself that there are no unphysical effects, for example, ammonia molecules inside the fulleride cage, and that the average structure is no longer changing. By this stage there should be a reasonable similarity between the data and the simulation. From the generated ensemble, individual radial distribution functions are calculated and then summed with the relevant neutron weighting factors and compared with the diffraction data. In the case of second order isotopic hydrogen/deuterium substitution the simulation is compared to the $S_{XX}(Q)$, $S_{XH}(Q)$ and $S_{HH}(Q)$. The refinement is then switched on.

The Empirical Potential is a perturbation added to the reference potential and the total internal energy is given by:

$$U = U_{ref} + U_{empirical}. \qquad 4.12$$

The Empirical Potential is calculated via the following method:

Every radial distribution function has a potential of mean force given by:

$$\Psi_{\alpha\beta}(r) = -kT \ln(g_{\alpha\beta}(r)). \qquad 4.13$$

This is true for both the data and the simulation. The difference between these two potentials is used to define the perturbation (the empirical potential). The new potential energy function is then:

$$U^{N}_{\alpha\beta}(r) = U^{O}_{\alpha\beta}(r) + \left(\Psi^{D}_{\alpha\beta}(r) - \Psi^{sim}_{\alpha\beta}(r)\right) = U^{O}_{\alpha\beta}(r) + kT\, ln\left(\frac{g^{sim}_{\alpha\beta}(r)}{g^{D}_{\alpha\beta}(r)}\right) \qquad 4.14$$

where the superscript D refers to the functions derived from the diffraction data; and *sim* refers to the functions derived from the EPSR configuration. The new potential $U^{N}_{\alpha\beta}(r)$ is then used in the simulation in place of the reference potential and the simulation is again brought to equilibrium. A new $g^{sim}_{\alpha\beta}(r)$ is thus obtained, which is in closer agreement to the diffraction data. This process is then repeated many times i.e. until $\left(\Psi^{D}_{\alpha\beta}(r)-\Psi^{sim}_{\alpha\beta}(r)\right)$ tends to zero and the simulation is consistent with the data.

A key point of EPSR is that the empirical potential must represent true differences between the simulation and the data, and *not* truncation effects in the real space transforms or statistical noise arising from the finite size of the simulation or systematic errors in the data. These errors would proliferate if included in the iterative refinement. The empirical potential is therefore calculated by using only the experimentally measured structure factors directly, and not their real space transforms. This is done via the following method:

The form of the empirical potential can be expressed as a series of power exponential functions:

$$U_{emp}(r) = kT\sum_{i} C_i p_{n_i}(r,\sigma_r), \qquad 4.15$$

$$\text{where} \quad p_n(r,\sigma_r) = \frac{1}{4\pi\rho\sigma^3(n+2)!}\left(\frac{r}{\sigma}\right)^n \exp\left[-\frac{r}{\sigma}\right]. \qquad 4.16$$

C_i are real constants and can be positive or negative, σ_r is a width function which can be specified by the user, and ρ is the atomic number density of the system.

This function, $p_n(r,\sigma_r)$, has a direct 3-dimensional Fourier transform to Q-space:

$$p_n(Q,\sigma) = 4\pi\rho\int p_n(r)\exp(i\mathbf{Q}.\mathbf{r})d\mathbf{r}. \qquad 4.17$$

In the EPSR procedure, the coefficients, C_i are estimated directly from the difference between the (Q-space) data and simulation, by fitting a series of the form:

$$U_{emp}(Q) = kT\sum_i C_i p_{n_i}(Q,\sigma_Q). \qquad 4.18$$

Once extracted, these coefficients are used in equation 4.15 to produce the empirical potential. This removes the need to transform the diffraction data and thereby eliminates the truncation problems associated with this.

Once the process has converged and the simulation fits the data, auxiliary routines are invoked to calculate distribution functions and other useful functions to interpret the data. This allows the extraction of a complete set of pair distribution functions. The spatial density function, which completely describes the 3-dimensional orientational distribution, can also be investigated via a spherical harmonic expansion.

4.5.2 The Spatial Density Function

An important tool in the EPSR arsenal is the ability to investigate the system's pair correlation function $g(r, \Omega_1, \Omega_2)$, Ω_i being the Euler angles, $(\theta_L,\varphi_L,\chi_L)$ for the ith molecule. This is done via a spherical harmonic expansion, and allows orientational correlations between the molecules to be investigated. The method has shed light on several systems such as the metal-ammonia solutions, alcohol-water mixtures and pure water.[133,135] It allows the visualisation in three dimensions of the probability of finding a second molecule between specified distances (in any orientation), with respect to a molecule of defined orientation.

The 'spatial density plots' are obtained by holding molecule 1 fixed at the origin in this pre-defined orientation, and ascertaining the most probable angular positions of the second molecule relative to the first within specified distances averaged over the entire ensemble, i.e. allowing θ_L and φ_L to vary. In this work,

the molecule at the origin is ammonia and is fixed (see figure 4.3). The angles θ and ϕ are defined relative to the z-axis (dipole moment) of the ammonia molecule, and the x-z plane (in which the first intra-molecular N-H bond lies), respectively.

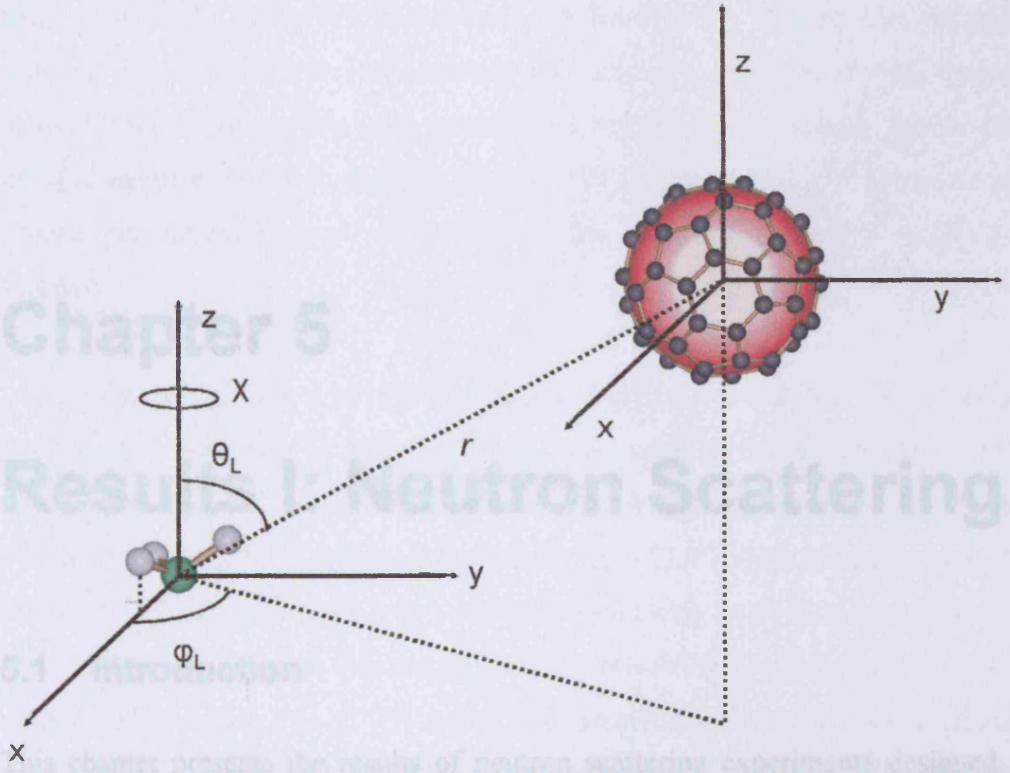

Figure 4.3: The coordinate system used in this work to investigate the spatial density function of the system. This function plots the most likely position of molecule 2, in any orientation, between specified distances relative to a fixed molecule at the origin. The figure shows how the orientation of the ammonia molecule at the origin is fixed.

Chapter 5

Results I: Neutron Scattering

5.1 Introduction

This chapter presents the results of neutron scattering experiments designed to establish the structure of metal-ammonia-fulleride solutions. The suitability for many of the suggested applications, for example, studying individual ions and deposition onto surfaces, depends on the fullerides being mono-dispersed as well as concentrated in solution. One of the key questions to be answered, therefore, is whether any large fulleride clusters form in solution.

The solvation of fullerenes/fullerides is poorly understood. A detailed measurement of the microscopic structure of the solution will answer fundamental questions such as: how are the solvent molecules arranged to accommodate the fullerides, and what is the role of hydrogen-bonding in the solutions?

Fullerenes currently find themselves in a frustrating position when it comes to revealing their structure in solution since their length-scale falls between the conventional wide- and small-angle instrumentation. Atomistic measurements

of the local structure of a liquid or disordered material are traditionally made using wide angle diffraction. Such instruments typically have a low-Q limit of about 0.5Å^{-1}, which loosely corresponds to a limit of maximum correlation length of ~12Å. The measurements also rely on a large Q-range for an accurate Fourier transformation to real-space, to examine the local order. Larger flux radiation sources, better instruments and increasingly powerful methods of data analysis have improved the quality and quantity of information obtained from liquid diffraction, particularly in the UK at the ISIS facility. The main part of this chapter presents wide angle diffraction studies of potassium-ammonia-fulleride solutions.

The low-Q limit of ~0.5Å^{-1} is too high to reveal the inter-fulleride correlations, especially if the fullerides form aggregates in solution. At a concentration of 250 NH_3 molecules per C_{60}, if the fullerides are distributed evenly in solution, there will be one fulleride per ~21Å^3. This ordering would be found at ~0.3Å^{-1}. Any clusters of fullerides would only be evident at even lower-Q. Small Angle Neutron Scattering (SANS) examines the order of particles of sizes 1-100nm in solution.[115] Fullerides have an effective diameter[9] of ~10 Å, and if they are dissolved monomerically are at the lower limit of this length scale. It was therefore decided that SANS would be the best way to investigate the inter-fulleride structure of the solution. The final part of this chapter presents the results from SANS studies of metal-ammonia-fulleride solutions

5.2 Wide Angle Diffraction Studies of Metal-Ammonia-Fulleride Solutions

5.2.1 Introduction

A single diffraction measurement on a metal-ammonia-fulleride solution, after correction, yields a total structure factor, $F(Q)$. This is a weighted sum of ten different partial structure factors arising from the ten partial pair correlation

functions, from the four different atomic species. The $F(Q)$ can be broken up using the technique of hydrogen/deuterium second order isotopic substitution (see section 2.9). From the resulting functions the structure can be probed further still using the technique of Empirical Potential Structural Refinement (EPSR) analysis, which permits a 3D analysis and a complete extraction of the individual pair distribution functions (see Chapter 4).[130,131] This chapter draws conclusions before and after EPSR analysis, in order to validate the use of this analysis technique. The experiment presented in this chapter measures the solvation structure of a large ion in a polar solvent and is a unique measurement in this regard.

The solution under study was chosen to be of composition, $C_{60}K_5(NH_3)_{250}$. The ratio of potassium to C_{60} ensured a maximum charging of the fullerene to C_{60}^{5-}, which intuitively yields the most developed solvent structure. The C-N and C-H correlations would be concentrated enough to be well represented in the diffraction data, but also at a concentration that previous experiments suggested would be homogenous.[140]

SANDALS has an advertised Q-range from $0.1Å^{-1}$ to $50Å^{-1}$, and this experiment aimed to access the low Q-region for evidence of inter-fulleride correlations. Unfortunately, at the time of experiment, there were problems with the detector stability in the low angle banks rendering the information from these banks unusable. The measurements therefore had a low-Q limit of $0.5Å^{-1}$.

5.2.2 Experimental Details

Three isotopically different samples were measured: (1) $C_{60}K_5(NH_3)_{250}$, (2) $C_{60}K_5(ND_3)_{250}$, and a 50:50 mixture of (1) and (2). The solution was prepared *in situ* by condensing a known amount of anhydrous ammonia gas onto pre-weighed potassium metal and C_{60} fullerite powder under vacuum conditions at 230K, as described in Chapter 3. Typical counting times were ~10 hours for each of the three samples. Before merging the individual (detector averaged), two hour long

data runs, the runs themselves were investigated as a function of time, to ensure the solutes were not still dissolving. Established routines were then employed to correct the raw data for background scattering, absorption, multiple scattering, inelastic scattering, and normalisation using the ATLAS suite of programs[113] (see Chapter 3).

5.2.3 Total Structure Factors and Pair Distribution Functions

The total normalised structure factors for the three samples, $C_{60}K_5(NH_3)_{250}$, $C_{60}K_5(ND_3)_{250}$ and $C_{60}K_5(ND_3{:}NH_3)_{125:125}$ are shown in Figure 5.1. The Q-range was from 0.5 to 50Å^{-1}. The functions are plotted to 20Å^{-1} to see features more clearly. The number density used throughout the analysis of this experiment, as well as in the EPSR analysis was taken from an equilibrated (N, p, T) Monte Carlo simulation whose volume had been allowed to vary (see Chapter 6). A simulation containing 4 C_{60}^{5-}, 20K^+ and 1000NH_3 was set up with an initial density of 1.4 that of ammonia. This density was estimated from absorption measurements via the incident and transmission monitors on SANDALS. The simulation was then allowed to equilibrate until the fluctuations in volume were very small and a density of 0.9g/cm^3 established. This is equivalent to a number density of 0.11Å^{-3}. The program *Monte*, used for the simulations, establishes the density of water to an accuracy of 1%.[128]

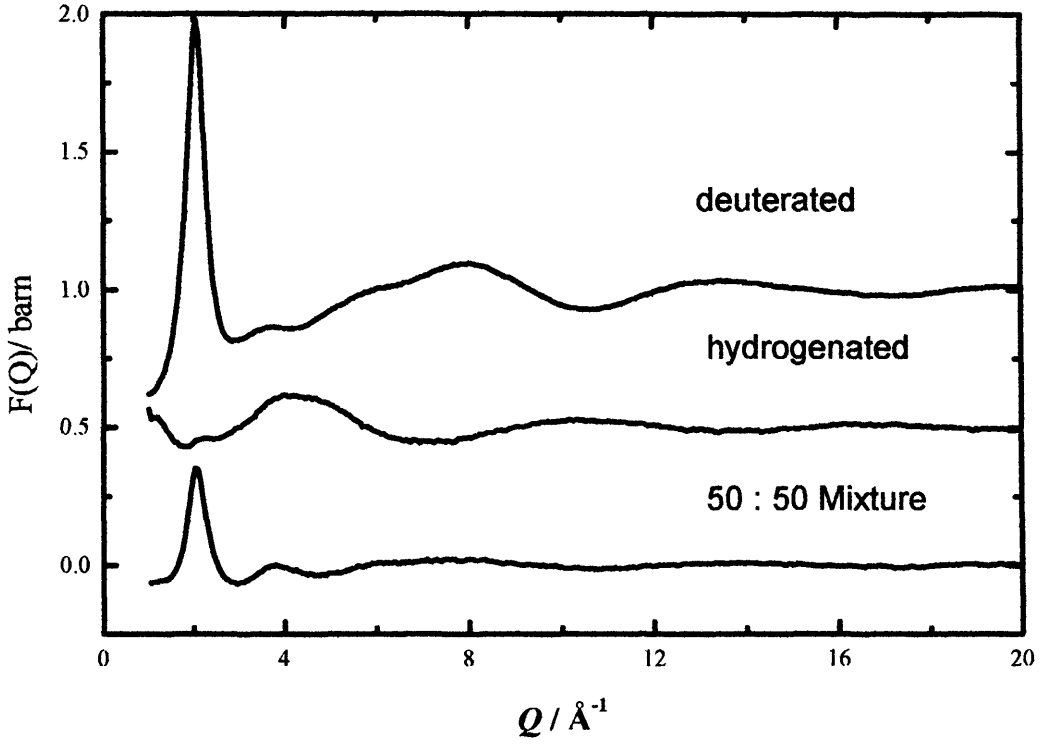

Figure 5.1: Total structure factors for the solutions, (1) $K_5C_{60}(NH_3)_{250}$ $C_{60}K_5(NH_3)_{250}$, (2) $C_{60}K_5(ND_3)_{250}$, and a 50:50 mixture of (1) and (2).

From the functions in Figure 5.1, the second order isotopic substitution was performed (see section 2.9). This yields the composite partial structure factors (CPSFs), $S_{HH}(Q)$, $S_{XH}(Q)$ and $S_{XX}(Q)$ (where H refers to the hydrogen and X to any non substituted atom), which are plotted in Figure 5.2 (top). Fourier transformation of these give the real space, composite partial pair correlation functions, $g_{HH}(r)$, $g_{XH}(r)$ and $g_{XX}(r)$, shown in the same figure (bottom). The Fourier transform was carried out via a minimum noise method in order to eliminate truncation effects and noise within the data. This method finds the smoothest possible real-space distribution function that remains consistent with the reciprocal space data.[141] Although some of the spikier features expected from the C_{60} intramolecular correlations might be compromised (i.e. 'smoothed' out), this method ensures that there are no unphysical features in the data due to truncation effects of the Fourier transform (which is finite). Consistency checks were performed by back transformation of the real space functions, and then

comparing with the data. Figure 5.2 plots this back-transform along with the error bars from the experimental data. The neutron weighting coefficients: the individual percentage contributions of the different pair correlation functions to the CPSFs, $S_{XH}(Q)$ and $S_{XX}(Q)$, are recorded in Table 5.1. The ammonia correlations dominate the CPSFs, the carbon contributions are significantly represented and the potassium contributions are very small.

X-X Correlation	**Coefficient**	**X-H correlation**	**Coefficient**
N-N	0.7203	N-H	0.8487
N-K	0.0113	K-H	0.0067
N-C	0.2455	C-H	0.1446
C-C	0.0209		
K-C	0.0019		
K-K	4.429E-005		

Table 5.1: Neutron weighting coefficients for the partial structure factors, $S_{XH}(Q)$ and $S_{XX}(Q)$.

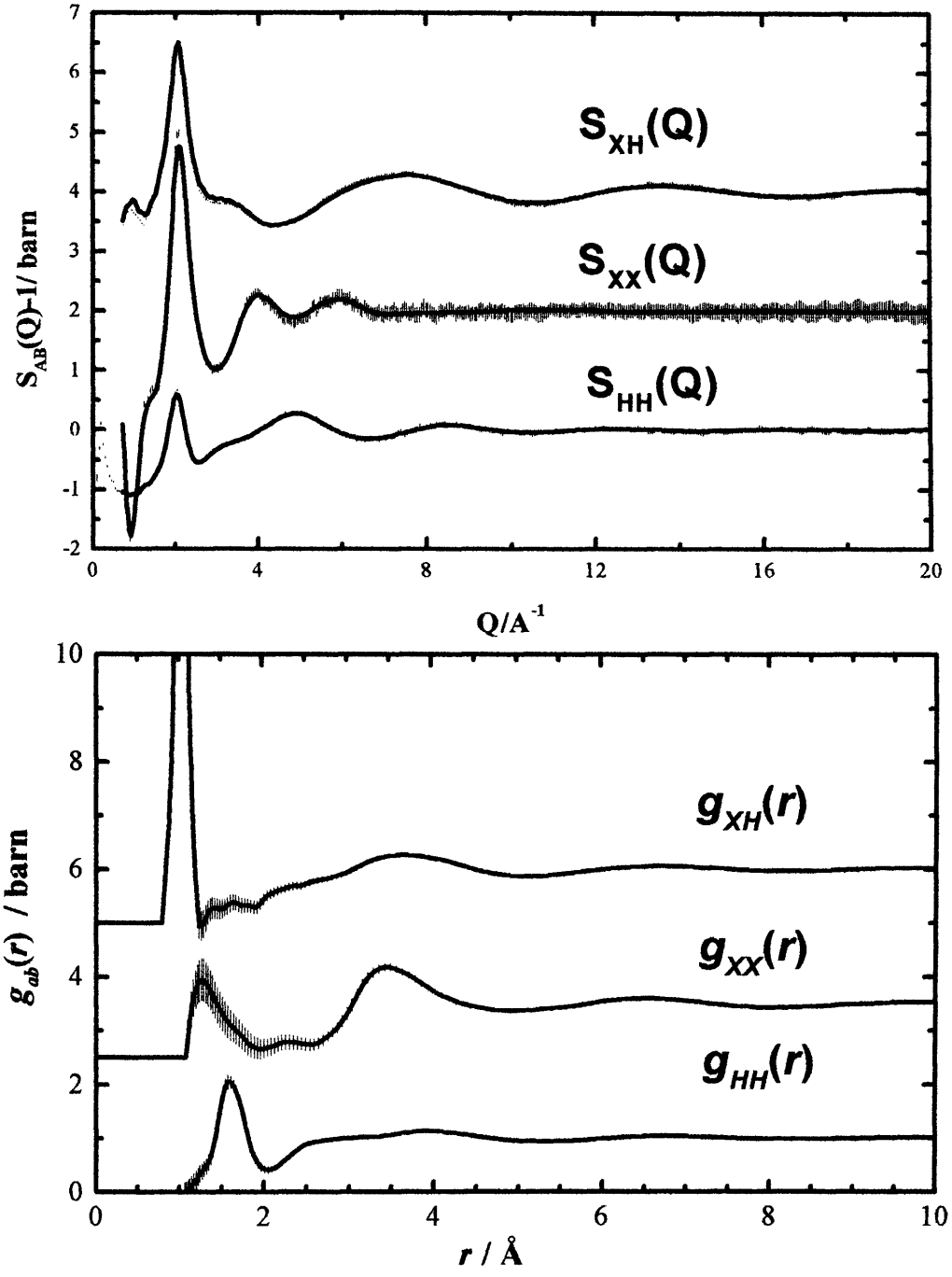

Figure 5.2: Composite Partial Structure Factors (CPSF) (top): $S_{HH}(Q)$, $S_{XH}(Q)$ and $S_{XX}(Q)$. Here the 'back transform' from the real space partial distribution functions is plotted with the experimental error bars. The real space partial distribution functions $g_{HH}(r)$, $g_{XH}(r)$ and $g_{XX}(r)$ are also shown (bottom).

5.2.4 Results and Discussion I

The real space data reveal the expected intramolecular correlations from the fulleride visible in the $g_{XX}(r)$ at ~1.4Å. The intramolecular structure of the ammonia solvent molecules can be seen at ~1.6Å and ~1Å, in the $g_{III}(r)$ and $g_{XH}(r)$ respectively. This is the first time C_{60} has been 'seen' in solution by diffraction. Only the most abundant, shorter bond lengths in the C_{60} anion are present. This is because of the method used to Fourier transform the data.

The CPSFs show some unusual intermediate range features, in particular a small pre-peak before the principal peak at ~0.9Å^{-1} in the $S_{XH}(Q)$, and a shoulder on the principle peak at ~1.1Å^{-1} in the $S_{XX}(Q)$. To shed light on the origin of these features, an identical experiment on pure ammonia was undertaken. The three CPSFs resulting from the pure ammonia experiment completely describe the solution: $S_{XH}(Q)$ represents only N-H correlations, and $S_{XX}(Q)$ just N-N correlations. These results are plotted together with the results on the fulleride solution in Figure 5.3. The error bars from the pure ammonia data have been removed in order to see the features more clearly.

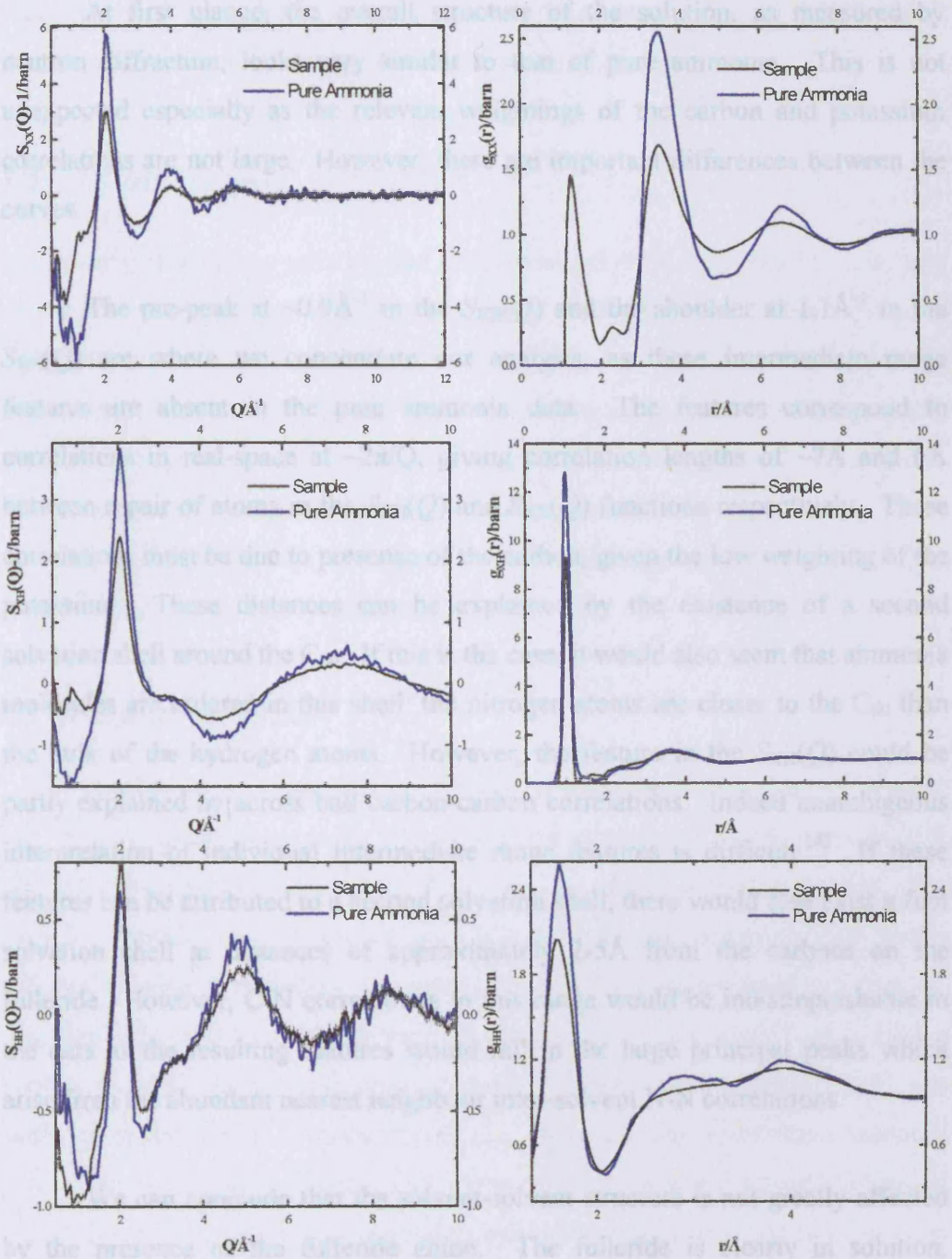

Figure 5.3: A comparison of the solution data, composition $K_5C_{60}(NH_3)_{250}$, (black) with pure ammonia (blue). The CPSFs, $S_{HH}(Q)$, $S_{XH}(Q)$ and $S_{XX}(Q)$, are plotted on the left, their real space $g(r)$ transforms on the right.

At first glance, the overall structure of the solution, as measured by neutron diffraction, looks very similar to that of pure ammonia. This is not unexpected especially as the relevant weightings of the carbon and potassium correlations are not large. However, there are important differences between the curves.

The pre-peak at ~0.9Å^{-1} in the $S_{XH}(Q)$ and the shoulder at 1.1Å^{-1} in the $S_{XX}(Q)$ are where we concentrate our analysis, as these intermediate range features are absent in the pure ammonia data. The features correspond to correlations in real-space at ~2π/Q, giving correlation lengths of ~7Å and 6Å between a pair of atoms in the $S_{XH}(Q)$ and $S_{XX}(Q)$ functions respectively. These correlations must be due to presence of the carbon, given the low weighting of the potassium. These distances can be explained by the existence of a second solvation shell around the C_{60}. If this is the case, it would also seem that ammonia molecules are ordered in this shell: the nitrogen atoms are closer to the C_{60} than the bulk of the hydrogen atoms. However, the feature in the $S_{XX}(Q)$ could be partly explained by across ball carbon-carbon correlations. Indeed unambiguous interpretation of individual intermediate range features is difficult.[142] If these features can be attributed to a second solvation shell, there would also exist a first solvation shell at distances of approximately 2-5Å from the carbons on the fulleride. However, C-N correlations in this range would be indistinguishable in the data as the resulting features would fall in the large principal peaks which arise from the abundant nearest neighbour inter-solvent N-N correlations.

We can conclude that the solvent-solvent structure is not greatly affected by the presence of the fulleride anion. The fulleride is clearly in solution, confirmed by the intramolecular correlations in the $g_{XX}(r)$ at the correct distances. Importantly, the intermediate range influence of the fulleride is also visible in the data giving rise to distinct features which perhaps can be attributed to a second solvation shell around the fulleride. However, the analysis is limited and unambiguous interpretation of the data is complicated by the mixture of correlations over the relevant intermolecular length scales. In order to establish

more information from the data, the recently developed technique of Empirical Potential Structural Refinement (EPSR) has been employed.

5.2.5 EPSR Analysis

An investigation of the experimental data averaged over all directions, can only reveal so much information about the system. A 3-dimensional investigation is possible using the EPSR technique (see Chapter 4). In brief, this procedure iteratively refines the inter-atomic forces of a molecular ensemble of the solution, until the average structure reproduces the diffraction data. The technique allows the extraction of 2- and 3-dimensional information from the experiments. More importantly, EPSR enables us to use the known, fixed geometry of the C_{60}^{5-} as a probe of the local environment around it.

5.2.5.1 Simulation Details

EPSR simulations were carried out on the data using the CPSFs, $S_{HH}(Q)$, $S_{XH}(Q)$ and $S_{XX}(Q)$ for the refinement. The ensemble consists of a cubic box of side ~42.6Å containing 2000 ammonias, 8 C_{60}^{5-} anions and 40 potassium cations. The 'seed' potentials are classical Lennard-Jones pairwise potentials and (some effective) Coulomb potentials, the parameters of which are recorded in Table 5.2. The ammonia molecule is the 4-site OPLS model,[143,144] which has been used in a similar study on lithium-ammonia solutions.[85] A reference 'dummy atom' was included at the centre of mass of the C_{60}^{5-} to allow the distribution functions centred on the ion to be plotted. The carbon potential used is discussed in Section 6.2.1. To represent the charge on the fulleride, the charge was evenly distributed across the fixed carbon atoms, i.e. -5/60e on each carbon atom. This assumption of the equivalent electronic nature of the atoms in the C_{60}^{5-} anion, in these solutions, was later confirmed by a single peak in its ^{13}C NMR spectrum (see Chapter 7).

Atom Type	σ (Å)	ε (kcal mol^{-1})	Q (e)
N[143]	3.42	0.170	-1.02
H[143]	0	0	0.340
K[145]	2.58	1.89	1.00
C[146]	3.80	0.0659	-0.0833

Table 5.2: Potentials used in the EPSR analysis of the form $V_{ij}(r_{ij}) = \frac{q_i q_j}{r_{ij}} + 4\varepsilon_{\alpha\beta}\left[\left(\frac{\sigma_{\alpha\beta}}{r_{ij}}\right)^{12} - \left(\frac{\sigma_{\alpha\beta}}{r_{ij}}\right)^{6}\right]$.

5.2.6 Results and Discussion II, EPSR

Typical fits of the EPSR ensemble to the CPSFs are shown in Figure 5.4 and a molecular graphics snapshot of the resulting ensemble is shown in Figure 5.5.

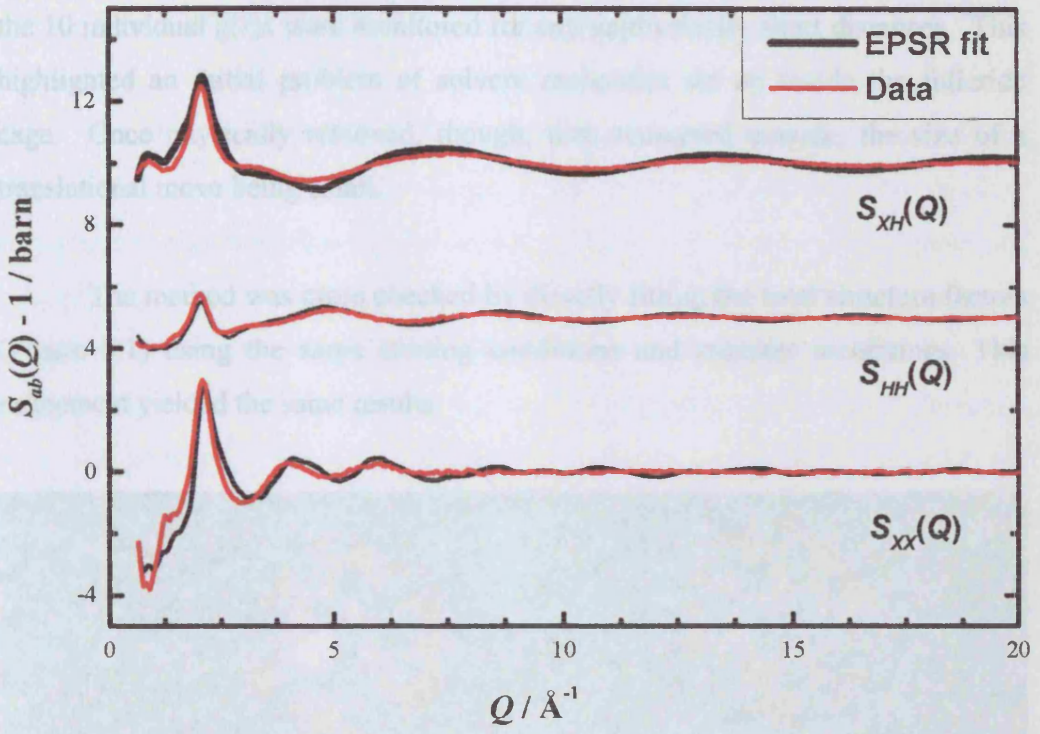

Figure 5.4: EPSR fits (red) to the measured CPSFs (black) obtained from the second order difference for the solution, composition $K_5C_{60}(NH_3)_{250}$.

The ESPR fits closely represent the data but there are some subtle differences. These are found at low-Q in the $S_{XX}(Q)$, in particular, and can be explained by an imperfect removal of inelastic scattering.[133,147] Otherwise, all the salient features in the data are very well reproduced. Care must be taken to ensure that the simulation is actually accessing all areas of phase space and that the resulting physical model is realistic. Whilst the extent to which the EPSR technique adds and takes away from the data is still debated, care must also be taken in its interpretation. Tests on the technique so far indicate that refining the initial 'seed' potentials to recreate the diffraction data, yields ensembles that recreate the topology of the local order.[131]

EPSR produces an output giving nearest molecule approaches. This and the 10 individual $g(r)$s were monitored for any unphysically short distances. This highlighted an initial problem of solvent molecules set up inside the fulleride cage. Once physically removed, though, they remained outside, the size of a translational move being small.

The method was cross checked by directly fitting the total structure factors (Figure 5.1) using the same starting conditions and relevant weightings. This refinement yielded the same results.

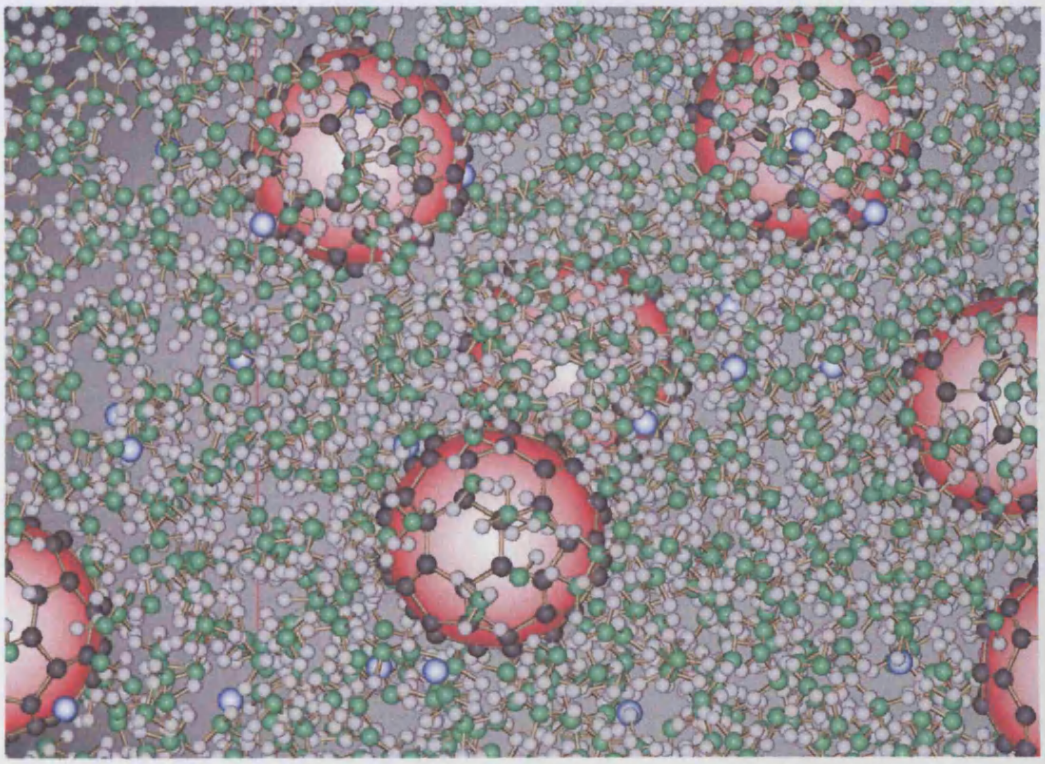

Figure 5.5: Molecular Graphics Snapshot of the EPSR ensemble fit to the diffraction data. Key: fulleride – red, carbon – black, potassium ion – blue, hydrogen – white, nitrogen – green.

From the resulting ensemble, the individual site-site radial distribution functions (rdfs), $g_{\alpha\beta}(r)$, for the relative density of atoms of type β as a function of their distance, r, from one of type α, are extracted. The 10 rdfs are shown in

Figure 5.6. Note that unlike the partial distribution functions presented in Figure 5.2, the intramolecular peaks are not included here.

Where there is a distinct peak indicating a specific organisation of one atom around another (usually limited to nearest neighbours in liquids), coordination numbers have been recorded in Table 5.3. These were determined by counting, after each EPSR iteration, over a specific range corresponding to minima in the respective $g(r)$. The coordination numbers given are then averages over a number of iterations, and their errors correspond to the r.m.s. deviation from this average. The more 'defined' a feature (i.e. sharper the peak), the smaller the percentage error on the coordination number. Some of the errors on these numbers appear large, but this is expected for the dynamic nature of a liquid's structure.

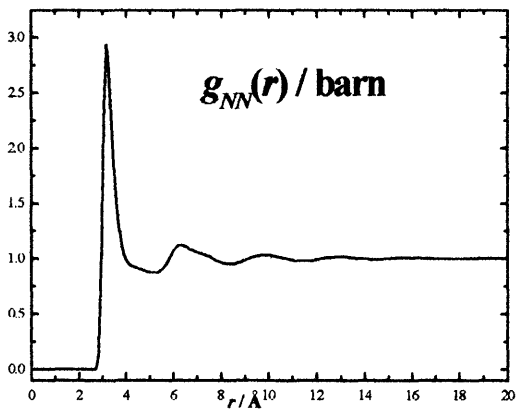
$g_{NN}(r)$ / barn
r / Å

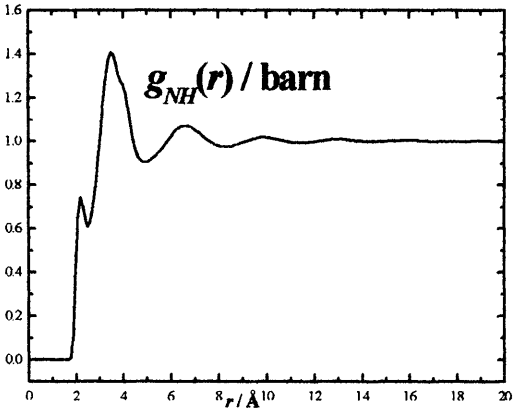
$g_{NH}(r)$ / barn
r / Å

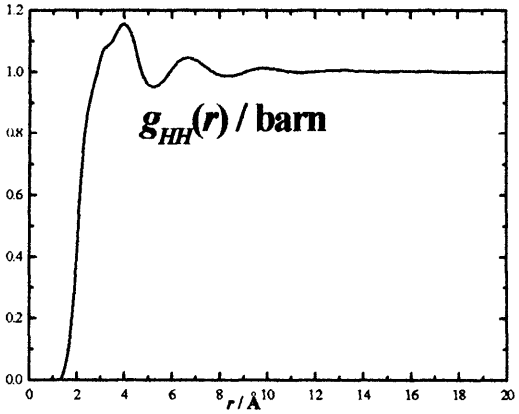
$g_{HH}(r)$ / barn
r / Å

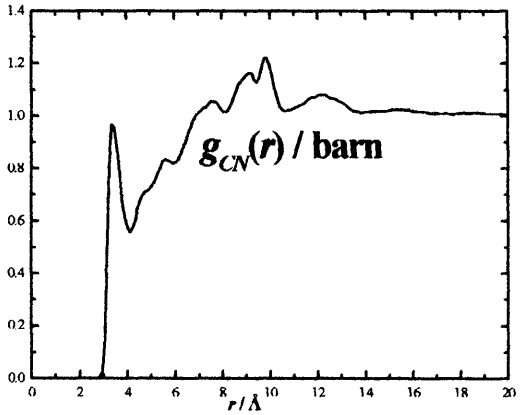
$g_{CN}(r)$ / barn
r / Å

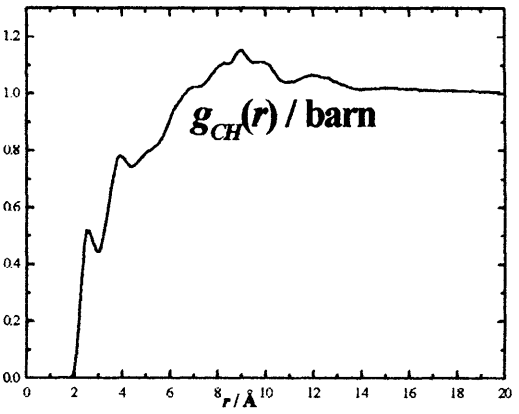
$g_{CH}(r)$ / barn
r / Å

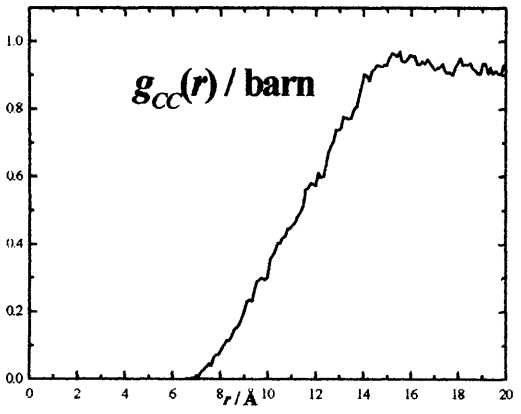
$g_{CC}(r)$ / barn
r / Å

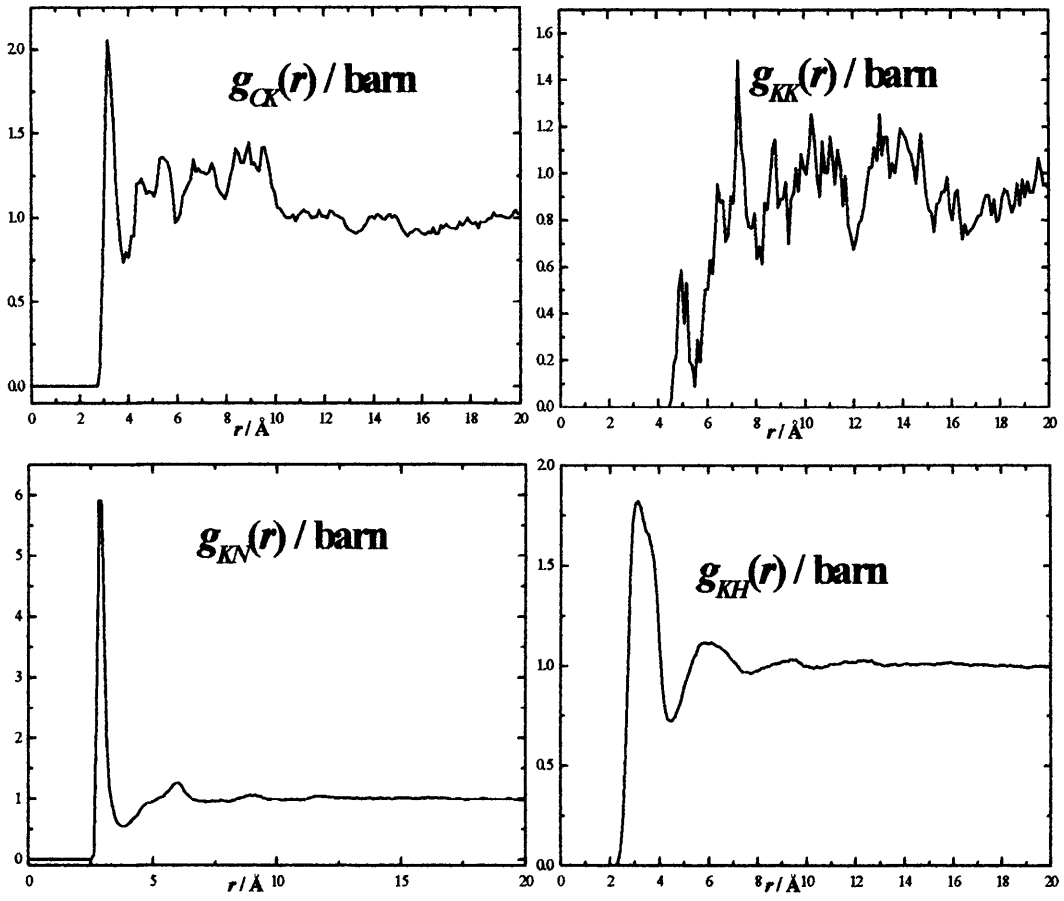

Figure 5.6: Individual site site radial distribution factors, $g_{\alpha\beta}(r)$, for the 10 pairs of atom types in the solution.

Correlation	R_{min}(Å)	R_{max}(Å)	Coordination Number
NN	2.6	5.2	14.4±1.5
NH	1.8	2.5	1.7±0.9
CN	2.9	4.1	3.2±0.8
CH	1.9	2.9	2.3±0.8
CH	2.9	4.4	13.2±2.3
CK	2.6	3.9	0.1±0.3
KN	2.5	3.6	6.6±1.1
KH	2.2	4.5	30.1±3.5

Table 5.3: Coordination numbers for individual features in the $g(r)$s.

The neutron weightings recorded in Table 5.1 must be considered whilst examining the individual partials: the lower the weighting, the more EPSR becomes weighted more towards the simulation than the data.

5.2.6.1 Solvent-Solvent Structure

The effect of the fulleride anion on the structure of the solvent is examined by comparing the relevant pair distribution functions with the (unEPSR'd) pure ammonia data. The $g_{III}(r)$ is compared in Figure 5.3, a comparison of the $g_{XII}(r)$ and $g_{NN}(r)$ is shown in Figure 5.7.

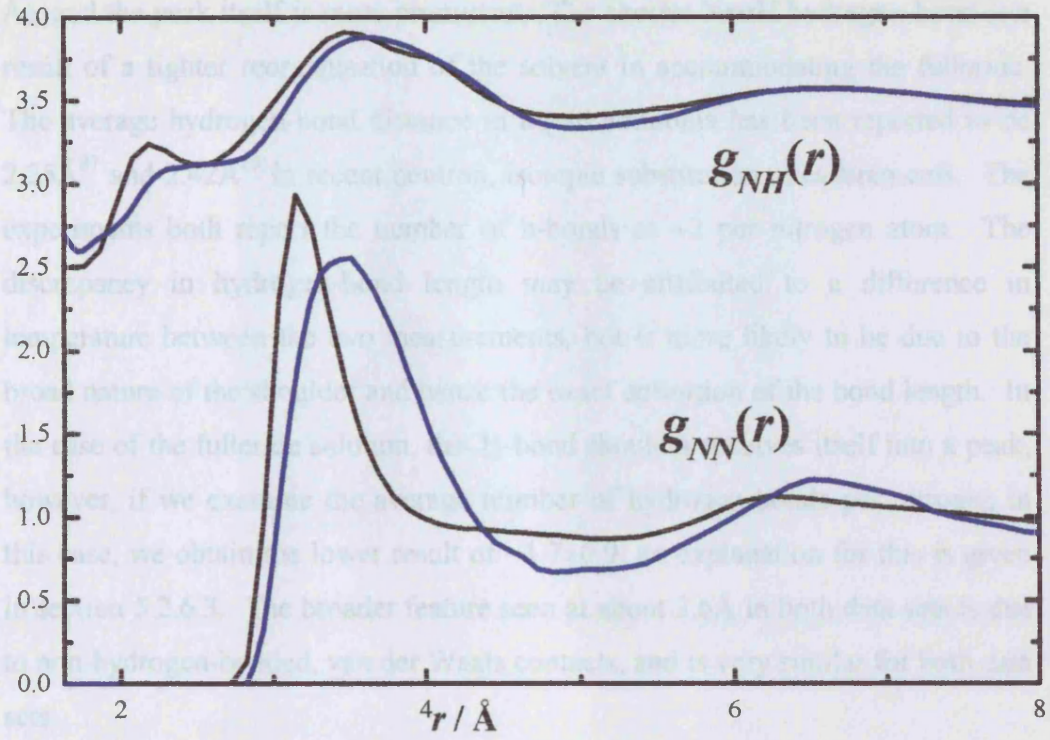

Figure 5.7: A comparison of the partial distribution functions, $g_{NH}(r)$ and $g_{NN}(r)$ of the solution data (black) and pure ammonia data (blue).

Firstly, the $g_{HH}(r)$ is considered. The shape of the two functions, for the solution and pure ammonia data, is very similar though the broad peaks in the ammonia data at about 2.9Å and 3.9Å are slightly less intense. The correlation visible at 2.9Å is equivalent to the distance between two adjacent hydrogen-bonded molecules.[87] This suggests a slight reduction in the number of hydrogen-bonds between neighbouring ammonia molecules.

Most inter-solvent hydrogen-bonding information can be found in the $g_{NH}(r)$. Nearest neighbour hydrogen-bonding is visible in both the ammonia and solution data and manifests itself as a shoulder/pre-peak at distance of ~2.4Å. There is a noticeable difference between this hydrogen-bonding feature in the two functions: the average hydrogen-bond distance is less for the solution data (~2.2

Å), and the peak itself is more prominent. The shorter N•••H hydrogen-bond is a result of a tighter reorganisation of the solvent in accommodating the fulleride. The average hydrogen-bond distance in liquid ammonia has been reported to be 2.25Å[87] and 2.42Å[85] in recent neutron, isotopic substitution, measurements. The experiments both report the number of h-bonds as ~2 per nitrogen atom. The discrepancy in hydrogen-bond length may be attributed to a difference in temperature between the two measurements, but is more likely to be due to the broad nature of the shoulder and hence the exact definition of the bond length. In the case of the fulleride solution, this H-bond shoulder resolves itself into a peak, however, if we examine the average number of hydrogen-bonds per nitrogen in this case, we obtain the lower result of ~1.7±0.9, an explanation for this is given in section 5.2.6.3. The broader feature seen at about 3.6Å in both data sets is due to non-hydrogen-bonded, van der Waals contacts, and is very similar for both data sets.

The N-N function shows a movement of the position of the principal peak to low-Q as the fulleride is introduced from ~3.46Å in the pure ammonia to ~3.18Å in solution. This is indicative of an increase in density. The shift is attributed to a 'tighter binding' between ammonia molecules in the solvent, due to the accommodation of the fullerides. Further evidence for this 'tighter binding' is the sharpening of the principal peak in the solution data compared with the solvent. The slight asymmetry of the pure ammonia principal N-N peak becomes more exaggerated as the fulleride is introduced. This indicates an enhancement of the immediate nearest neighbour close packing in the solvent. Integration out to 5.2Å, yields a coordination number of ~14 for the solution data which is the same value found for pure ammonia.[87]

The 3D ammonia-ammonia average structure is shown in Figure 5.8. This is calculated by holding an ammonia molecule in fixed orientation and calculating the 20% most likely angular positions of the approach of another ammonia molecule, in any orientation, averaged over the entire system for the distance equivalent to the nearest neighbour first shell (i.e. to 5.2Å).

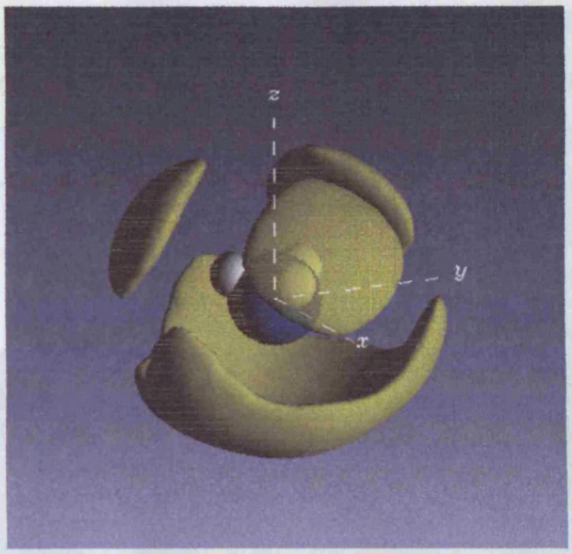

Figure 5.8: 3-D average structure of hydrogen-bonding between ammonia molecules in the solution, $K_5C_{60}(NH_3)_{250}$. The yellow region shows the most likely angular positions that an ammonia molecule, in any orientation, can be found in with respect to a fixed ammonia molecule. This figure plots the 20% most likely positions in the region from 0-5.2 Å equivalent to the nearest ammonia-ammonia distances.

The direction of the hydrogen-bonding can be seen from the acceptor lobes which are found above the hydrogen atoms in the ammonia at the origin. This is very similar to the structure developed in dilute metal-ammonia solutions.[135] In these solutions the number of hydrogen-bonds per nitrogen atom is slightly reduced due to the coordination of the solvent to the cationic species (see section 5.2.6.3).

5.2.6.2 Fulleride Solvation Structure

The $g_{CN}(r)$ shown in Figure 5.6, has a peak at 3.3Å. The $g_{CH}(r)$ function has a similar peak at 2.6Å and again at 2.9Å. These features are attributed to an intense immediate ordering of the solvent around the fulleride: the three features at these distances are suggestive of ammonia molecules coordinated to the C_{60} anion. For more insight, the spatial density function of the system for the distribution of

ammonias around a C_{60} anion's centre of mass is investigated. Figure 5.9 shows a 2-dimensional projection of the average relative density of ammonia molecules around a reference fulleride anion, averaged over the entire system, effectively a 2D $g(r)$. The relevant coordination numbers for the solvation shells are presented in Table 5.4.

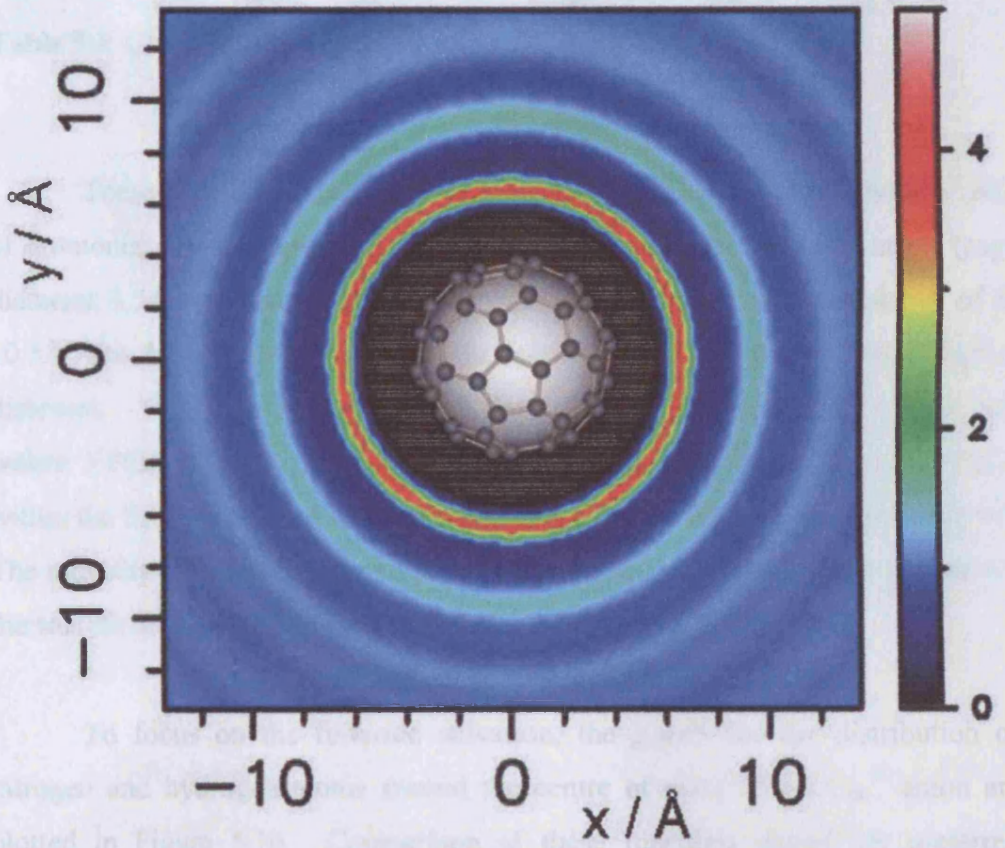

Figure 5.9: 2-dimensional projection of the NH_3-C_{60}^{5-} solvent structure in the solution. This figure shows the ensemble average relative density of ammonia molecules around a reference fulleride located at the origin.

Correlation	R_{min}(Å)	R_{max}(Å)	Coordination Number
C_{60} N	0	7.5	44.6±1.9
C_{60} N	8	10.5	79.6±3.5
C_{60} H	0	6.2	39.7±2.2
C_{60} H	6.2	7.6	96.2±4.6

Table 5.4: Coordination numbers for the ammonia solvation of C_{60}^{5-}.

These data immediately reveal a very dense spherical first solvation shell of ammonia at a distance of 5.5-7.5Å from the centre of the C_{60}^{5-} anion (cage diameter 3.54Å). Beyond this, the second solvation shell is at a distance of 8-10.5Å with the anion's influence on the solvent matrix still discernable at further distances. This is in agreement with the initial conclusions drawn on the data before EPSR analysis. The average fulleride-nitrogen coordination numbers within the first and second solvation shells are ~45 and 80 ammonias respectively. The intensity of these shells is surprisingly large and the question now is, how are the solvent molecules oriented in these shells?

To focus on the fulleride solvation, the $g_{\alpha\beta}(r)$s for the distribution of nitrogen and hydrogen atoms around the centre of mass of the C_{60}^{5-} anion are plotted in Figure 5.10. Comparison of these functions shows the preferred orientation of the ammonia molecules in the first solvation shell. The relative intensities of the first two peaks (at ~5.5 and 7.1Å), see Table 5.4, together with the position of the nitrogen peak, indicate that the molecules in this first shell adopt a position with, on average, approximately one hydrogen atom pointing to the centre of the C_{60} anion.

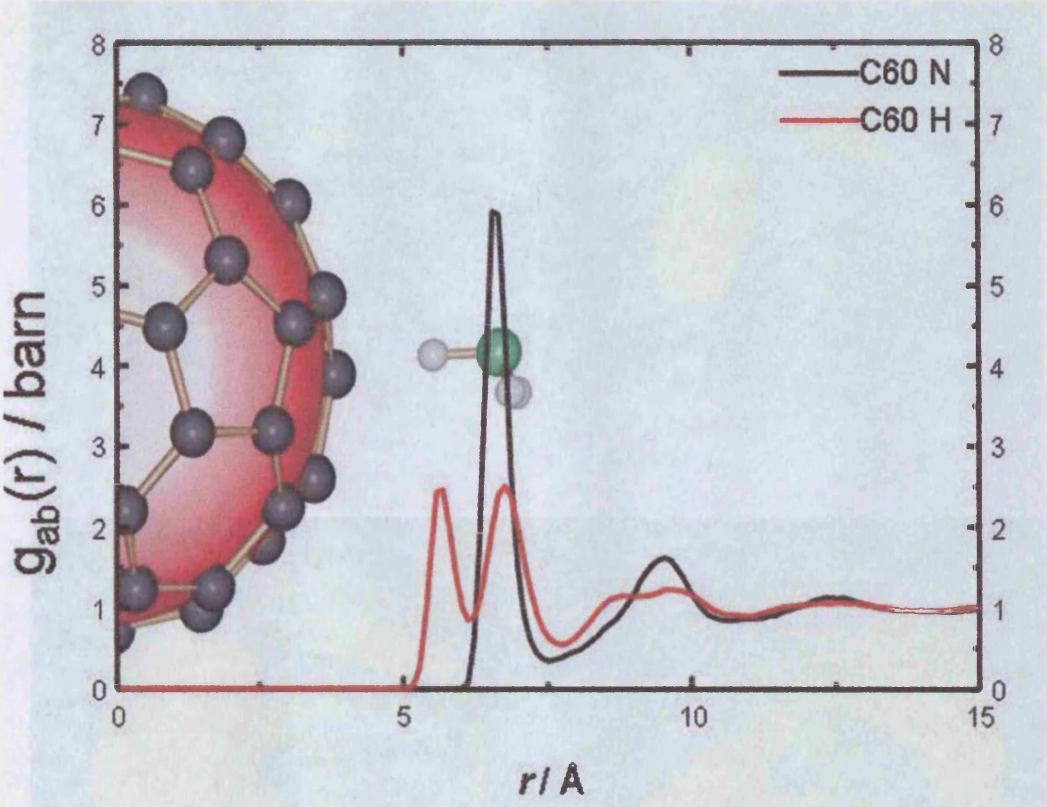

Figure 5.10: Pair distribution function of nitrogen and hydrogen around the centre of mass of a fulleride anion, with molecular graphics to guide the eye.

A 3-dimensional examination of this hydrogen-bonding is shown in Figure 5.11. This was carried out by holding the ammonia molecule in a fixed orientation and plotting the distribution of C_{60}s (CoM) around it averaging over every C_{60} and ammonia in the ensemble. The figure plots the isosurfaces of the 50% and 90% most likely angular positions of a C_{60}^{5-} around a fixed ammonia molecule for distances equivalent to the two solvation shells.

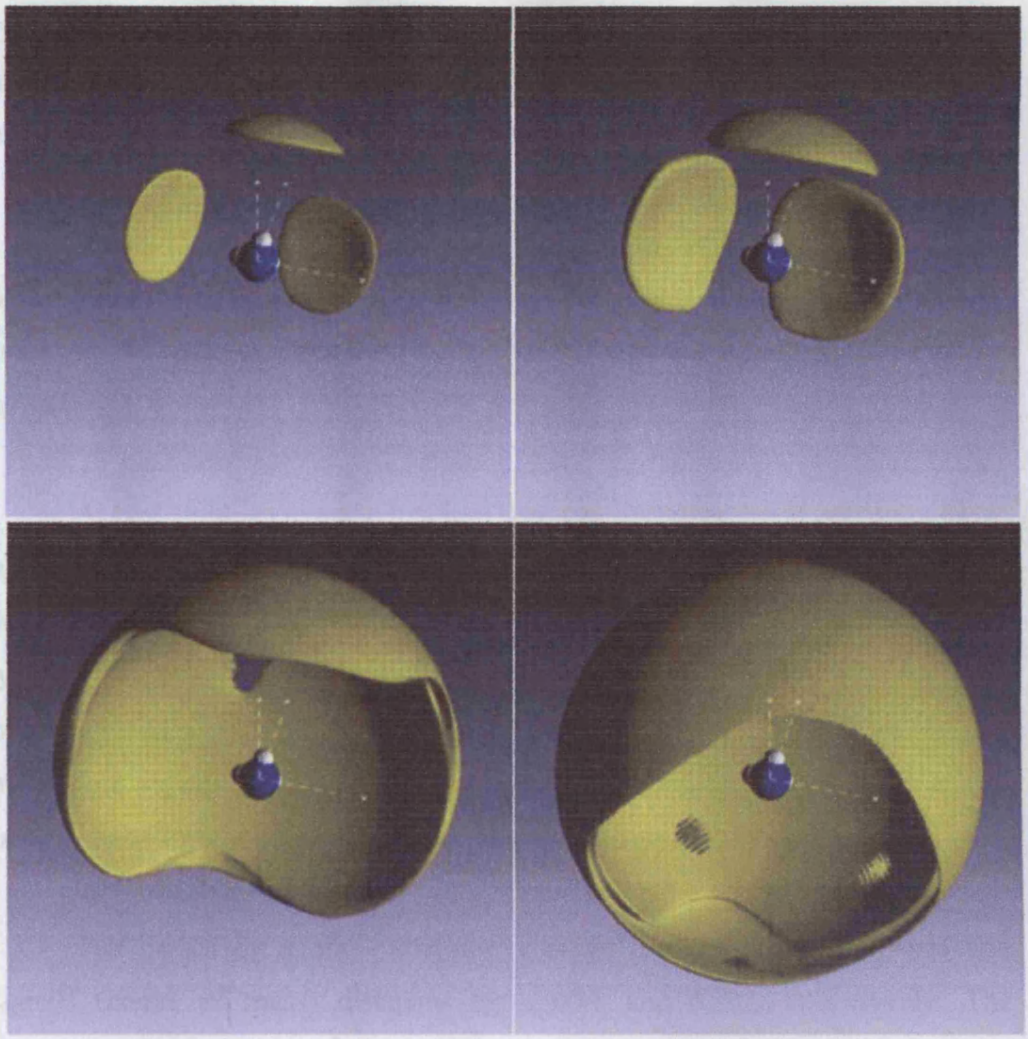

Figure 5.11: 3-dimensional fulleride anion solvation structure. The yellow region shows the most likely angular positions that a C_{60}^{5-} anion can be found in with respect to a fixed ammonia molecule. This is plotted from 0-7.5 Å (top) and 8.8-10.5 Å (bottom) to the centre of the fulleride anion, equivalent to the distances of the two solvation shells. The figure plots the 50% (left) most likely positions and 90% most likely (right).

The results confirm that, within the first solvation shell, the ammonia molecules are aligned with one hydrogen atom pointing towards the centre of the fulleride anion. In the second shell, it can be seen that although this directionality is still present, it is broader and includes molecules in which two or three

hydrogen atoms point towards the centre. However, it shows that the overall dipole moment of the ammonia molecules is the same in the second shell. This is due to hydrogen-bonding to ammonia molecules in the first shell.

The coordination numbers reveal ~45 nitrogen atoms, and hence ammonia molecules, in the first solvation shell. Out of these, there are ~40 hydrogen-bonds to the C_{60}. Therefore ~90% of the ammonias in this shell form hydrogen-bonds to the fulleride.

At first sight, an average just less than one hydrogen-bond per ammonia to the anion in the first shell may seem small, since the anion is highly charged. However, by adopting this orientation the ammonia molecules can then complete hydrogen-bonds within and across the solvation shells. This is why, although roughly half of all the total solvent molecules are involved in the solvation shell, there is no significant change in the average solvent-solvent structure of the fulleride solution from the pure ammonia solvent structure.

The partial $g(r)$s show that the average nearest-neighbour C•••H and C_{60}•••H (centre of mass) distances are 2.60Å and 5.80Å respectively. The fulleride cage radius is 3.54Å suggesting that the ammonia molecules are typically located over the pentagonal and hexagonal rings allowing for a closer approach. There are ~40 hydrogen-bonds per fulleride, which gives ~1.25 bonds per carbon ring. More insight into the organisation can be gained from examination of a molecular graphics snapshot of the solution.

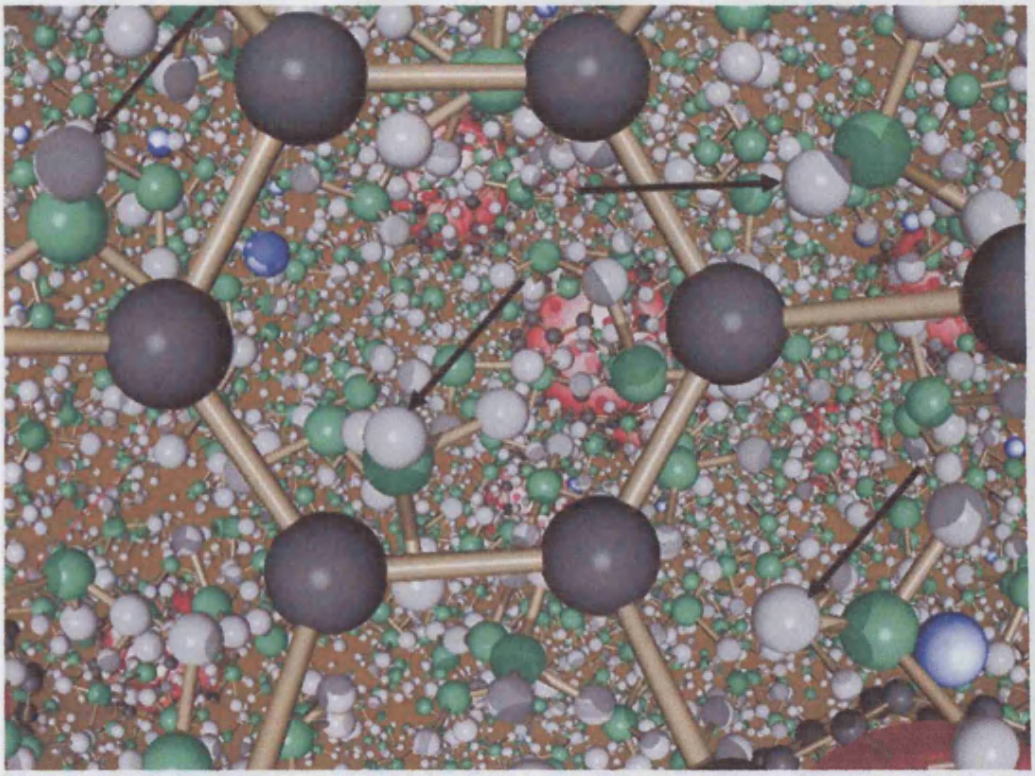

Figure 5.12: Snapshot taken from 'inside' the fulleride. Black arrows point to the hydrogen (white) bonds to the carbon rings.

Figure 5.12, an EPSR ensemble snapshot taken from 'inside' a fulleride, shows that the hydrogen-bonds point towards the 5 and 6 membered rings rather than the actual carbon atoms. This arrangement allows for a closer approach of the ammonia molecules to the fulleride. The unusually short C•••H hydrogen-bond lengths of ~2.6Å are consistent with those observed in solid $(ND_3)_8Na_2C_{60}$ and $(ND_3)_xNaRb_2C_{60}$ (C•••D ~2.55Å to 2.76Å), where the ammonia molecules are shared between fulleride and metal ions.[111]

5.2.6.3 Potassium Solvation

The potassium cation solvation can be investigated by examining the $g_{KN}(r)$ and $g_{KH}(r)$, shown in figure 5.6, and the spherical harmonic plot, shown in Figure

5.13. This diagram shows the most likely orientational position of a potassium cation with respect to an ammonia molecule.

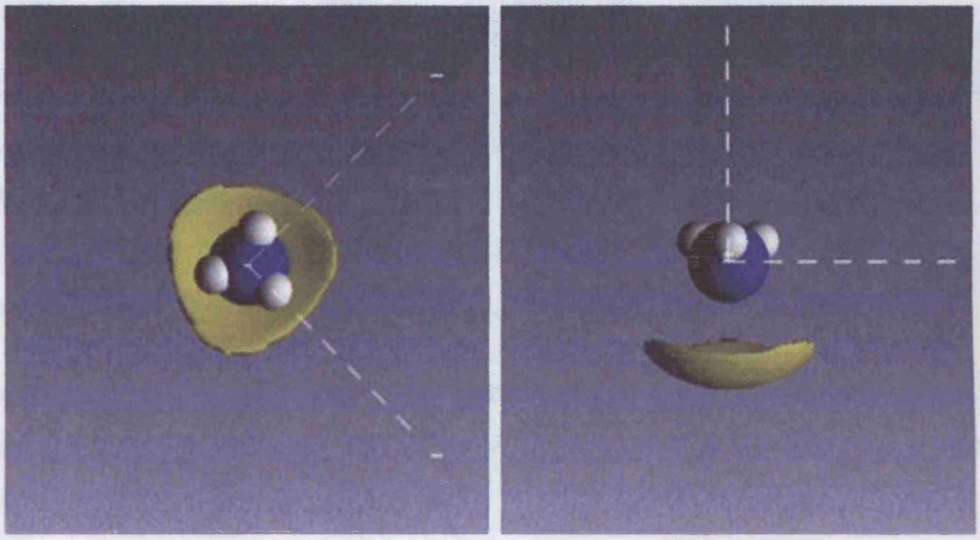

Figure 5.13: Potassium cation solvation by ammonia. The yellow region shows the most likely angular positions that a potassium cation can be found in with respect to a fixed ammonia molecule. The ammonia molecule directs its nitrogen atom towards the cation.

From the coordination numbers shown in Table 5.3, we find that the cations are solvated by ~6.6 ammonia molecules at an average distance of ~2.9Å. The cations are found with the more electronegative nitrogen atom pointing directly towards them. The value of the K-N distance is almost identical to that found in a neutron diffraction experiment of potassium-ammonia solution,[148] and the effect of the fulleride on the solvation of the potassium cation appears minimal.

The potassium solvation also explains the reduced total number of hydrogen-bonds that exist on average in solution, when compared to pure ammonia. There are, on average, 6.6 nitrogen atoms solvating the potassium ions which are therefore not involved in inter-solvent hydrogen-bonding. There are 5

potassium ions per 250 solvent molecules and in the pure solvent there are ~2 hydrogen-bonds per nitrogen atom. This means 5 × 6.6 × 2 = 66 *less* hydrogen-bonds are expected per 250 ammonias. In pure ammonia, ~2 hydrogen-bonds form per nitrogen giving roughly 500 bonds per 250 ammonia molecules. If we subtract from this the 66 bonds unable to form due to cation solvation we obtain ~436 i.e. ~1.74 N-H hydrogen-bonds on average per nitrogen. This is consistent with the value obtained from the analysis.

5.2.6.4 Anion-Cation Correlations

The fulleride is a highly negatively charged anion and it seems likely that cation-anion pairs will form. The partial distribution function for potassium around the centre of a C_{60} is shown in Figure 5.14.

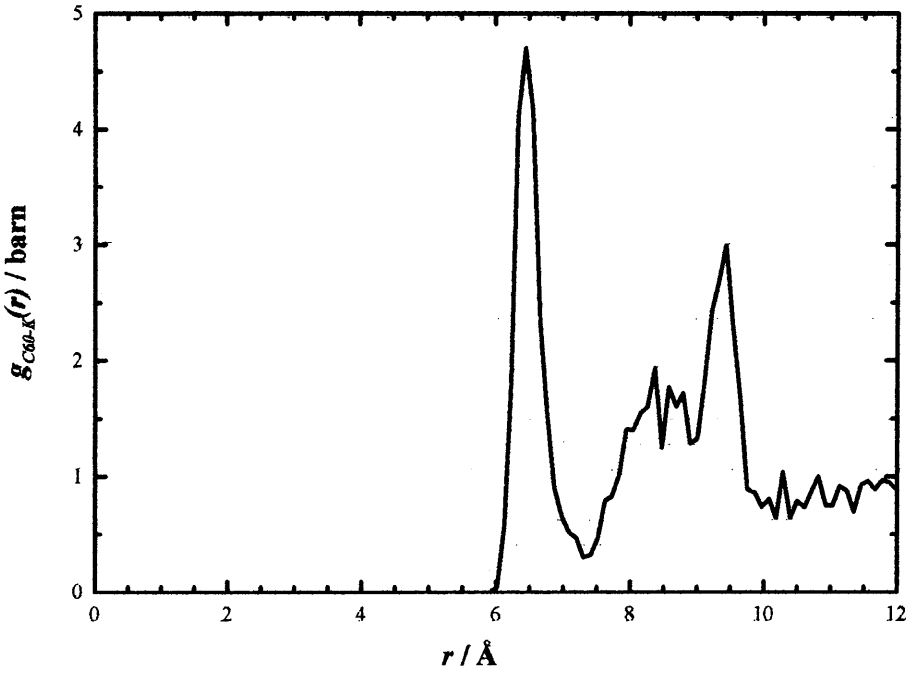

Figure 5.14: Distribution of potassium around C_{60}, $g_{C60\text{-}K}(r)$.

There is a peak in Figure 5.14 representing potassium cations closely coordinated to the C_{60}. The statistics in this function are relatively poor, due to

the relatively low concentration of the ions. The number of cations this peak represents is ~1.7±0.7. Integrating the area beyond this from 7.4-10Å, gives a coordination number of ~0.9±1. These large errors indicate the 'instability' of these peaks. The average distance of the cation to an individual carbon atom is ~3.2Å. The distances involved are not greater than the respective C_{60}-H and C-H distances, but are similar to those found in K_3C_{60}[7] crystals. Although ion pairs do form, the frequency of them occurring is not high, due to the strength of the respective potassium and fulleride solvation by the ammonia molecules.

5.2.6.5 Inter-fulleride Structure

Strong conclusions cannot be drawn about the inter-fulleride correlations from these results, as these would give rise to features visible only at lower values of Q than those measured here. To obtain accurate data on this, we require a larger box size and/or lower-Q data. However, the strength of the solvent ordering, and the resulting structure of the solvation shells around the C_{60} anions, indicate that inter-fulleride contacts are absent. The solute molecules are therefore dispersed via solvent-separation. If the fulleride has a core radius of 3.54Å and is surrounded by two well defined solvation spheres, then its effective radius in solution is ~10.5 Å.

5.2.7 Conclusions

We conclude that in $C_{60}K_5(NH_3)_{250}$ solutions the C_{60}^{5-} anions are strongly solvated by a shell of ~45 ammonia molecules, located around 6-7Å from the centre of the fulleride. These molecules direct one of their hydrogen atoms towards the centre of the fulleride anion, while retaining axial hydrogen-bonding within the shells. This means that the overall solvent structure is similar to that found in bulk ammonia, despite the high fulleride concentrations. The potassium ions are typically solvated in the same way as in a metal-ammonia solution of the same metal concentration. The picture built up from these results is a solution in which the cations and anions are tightly solvated. This prevents the recombination of the salt and permits high concentrations of monodispersed fullerides.

5.3 Small Angle Neutron Scattering Studies (SANS) of Metal-Ammonia-Fulleride Solutions

SANS is used to examine the shape and distribution of particles in solution.[115] A limited Q-range together with the small angle approximation means that SANS is not an atomistic measurement. An accurate, direct Fourier transform to real space is not possible and SANS data is typically analysed by fitting analytical models. The shape of the SANS pattern gives an indication of the types of particles in solution, e.g. rods, spheres, discs, and hence which model to use. Inputting known parameters permits the extraction of other parameters from the fitted pattern.

SANS techniques examine the distribution of particles in the size range 1-100nm.[115] Most of the systems investigated on SANS instruments are at the large end of this scale; the magnitude of scattering decreases rapidly with decreasing particle size. Fullerides find themselves at the minimum limit of this length scale and the experiment performed here tests this limit. Solutions of C_{60} have been examined, using SANS, on two previous occasions. They were either introduced into solution using a surfactant, which significantly increases the volume of the C_{60}s,[149] or the samples had an extremely large sample path length, made possible by using a solvent with very low incoherent scattering.[150]

As SANS instruments are not optimised to maximise their sensitivity for small signals, it was important to calculate expected patterns before the experiment. In this way, the relevant instrument and experimental parameters could be optimised to maximise the chances of obtaining useful data.

5.3.1 Calculations of SANS Patterns

SANS measures the structure of large 'scattering bodies' in a solvent which is treated as a continuous medium. The corrected SANS pattern can be expressed as:

$$\left(\frac{d\sigma}{d\Omega}\right) = (b_p - b_s)^2 N_p V_p^2 P(Q) S(Q), \qquad 5.1$$

where N_P is the number concentration of the particles and V_P is the volume of one scattering body, $P(Q)$ = form factor of the scattering bodies, $S(Q)$ = structure factor of the scattering bodies (see Section 2.8). b_p and b_s are the scattering densities of the scattering particle/solvent respectively. The scattering length density of a particle/molecule is given by:

$$b = \sum_i bi \frac{DN_A}{M_W} \qquad 5.2$$

where D is the bulk density of the scattering body, M_W is its molecular weight, b_i are the atomic the scattering lengths, and N_A is Avogadro's number.

Equation 5.1 tells us is that the greater the number of fullerides that are in solution, the larger the magnitude of the SANS scattering. The other important factor is the 'contrast term', the difference in scattering length between the sample (fullerides) and the medium (ammonia). The choice of ND_3 or NH_3 is relevant in maximising this term. The presence of hydrogen, however, gives rise to a large incoherent background signal. Whilst deuterated ammonia significantly reduces the complications arising from the inelastic scattering the scattering length difference between deuterium and carbon is very small.

Measuring the SANS pattern and changing the concentration of fullerides in solution should yield a non-changing form factor ($P(Q)$) and a concentration dependent structure factor $S(Q)$. Ideally this would permit the separation of the terms and allow the inter-fulleride structure in solution to be examined.

The calculations were performed for the solution of $Li_5C_{60}(NH_3)_{250}$, which has a volume fraction of ~5%, using the program FISH[151] which is designed for SANS data fitting. The scattering from systems using the two different solvents (NH_3 and ND_3) was investigated, as well as using two $S(Q)$ models: hard

interacting spheres and charged spheres. To calculate the $P(Q)$, a two shell spherical model to represent the fulleride was used. This comprises of a central void and a shell of carbon atoms. A calculation of a three shell model, which included a dense layer of ammonia around it, was also undertaken. The basic form of the $P(Q)$ from spherical scattering bodies, radius R, is shown in equation 5.3. The extension to the three shell model is given in reference [151].

$$P(Q) = \left[\frac{3(Sin(QR_F) - QR_F Cos(QR_F))}{(QR_F)^3} \right]^2 \qquad 5.3$$

Figure 5.15 shows calculations of the scattering from a system of a void surrounded by a 1Å thickness of carbon at a radius of 3-4 Å in both hydrogenated and deuterated ammonia. The $S(Q)$ which modifies the $P(Q)$ is based on a hard shell model and is plotted separately in the same figure.

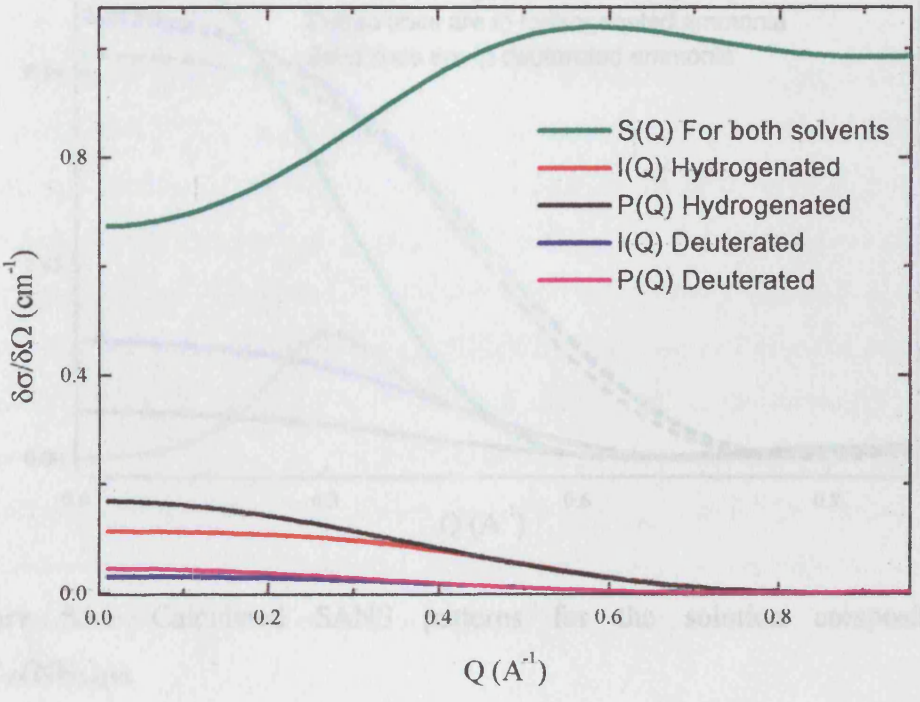

Figure 5.15: Calculated SANS patterns for the solution composition, $Li_5C_{60}(NH_3)_{250}$.

The calculations reveal that the magnitude of the SANS pattern will be very small due to the small size of the form factor. The scattering magnitude from the deuterated sample is significantly less than from the hydrogenated sample. The calculations also indicate that the scattering pattern is to be found at relatively large-Q for a SANS instrument.

Figure 5.16 plots more calculated SANS patterns. In these plots the scattering from three different models of the system are presented. As well as the two shell model presented in Figure 5.15, a model in which the fullerides are represented by a 2Å carbon shell (from 2.5-4.5Å), and by a 1Å shell surrounded by a 120% dense shell of ammonia to 8Å is plotted.

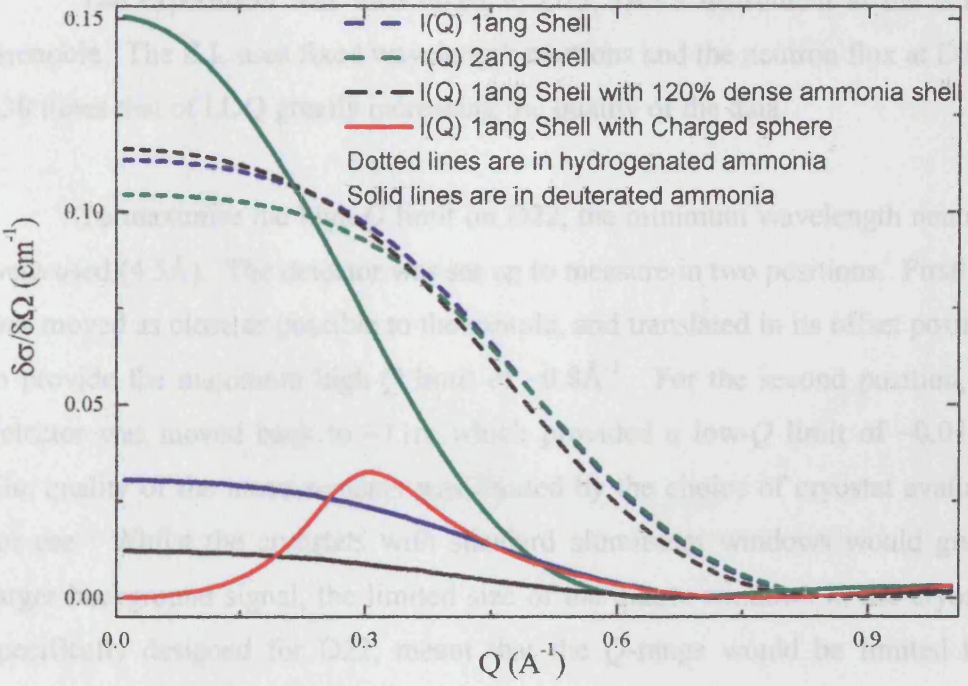

Figure 5.16: Calculated SANS patterns for the solution composition, $Li_5C_{60}(NH_3)_{250}$.

In general the SANS patterns are larger for hydrogenated ammonia. However, this signal would still be swamped by the large incoherent and inelastic scattering associated with the hydrogen, so deuterated ammonia must be used.

Figure 5.16 reveals that the ND_3 solvent is, in fact, more sensitive to a dense ammonia layer surrounding the fulleride.

5.3.2 Experimental

The experiment was initially conducted on the LOQ instrument at ISIS. The scattering from three samples were measured: $Li_5C_{60}((ND)_3)_x$ where x = 250, 350 and 450. The data was measured over a Q-range of ~0.07-1Å^{-1}. The results revealed no small angle scattering but the error bars on the data were large and therefore not conclusive as to whether a SANS pattern would result from further measurements.[152]

The experiment was then taken to D22 SANS instrument at the ILL in Grenoble. The ILL uses fixed wavelength neutrons and the neutron flux at D22 is ~30 times that of LOQ greatly increasing the quality of the data.

To maximise the high-Q limit on D22, the minimum wavelength neutrons were used (4.5Å). The detector was set up to measure in two positions. Firstly, it was moved as close as possible to the sample, and translated in its offset position, to provide the maximum high-Q limit of ~0.8Å^{-1}. For the second position, the detector was moved back to ~11m which provided a low-Q limit of ~0.01Å^{-1}. The quality of the measurements was limited by the choice of cryostat available for use. Whilst the cryostats with standard aluminium windows would give a larger background signal, the limited size of the quartz windows in the cryostat, specifically designed for D22, meant that the Q-range would be limited to a maximum of 0.3Å^{-1}. The aluminium cryostat was chosen to increase the high-Q limit, but the size of the increased background meant that the counting times had to be increased.

The solutions were prepared *in situ*, as described in Chapter 3, by condensing ammonia onto pre-made fulleride salts. Two samples were measured: $C_{60}Li_5(ND_3)_{250}$ and $C_{60}Li_5(ND_3)_{450}$. A sample of $C_{60}K_5(ND_3)_{250}$ was attempted,

however the fulleride salt decomposed in the glovebox. The data was collected for ~1 hour runs alternating between the two detector positions. These were repeated five times at each concentration. To ensure the sample had dissolved, only the last three measurements were included in the analysis. The data was corrected as described in Chapter 3.

5.3.3 Results

The results for the two concentrations are shown in Figure 5.17.

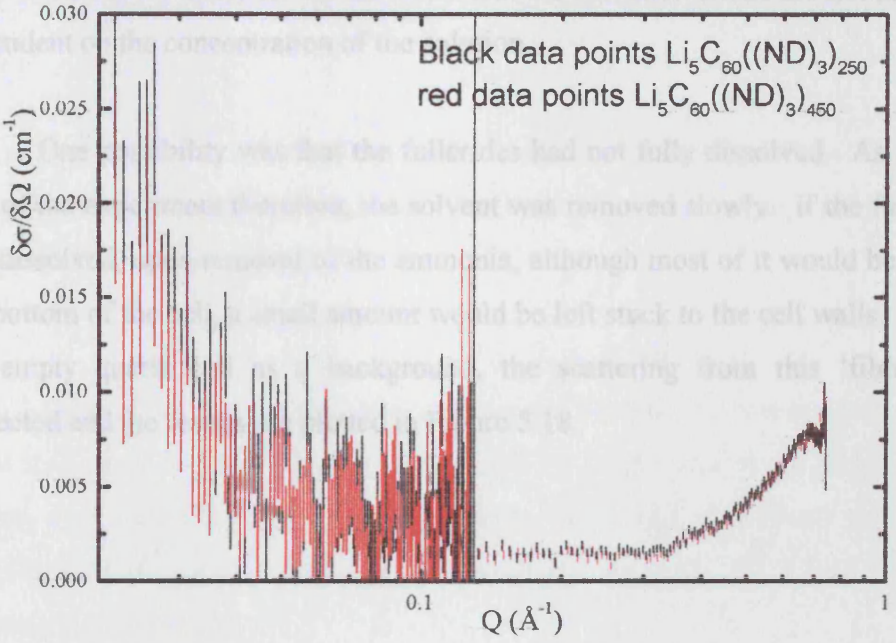

Figure 5.17: Measured SANS patterns for solutions of composition $Li_5C_{60}(ND_3)_{250}$ (black) and $Li_5C_{60}(ND_3)_{450}$ (red).

The data is plotted on a log scale of the x-axis down to a Q value of 0.02 Å^{-1}. Although the two data ranges match up there is a much larger error on lower-

Q data due to a larger background scattering from the cryostat and lower flux of neutrons at these values.

The tiny signal, although similar to the levels expected from the calculations, does not enable modelling of the inter-fulleride interactions in the solutions. The slight decrease in scattering with dilution is consistent with the reduction of the volume fraction. The small size of the signal, however, means that such slight differences are very dependent on many parameters such as the transmission through the sample. The rising signal at the high-Q end is absent from the background solvent data and could be the onset of the intermediate range order, attributed to the solvation shells around the C_{60}, seen in the SANDALS data. If this is the case, the results show that the solvation shells are not strongly dependent on the concentration of the solution.

One possibility was that the fullerides had not fully dissolved. As a final part of the experiment therefore, the solvent was removed slowly. If the fulleride had dissolved, upon removal of the ammonia, although most of it would be left at the bottom of the cell, a small amount would be left stuck to the cell walls. Using the empty quartz cell as a background, the scattering from this 'film' was corrected and the results are plotted in Figure 5.18.

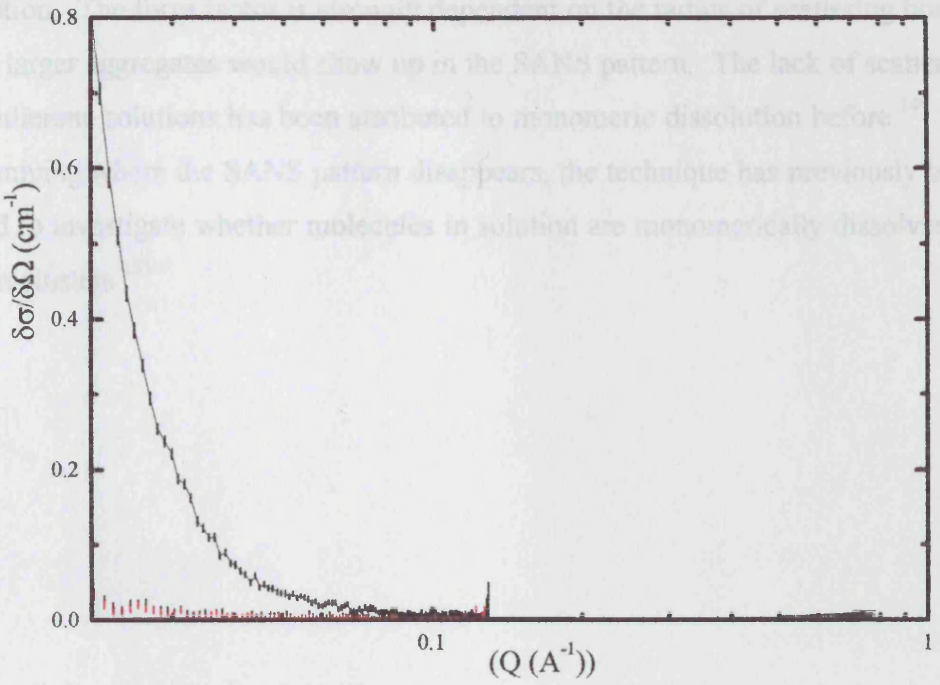

Figure 5.18: SANS scattering from the 'thin film' of fullerides left on the on the cell walls after removal of the solvent. The scattering from the fulleride solutions is also shown.

Figure 5.18 shows that upon removal of the solvent, we are left with a small amount of fulleride on the cell walls which results in a much larger SANS pattern than that from the original solution. Although this result cannot be quantified, it shows that the fullerides were dissolved in the SANS patterns presented in Figure 5.17.

5.3.4 Conclusions

The results from the SANS studies do not directly measure the inter-fulleride structure of metal-ammonia-fulleride solutions. The small size of the measured signal is due to the small size of the fullerides anions and the fact that SANS instruments are not optimised for sensitive measurements. Importantly, however, the results confirm that we have dispersions of fullerides rather than clusters in

solution. The form factor is strongly dependent on the radius of scattering bodies and larger aggregates would show up in the SANS pattern. The lack of scattering in fullerene solutions has been attributed to monomeric dissolution before.[149] By examining where the SANS pattern disappears, the technique has previously been used to investigate whether molecules in solution are monomerically dissolved or form clusters.[153]

Chapter 6

Results II: Computer Simulations

6.1 Introduction

This chapter presents the results of Monte Carlo (MC) simulation studies of metal-ammonia-fulleride solutions. The first section of this chapter details the parameters, potentials, and the general method followed in performing the simulations. In order to examine how closely the simulations describe the real solutions, the next section compares simulation results to the diffraction data presented in Chapter 5. The chapter goes on to investigate the effect of varying fulleride charge and cationic species on the structure and the thermodynamics of the solution.

6.2 Simulation Details

6.2.1 Interatomic Potentials

Throughout the simulations interatomic interactions were represented by effective pair potentials of the form:

$$V_{ij}(r_{ij}) = \frac{q_i q_j}{r_{ij}} + 4\varepsilon_{\alpha\beta}\left[\left(\frac{\sigma_{\alpha\beta}}{r_{ij}}\right)^{12} - \left(\frac{\sigma_{\alpha\beta}}{r_{ij}}\right)^{6}\right]. \qquad 6.1$$

Values for the parameters used are given in Table 6.1. Where atomic species differ, the Lorentz-Berthelot mixing rules are used (see Chapter 4).

Atom Type	σ (Å)	ε (kcal mol^{-1})	q (e)
K[145]	2.58	1.89	1.00
N[143]	3.42	0.17	-1.02
H[143]	0.0	0.0	0.34
C[146]	3.80	0.0659	-n/60
Li[144]	1.25	6.25	1.00
Na[144]	1.89	1.60	1.00
Ca[145]	2.41	0.46	2.00

Table 6.1: Lennard-Jones pair potentials used in the MC simulation.

The ammonia molecule that was used in the simulations was the 4-site OPLS model.[143] This has rigid bond lengths and angles, and Coulomb charges were placed on the hydrogen and nitrogen atoms to represent the electrostatic moment of the molecule. This model has been successfully employed in recent studies of bulk ammonia, lithium-ammonia and calcium-ammonia solutions.[129,135]

Several classical potentials have been used to model C_{60}, and two general methods of representing C_{60} molecules in simulations have been employed. The first representation was developed by Girifalco.[154] This treats the C_{60} as a single, spherically symmetric interaction site. By averaging the potential of all the interactions of the carbon atoms between two different fullerenes, an effective average C_{60}-C_{60} potential was established. The other method is to use a fully atomistic representation of C_{60} in which the carbon atoms are fixed in their conventional, molecular positions over the molecule. In implementing the first model, Girifalco used potentials obtained by computing the fullerite lattice energy, using first, second and third neighbour interactions, with measurements of the enthalpy of sublimation and lattice parameter. For the atomistic model, several different carbon potentials have been proposed, for example, potentials based on graphite[155] or for general sp^2 carbon centres.[146]

Of the two methods of representing C_{60}, the Girifalco model is clearly quicker computationally and almost essential for use in systems consisting of many C_{60}s. Recent studies have concluded that whilst the Girifalco potential provides a useful qualitative depiction, the atomistic model provides a much more reliable description and should be used for primary investigations.[156]

Due to the fact that a relatively small number of C_{60}s were used in my simulations, and that the solvation of the ammonia molecules might hinder the rotation of the C_{60} at the relevant temperatures, the atomistic model was used. The carbon Lennard-Jones potentials were taken from the literature for one of the first simulation publications on C_{60}, which correctly predicts the fcc crystal structure that is adopted in the solid state at room temperature.[146] The charge for the fulleride C_{60}^{n-} was placed fractionally on each carbon atoms, i.e. $-n/60$ on each carbon. In Chapter 7 sharp, single peaks for the individual ^{13}C NMR shifts confirm the carbon atoms electronic equivalence upon the introduction of charge to the fullerenes in these solutions. A 'dummy' atom was placed at the centre of the C_{60} cage to permit radial distribution functions to be plotted around the C_{60}'s centre of mass.

6.2.2 Boundary Conditions and Simulation Cells

Throughout the simulations, 3-dimensional periodic boundary conditions were implemented as described in Chapter 4. The minimum image convention[139] restricts the examination of local order to a distance of no greater than $L/2$, where L is length of the simulation box. Inter-fulleride distances are of the order of ~21Å, in the concentrated solutions studied here, if the fullerides are dispersed uniformly. To satisfactorily investigate the inter-fulleride structure of the solutions, an absolute minimum box length at least twice a big as this is required, i.e. ~42Å, containing at least 8 fullerides. This proved impractically large for reasonable equilibration times, with current computing processing power.

The first part of this chapter simulates the solution of composition $K_5C_{60}(NH_3)_{250}$, the structure of which was measured in Chapter 5. The ensemble representing this system contains 4 C_{60}, 20 K^+, and 1000 NH_3. This was large enough to extract a satisfactorily averaged solvent structure and small enough ($33Å^3$) to require sensible equilibration times.

The second part of this chapter examines the structure of the solutions as a function of electronic charge and cationic species. For this, simulations consist of one fulleride, 400 NH_3, and the relevant number of cations. The fulleride number was kept to one, in order to reduce equilibration times. The fulleride was surrounded by the increased number of 400 NH_3 to reduce boundary effects of the C_{60} solvation shell that might result from the smaller simulation box. The box sizes were all approximately $25Å^3$.

6.2.3 Physical Parameters and Cut-offs

The simulations were all performed at a temperature of 220K and pressure of 1atm. The Ewald sum cut-off parameters used were 0.2 and 2.5 for α, and the k-space cut-off respectively and 10Å as the real space cut-off.[126] A value of 10Å was used throughout as the real space Lennard-Jones cut off.

6.2.4 General Method

In all cases the densities of the systems studied were unknown. For the solution with a composition identical to the neutron experiment, an initial value of the density was taken to be 1.4 that of ammonia. This was estimated from the absorption measurements taken during the SANDALS experiment (see Chapter 5). A simulation was then set up with this value in an isothermal-isobaric (constant pressure) ensemble, (N, p, T). Equilibrium was conceded when the volume and energy fluctuated about their means. Once the density was established it was then used for a (N, V, T) simulation. This procedure was adopted because the $g(r)$s are calculated cumulatively and as the box size is fluctuating, the $g(r)$s fall off/increase in the expanded/contracted regions during the (N, p, T) ensemble.

The same method was used to determine the densities of all the other systems studied, starting with the same initial estimated density. A typical number of iterations required to establish equilibrium was ~12-15M per system, for the two successive ensembles. This gave enough time for the solvent molecules to equilibrate with respect to the ions. Some caution must be taken in examining the ion-ion structure as the ions are relatively dilute in solution and therefore take longer to fully equilibrate with respect to each other.

Together with the initial simulation, simulations of neutral C_{60} in ammonia and C_{60}^{2-}, C_{60}^{4-} and C_{60}^{6-} were undertaken. The simulations were all performed in ensembles consisting of 400 NH_3, 1 C_{60}^{n-} and n ions. In the final part of this chapter, systems containing 1 C_{60}^{4-} and 400 NH_3 were simulated with differing cations: 2 Ca^{2+}, 4 Li^+ and 4 Na^+.

A typical molecular graphics snap-shot of a simulation ensemble is shown in Figure 6.1.

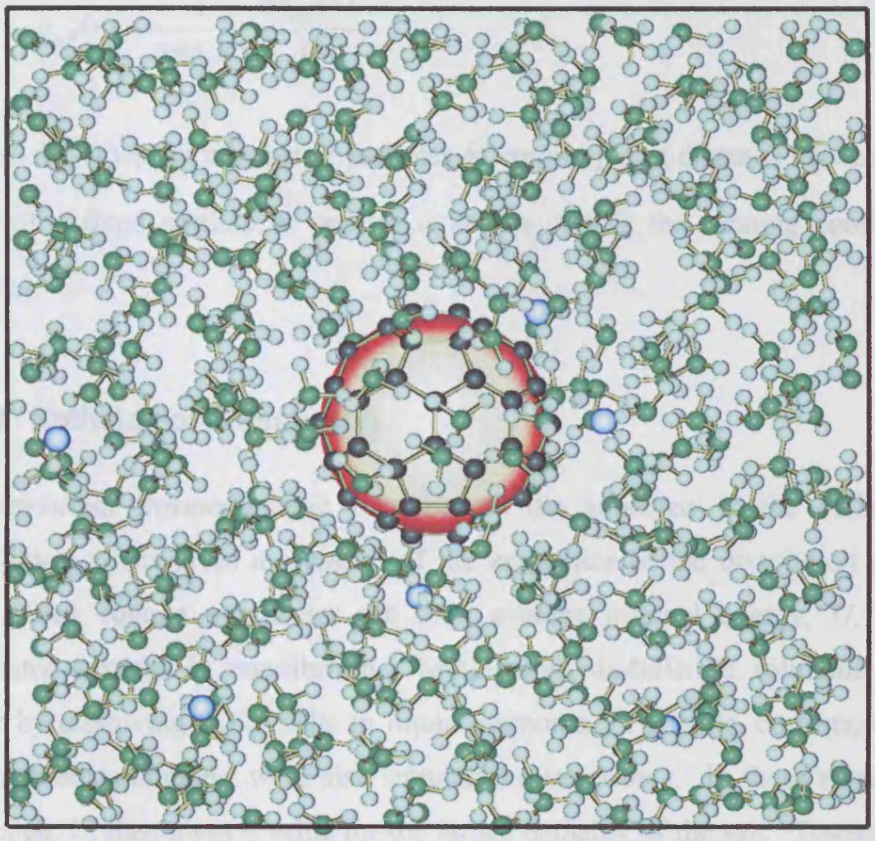

Figure 6.1: Molecular graphics snapshot of the MC simulated solution composition, $K_6C_{60}(NH_3)_{400}$. Key: carbon atoms – black, potassium cations – blue, hydrogen atoms – white, and nitrogen atoms – green.

6.3 Simulation Analysis

Two methods were used to investigate the results from the simulations: the calculation of the enthalpy of dissolution, and the extraction of the pair distribution functions of the system.

6.3.1 Pair Distribution Functions

1-dimensionally averaged radial pair distribution functions were plotted from the simulation data using the definition:

$$g_{\alpha\beta}(r) = \frac{1}{4\pi\rho_\beta r^2}\frac{dn_{\alpha\beta}(r)}{dr}, \qquad 6.2$$

where $dn_{\alpha\beta}(r)$ is the number of particles of species β at a distance between r and $r+dr$ of a fixed particle of species α and $n_{\alpha\beta}(r)$ is the running coordination number.

6.3.2 Enthalpy of Dissolution

An important thermodynamic property of the solutions is the enthalpy of dissolution. This gives a measure of the energetics of the dissolution process. The *Monte* routine establishes the total average internal energy, U, for the simulated systems in equilibrium. Metal-ammonia-fulleride solutions can be made by dissolving A_nC_{60} salts in liquid ammonia. The salts, corresponding to the simulated solutions, were also simulated using *Monte*. In these simulations, the value, U, then gives a value for the lattice enthalpy of the salt. Together with results from a simulation of pure ammonia, the cycle shown in Figure 6.2 and equation 6.3, was used to calculate the enthalpy of dissolution. If the enthalpy of dissolution is negative, the dissolution of the salts is enthalpically favoured.

$$\Delta H_s = U_{soln} - \left(U_{ammonia} + U_{crystal}\right) \qquad 6.3$$

Throughout this work the U resulting from the simulation of the salt is referred to as the 'lattice enthalpy', U from the ammonia solution the 'solvent enthalpy', U from the solution as the 'solution enthalpy', and ΔU as 'the enthalpy of dissolution'.

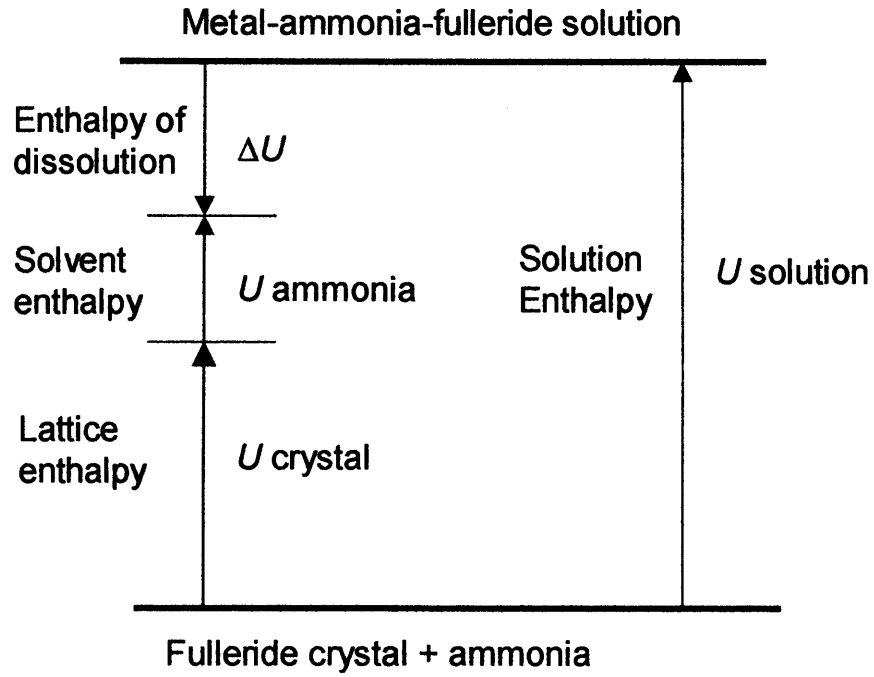

Figure 6.2: Definition of the enthalpy of dissolution. In all cases, U is the average internal energy of the respective systems at equilibrium. ΔU is a measure of the enthalpy of dissolution.

The A_nC_{60} salts were simulated using a box consisting at least 16 C_{60} anions. The ions were placed in the simulation in positions derived from an approximate bcc representation of the C_{60} salts[9] or the fcc positions in the case of the pure fullerite crystal itself. The crystals were initially set up in slightly increased volumes from those found in the literature and then allowed to come to equilibrium under the isothermal-isobaric ensemble. The initial setups of the crystals are shown in Figure 6.3. The same method was used to simulate the crystals, Na_4C_{60}, Li_4C_{60}, and Ca_2C_{60}.

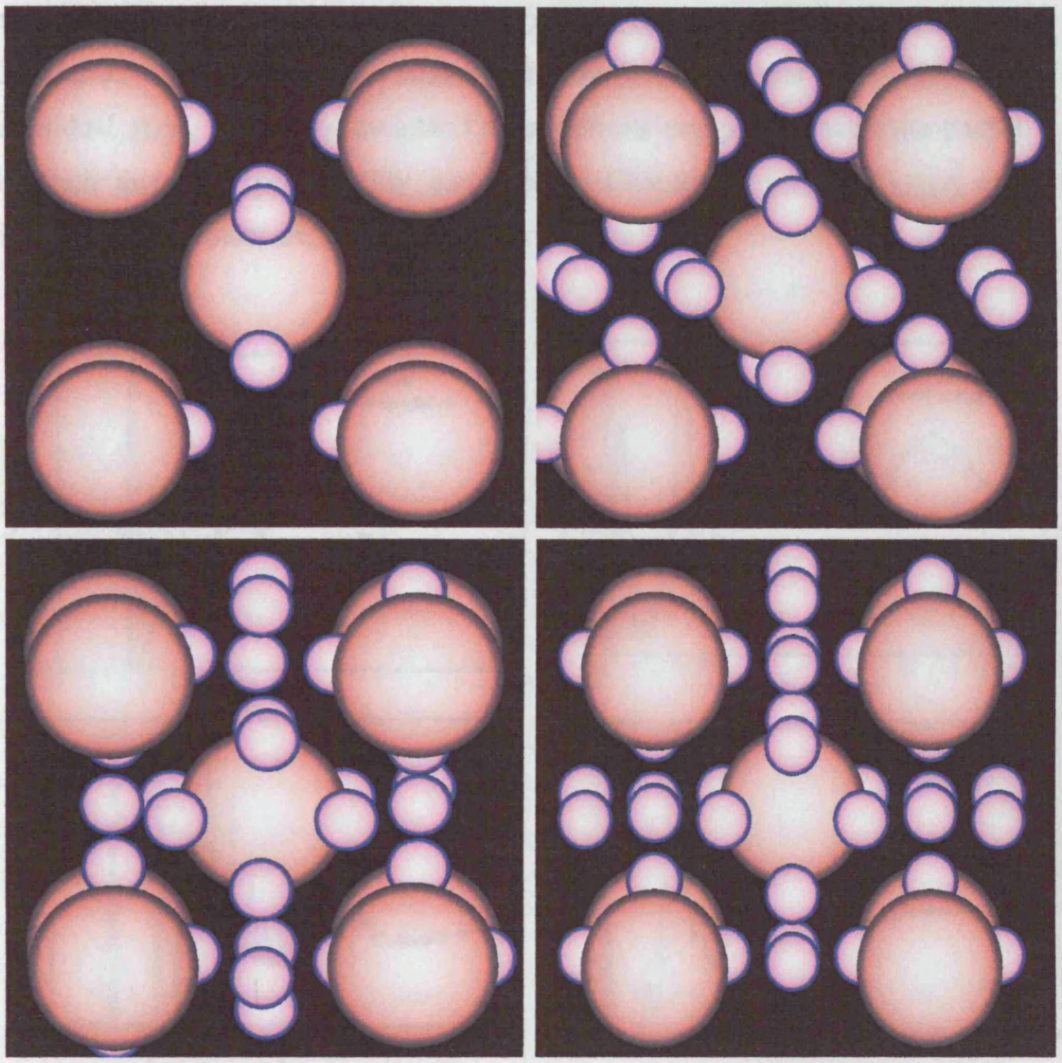

Figure 6.3: Snapshots of the approximate starting configurations for the simulations of potassium fulleride salts. Clockwise from top: K_2C_{60}, K_4C_{60}, K_6C_{60} and K_5C_{60}. Grey spheres – C_{60} anions, blue spheres – K^+.

6.4 Results and Discussion I: Potassium-Fulleride-Ammonia Solution, $K_5C_{60}(NH_3)_{250}$

A simulation of the solution composition, $K_5C_{60}(NH_3)_{250}$, was undertaken. From the equilibrated ensemble the 10 individual site-site radial distribution functions, the $g_{\alpha\beta}(r)$s, were extracted. Summation of these functions with their relative neutron weightings (see Table 5.1) permits a direct comparison to the composite

partial distribution functions: $g_{HH}(r)$, $g_{XH}(r)$ and $g_{XX}(r)$, measured and presented in Chapter 5. This comparison is shown in Figure 6.4. A Fourier transform of the individual $g(r)$s, before the weighted sum, permits comparison with the partial structure factors, experimentally measured in Chapter 5: $S_{HH}(Q)$, $S_{XH}(Q)$ and $S_{XX}(Q)$. These results are shown in the same figure.

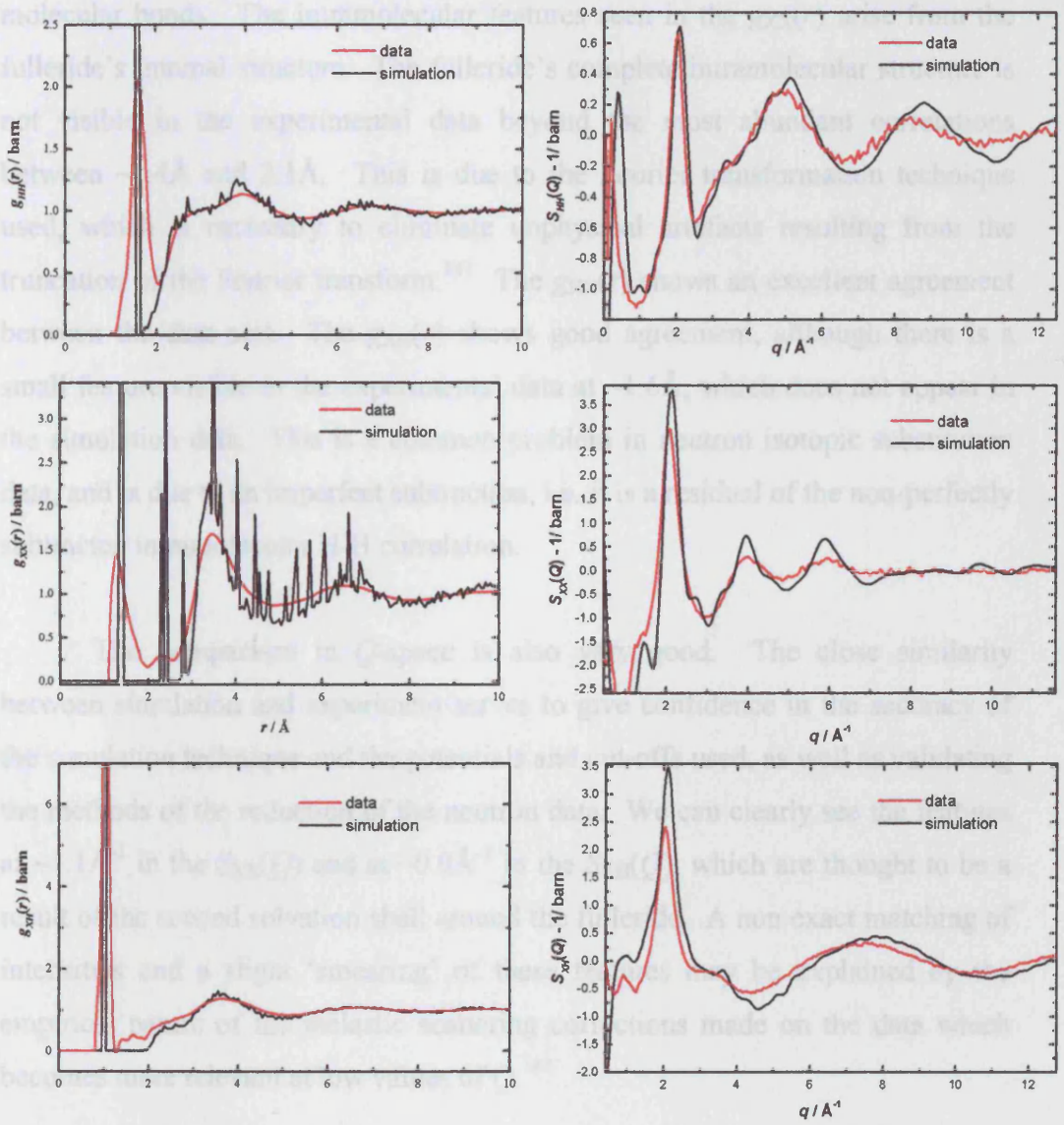

Figure 6.4: The structure of solution composition $K_5C_{60}(NH_3)_{250}$. A comparison between MC simulation (black curves) and neutron data (red curve). Partial $S(Q)$s are shown on the left, partial $g(r)$s on the right.

An examination of Figure 6.4 reveals close agreement between the simulation results and the experimental data. In more detail, starting with the real space functions, the expected intramolecular correlations below 2Å in the three sets of data can be seen. The simulation uses molecules with fixed bond lengths which give rise to very sharp intramolecular features in the data. These distances are less sharply defined in the neutron data due to dynamic nature of real molecular bonds. The intramolecular features seen in the $g_{XX}(r)$ arise from the fulleride's internal structure. The fulleride's complete intramolecular structure is not visible in the experimental data beyond the most abundant correlations between ~1.4Å and 2.1Å. This is due to the Fourier transformation technique used, which is necessary to eliminate unphysical artefacts resulting from the truncation of the Fourier transform.[141] The $g_{HH}(r)$ shows an excellent agreement between the data sets. The $g_{XH}(r)$ shows good agreement, although there is a small feature visible in the experimental data at ~1.6Å, which does not appear in the simulation data. This is a common problem in neutron isotopic substitution data, and is due to an imperfect subtraction, i.e. it is a residual of the non-perfectly subtracted intramolecular H-H correlation.

The comparison in Q-space is also very good. The close similarity between simulation and experiment serves to give confidence in the accuracy of the simulation technique and the potentials and cut-offs used, as well as validating the methods of the reduction of the neutron data. We can clearly see the features at ~1.1Å^{-1} in the $S_{XX}(Q)$ and at ~0.9Å^{-1} in the $S_{XH}(Q)$, which are thought to be a result of the second solvation shell around the fulleride. A non exact matching of intensities and a slight 'smearing' of these features may be explained by the empirical nature of the inelastic scattering corrections made on the data which becomes more relevant at low values of Q.[147]

The individual $g(r)$s are very similar to those obtained from the EPSR analysis and are discussed in Chapter 5, so are not re-examined here. A discussion of the way in which the EPSR technique has modified the interatomic potentials to account for the discrepancies between the simulation and data, is

beyond the scope of this thesis. The origins of the low-Q features can be examined by 'breaking up' the individual contributions to the $S_{XH}(Q)$ and $S_{XX}(Q)$. These results are shown in Figure 6.5. In both cases the $S(Q)$s involving the potassium correlations are not included due to their very small neutron weightings.

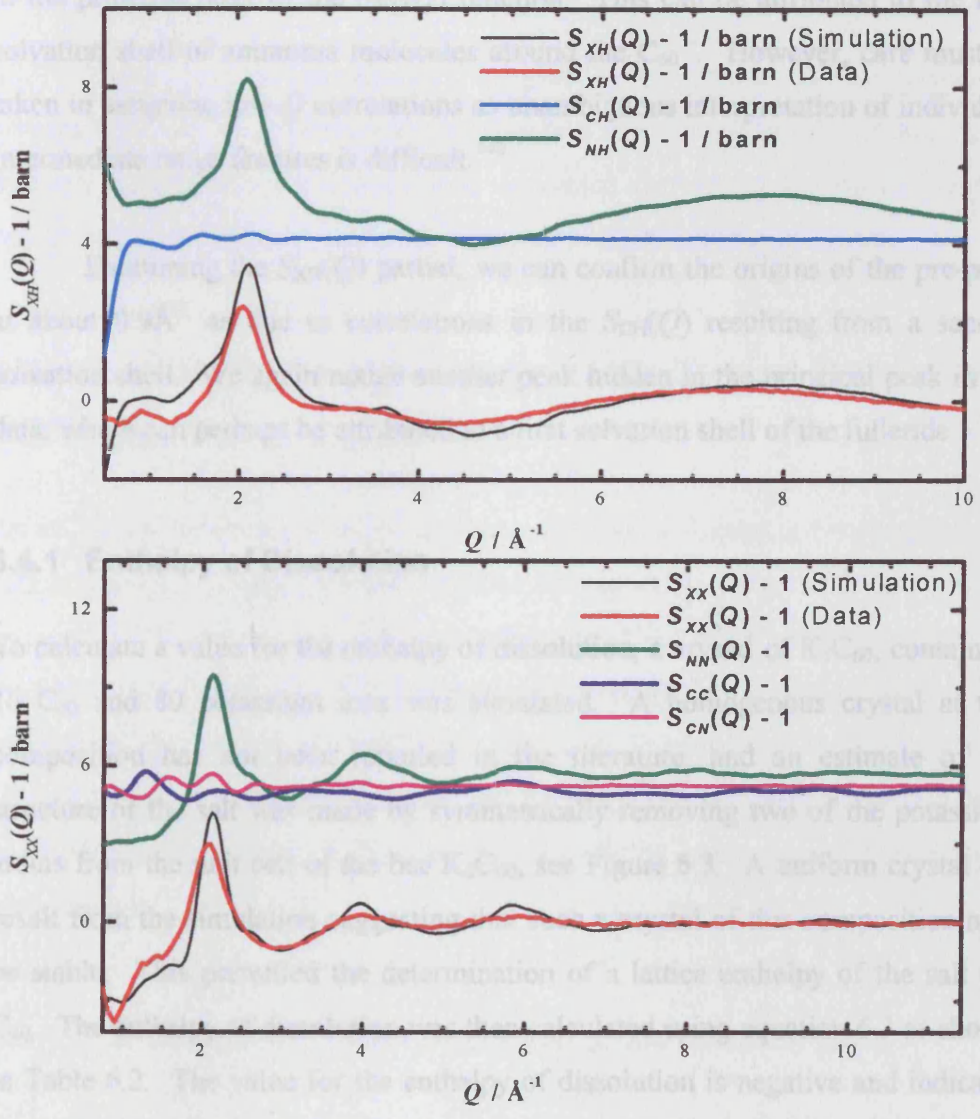

Figure 6.5: Individual partial structure factors' contributions to the shape of the measured $S_{XH}(Q)$ and $S_{XX}(Q)$. The individual $g(r)$s are extracted from the simulations, Fourier transformed, and then summed with their neutron weighting.

In the $S_{XX}(Q)$ function both the $S_{CN}(Q)$ and the $S_{CC}(Q)$ contribute to the shoulder on the principal peak in the neutron data. These features can be seen to arise from intramolecular, across ball C-C correlations, as well as C-N correlations. The peak in the $S_{CN}(Q)$ is consistent with the two solvation shell model with the correlations arising from the second solvation shell of ammonias around the C_{60}. There is another peak in the $S_{CN}(Q)$ at ~2.1Å^{-1}, which is 'hidden' in the principal peak of the $S_{XX}(Q)$ function. This can be attributed to the first solvation shell of ammonia molecules around the C_{60}^{5-}. However, care must be taken in assigning low-Q correlations as unambiguous interpretation of individual intermediate range features is difficult.[142]

Examining the $S_{XH}(Q)$ partial, we can confirm the origins of the pre-peak at about 0.9Å^{-1} as due to correlations in the $S_{CH}(Q)$ resulting from a second solvation shell. We again notice another peak hidden in the principal peak in the data, which can perhaps be attributed to a first solvation shell of the fulleride.

6.4.1 Enthalpy of Dissolution

To calculate a value for the enthalpy of dissolution, a crystal of K_5C_{60}, containing 16 C_{60} and 80 potassium ions was simulated. A homogenous crystal at this composition has not been reported in the literature, and an estimate of the structure of the salt was made by symmetrically removing two of the potassium atoms from the unit cell of the bcc K_6C_{60}, see Figure 6.3. A uniform crystal did result from the simulation suggesting that such a crystal of this composition may be stable. This permitted the determination of a lattice enthalpy of the salt per C_{60}. The enthalpy of dissolution was then calculated using equation 6.3 as shown in Table 6.2. The value for the enthalpy of dissolution is negative and indicates the formation of the solutions is enthalpically favourable with respect to forming the salt and the pure solvent.

U total for solution of $K_5C_{60}(NH_3)_{250}$ (kcal mol^{-1})	-2598±21
U total for 1 unit of K_5C_{60} (kcal mol^{-1})	-1303±6
U total for 250 NH_3 (kcal mol^{-1})	-1254±20
ΔU Enthalpy of formation (kcal mol^{-1})	-41±29

Table 6.2: Calculation of the enthalpy of dissolution for $K_5C_{60}(NH_3)_{250}$.

These opening results serve to give us confidence in the simulation potentials as well as permitting an investigation into the origins of certain specific features in the experimental data. This simulation also provides a measurement of the density of the solution and gives a measure of the enthalpy of dissolution.

6.5 Results II: The Effect of Fulleride Charge, Simulations of Composition $K_nC_{60}^{n-}(NH_3)_{400}$

An important parameter of metal-ammonia-fulleride solutions is the charge on the fulleride anion. Control over the electronic charge of the fulleride[6] is an attractive property of these solutions. Understanding the effect of fulleride charge on the mechanism of dissolution is important in the exploitation of the solutions. The propensity of the salt to crystallise out in solution is also likely to depend on the charge density of the fulleride anion. Highly charged molecules are rarely seen to exist in solution as the strength of the lattice enthalpy increases significantly with ionic charge.[157]

6.5.1 The Simulated Crystal Structures of the Fulleride Salts

A large amount of the work on fullerenes and their derivatives to date has concentrated on the fulleride salts. It is therefore significant to discuss the results of the simulations of these salts. The results of this classical MC study are compared with experimental data for the salts and the fullerite crystal.

Early calculations revealed that nearest neighbour interactions dominated the lattice enthalpy of pure fullerite C_{60} crystal.[154] In the simulation of pure fullerite here, 32 C_{60}s were used, producing the expected fcc structure, and the established lattice enthalpy was ~50±4 kcal/mol per C_{60} (see Table 6.3). This value compares with a value of the sublimation enthalpy of 41 ± 6kcal/mol at 298K, which is an average of several experimental measurements.[35] The difference in temperatures may explain the discrepancy between the values.

K_4C_{60} was set up using the standard cubic representation of the fulleride crystal with the potassium atoms placed in the approximate positions.[7] Allowing this system to equilibrate under the isothermal-isobaric ensemble, results in a reduction in the c-direction similar to the bct distortion seen in the experimentally measured structure of this crystal. The unit cell measured by synchrotron diffraction and Reitveld refinement has dimensions a = b = 11.87Å, c = 10.79Å.[158,159] This compares with the simulation results of: a = b = 12.0 ± 0.1, c = 10.5 ± 0.1. The discrepancies may be explained by the difference in temperature of the measurements, the fact that the experimental measurements had small traces of the fcc K_3C_{60} and K_6C_{60},[158] or subtle differences in the bond lengths and potentials in fulleride crystals not accounted for by the classical simulation. The average fulleride separation in the simulations is found to be ~9.95Å similar to the experimentally measured 9.98Å.[158]

The K_6C_{60} simulation reproduces the bcc structure that is measured experimentally measured. The nearest centre C_{60}-C_{60} distances of 10Å is also similar to those measured experimentally.[7]

A homogenous crystal of K_2C_{60} has not been reported in the literature and a uniform crystal does not result from the simulation. However, the simulation does permit a quantitative discussion of the thermodynamics of solution. Recent simulation work has shown that at this concentration a combination of the thermodynamically stable K_3C_{60} and pure C_{60} form.[160]

6.5.2 Enthalpies of Dissolution and Solution Densities

The enthalpies of dissolution as well as the individual lattice enthalpies and solution enthalpies are shown in Table 6.3.

	C_{60}^{6-}	C_{60}^{4-}	C_{60}^{2-}	C_{60}
U, $K_XC_{60}(NH_3)_{400}$ (kcal mol^{-1})	-3776±21	-3006±19	-2400±20	-2002±19
U, 1 unit of K_XC_{60} (kcal mol^{-1})	-1750±4	-923±3	-320±8	-50±4
U, 400 NH_3 (kcal mol^{-1})	-2021±20	-2021±20	-2021±20	-2021±20
ΔU Enthalpy of Dissolution (kcal mol^{-1})	-3±29	-56±28	-59±29	+70±28

Table 6.3: Enthalpy of dissolution for the solutions $NH_3(400)$, C_{60}^{n-}, nK^+.

Here the enthalpy of dissolution is a small difference between the relatively large lattice + solvent enthalpies, and the solution enthalpy. Figure 6.6 plots the (negative) increase in lattice enthalpy *per* potassium ion as a function of the total number of potassium ions. The figure includes data for the simulation of the K_5C_{60} crystal.

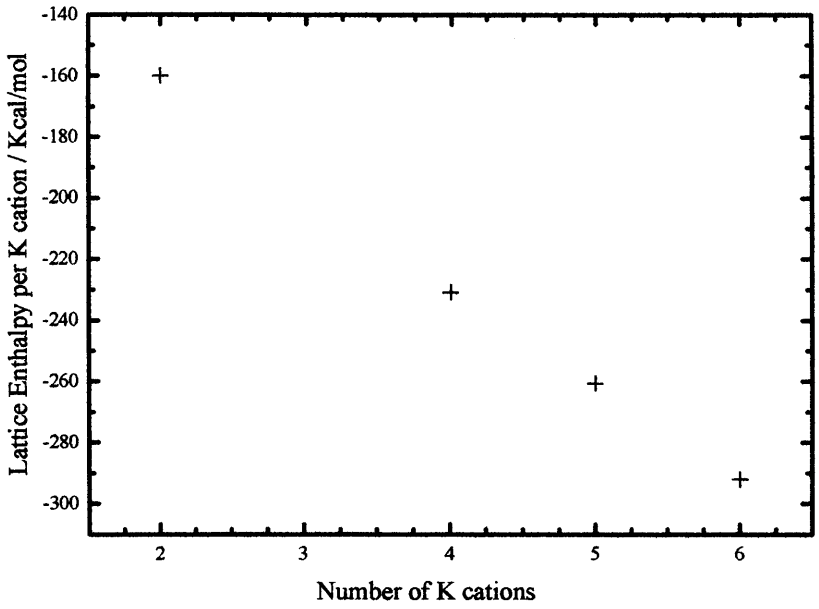

Figure 6.6: Lattice enthalpy per K^+ cation in the simulated crystal structures, K_2C_{60}, K_4C_{60}, K_5C_{60} and K_6C_{60}.

Figure 6.6 shows that as the number of potassium ions in the crystal is increased, the (negative) binding energy *per* potassium in the lattice also increases. Table 6.3 shows a distinct increase in solution enthalpy with increasing charge. However, this is more than offset by the faster rate of increase of lattice enthalpy. This means that as the number of potassium ions is increased, there is a value at which it is favourable for the salt to recombine: the enthalpy of dissolution will become positive. At the concentration simulated here, this value is approximately six potassium cations per fulleride, where the enthalpy of dissolution is -3±29 kcal/mol.

Some caution must be observed in the interpretation of the enthalpy of dissolution results however, as the entire phase diagrams of the systems have not been examined. This is most relevant in considering the number of ammonia molecules. For example, it is possible that an ammonia complexed salt and excess solvent is a more enthalpically stable system than a homogenous solution.

The results indicate that the solutions are all enthalpically stable with respect to the salt and pure solvent at the concentrations studied, with the exception of the solution of uncharged C_{60} in ammonia and possibly K_6C_{60}. This is consistent with observation: C_{60} fullerite is insoluble in ammonia. The solvation mechanism is then due to the charge on the anion. It is debatable whether the anion C_{60}^{6-} will form in potassium-ammonia-fulleride solutions at this concentration. The experiments on rubidium-ammonia-fulleride solutions,[6] which proved the sequential and reversible reduction of the C_{60} anion, showed that upon addition of more metal to C_{60}^{5-} ammonia solution the spectrum of the solvated electrons returned rather than the C_{60}^{6-} spectrum (see Section 1.7.2). In the case of the potassium-ammonia-fulleride solution for C_{60}^{6-}, the enthalpy of dissolution is almost zero within the errors suggesting that K_6C_{60} is far less readily soluble than the other C_{60} anions and the crystal is almost as enthalpically likely to be formed as the solution itself.

Table 6.4 records the bulk density of the solutions. These results are plotted in Figure 6.7.

	NH_3	C_{60}^{6-}	C_{60}^{4-}	C_{60}^{2-}	C_{60}
Density (gcm^{-3}) ± 0.01	0.70	0.80	0.79	0.76	0.72

Table 6.4: Densities of the simulated solutions of composition, $NH_{3(400)}$, C_{60}^{n-}, nK^+.

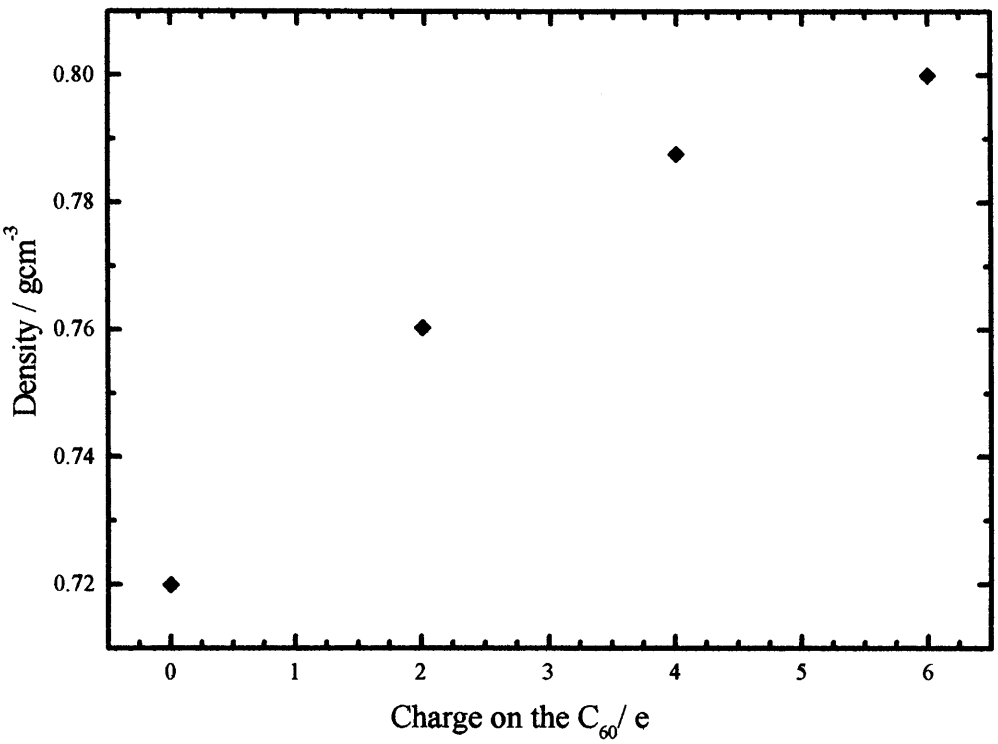

Figure 6.7: Dependence of solution density on fulleride charge, for the simulated solutions of composition, $(NH_3)_{400}$, C_{60}^{n-}, nK^+, n = 0, 2, 4 and 6.

There is an overall increase in solution density as the charge on the fulleride is increased. The density increase here appears to tend to a finite value. The increase is suggestive of an increase in organisation of the solvent around the anions.

6.5.3 Solvent-Solvent Structure

The solvent-solvent structure of the solutions, and its variation with fulleride charge, is examined by plotting the pair distribution functions, $g_{NH}(r)$, $g_{NN}(r)$, $g_{HH}(r)$. These functions, for the anions C_{60}^{n-} where n = 2, 4 and 6, as well as for pure ammonia, are shown in Figure 6.8.

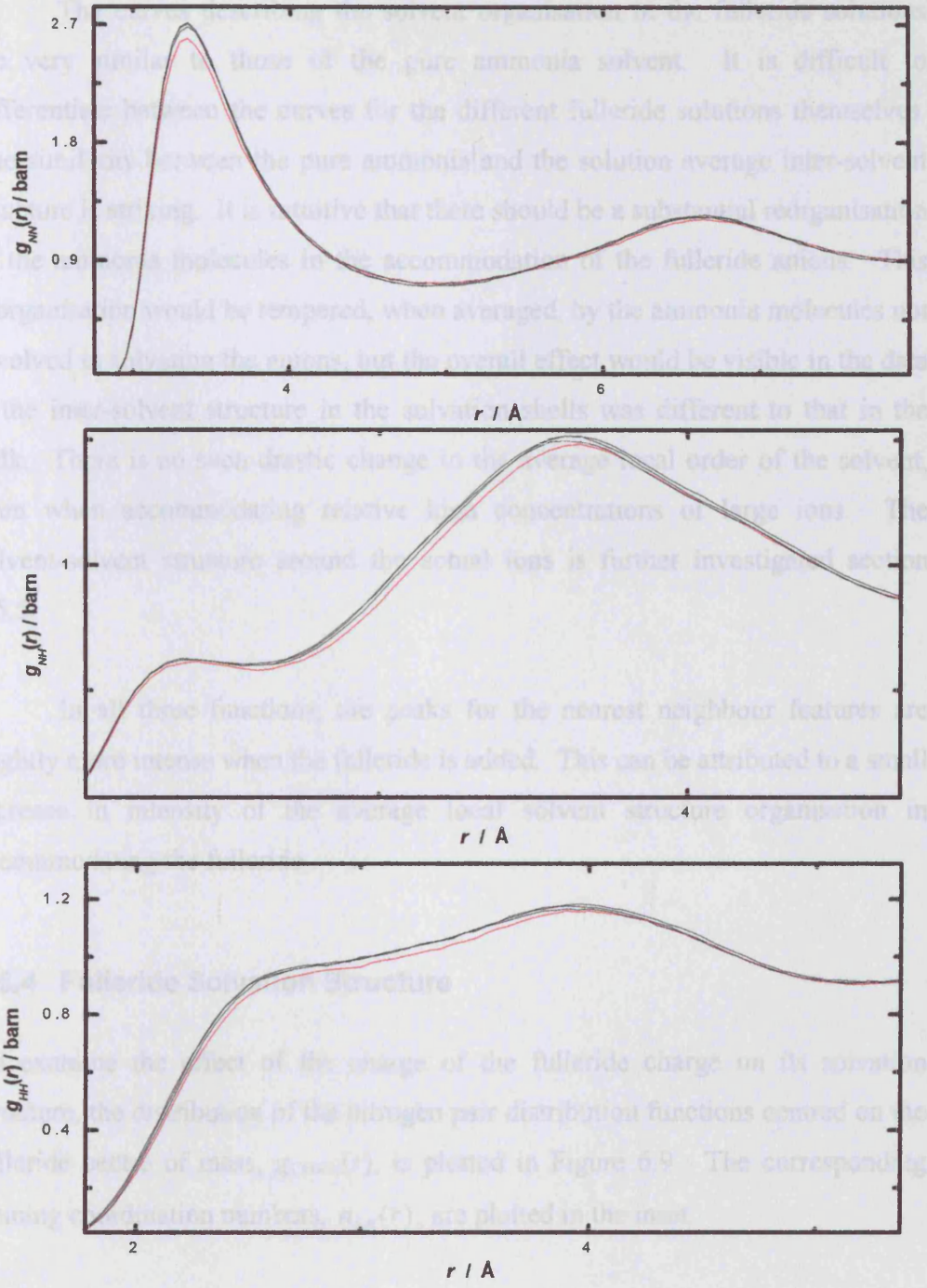

Figure 6.8: Solvent-solvent partial distribution functions for the simulated solutions, $NH_{3(400)}$, C_{60}^{n-}, nK^{+}, n = 2, 4 and 6 (black curves), and pure NH_3 (red curve). The figure shows $g_{NN}(r)$ (top), $g_{NH}(r)$ (middle), and $g_{HH}(r)$ (bottom).

The curves describing the solvent organisation in the fulleride solutions are very similar to those of the pure ammonia solvent. It is difficult to differentiate between the curves for the different fulleride solutions themselves. The similarity between the pure ammonia and the solution average inter-solvent structure is striking. It is intuitive that there should be a substantial reorganisation of the ammonia molecules in the accommodation of the fulleride anions. This reorganisation would be tempered, when averaged, by the ammonia molecules not involved in solvating the anions, but the overall effect would be visible in the data if the inter-solvent structure in the solvation shells was different to that in the bulk. There is no such drastic change in the average local order of the solvent, even when accommodating relative high concentrations of large ions. The solvent-solvent structure around the actual ions is further investigated section 6.5.5.

In all three functions, the peaks for the nearest neighbour features are slightly more intense when the fulleride is added. This can be attributed to a small increase in intensity of the average local solvent structure organisation in accommodating the fulleride.

6.5.4 Fulleride Solvation Structure

To examine the effect of the charge of the fulleride charge on its solvation structure, the distribution of the nitrogen pair distribution functions centred on the fulleride centre of mass, $g_{C60\text{-}N}(r)$, is plotted in Figure 6.9. The corresponding running coordination numbers, $n_{\alpha\beta}(r)$, are plotted in the inset.

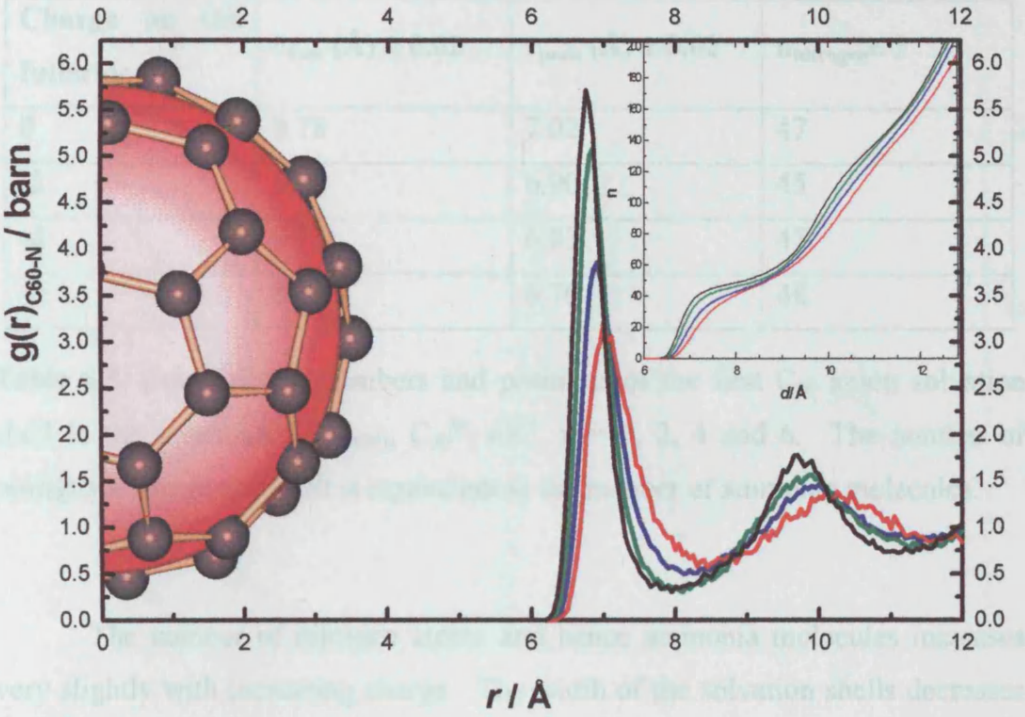

Figure 6.9: $g_{C60\text{-}N}(r)$, partial distribution functions of the distribution of nitrogen around C_{60}^{n-} anions in the solutions $NH_{3(400)}$, C_{60}^{n-}, nK^+, n = 0, 2, 4 and 6. Key: black – C_{60}^{6-}, green – C_{60}^{4-}, blue – C_{60}^{2-}, red – C_{60}. The corresponding running coordination numbers are shown in the inset.

Two distinct solvation shells of ammonia molecules around the fulleride can be seen in the data. The first shell is narrower than the second and the width of the two shells increases with decreasing charge on the fulleride anion. The number of ammonia molecules in the first shell is given by the number of nitrogen atoms in the first sharp peak of the $g_{C60\text{-}N}(r)$. The position of this peak, the number of atoms in this peak, and the maximum extent of this peak in r is recorded in Table 6.5.

Charge on the fulleride (e)	r_{max} (Å) ± 0.02	r_{peak} (Å) ± 0.02	$n_{nitrogen}$ ± 2
0	8.78	7.02	47
-2	8.29	6.90	45
-4	8.17	6.83	47
-6	8.02	6.76	48

Table 6.5: Coordination numbers and positions of the first C_{60} anion solvation shell in the solutions, $NH_{3(400)}$, C_{60}^{n-}, nK^+, n = 0, 2, 4 and 6. The number of nitrogen atoms in this shell is equivalent to the number of ammonia molecules.

The number of nitrogen atoms and hence ammonia molecules increases very slightly with increasing charge. The width of the solvation shells decreases with increasing charge. This decrease is consistent with the overall increase in density: the ammonia molecules approach the fulleride more closely the higher the charge on the fulleride. Figure 6.10 plots the, $g_{C60\text{-}H}(r)$, for the four solutions, to investigate the distribution of hydrogen atoms around the centre of the fulleride anions.

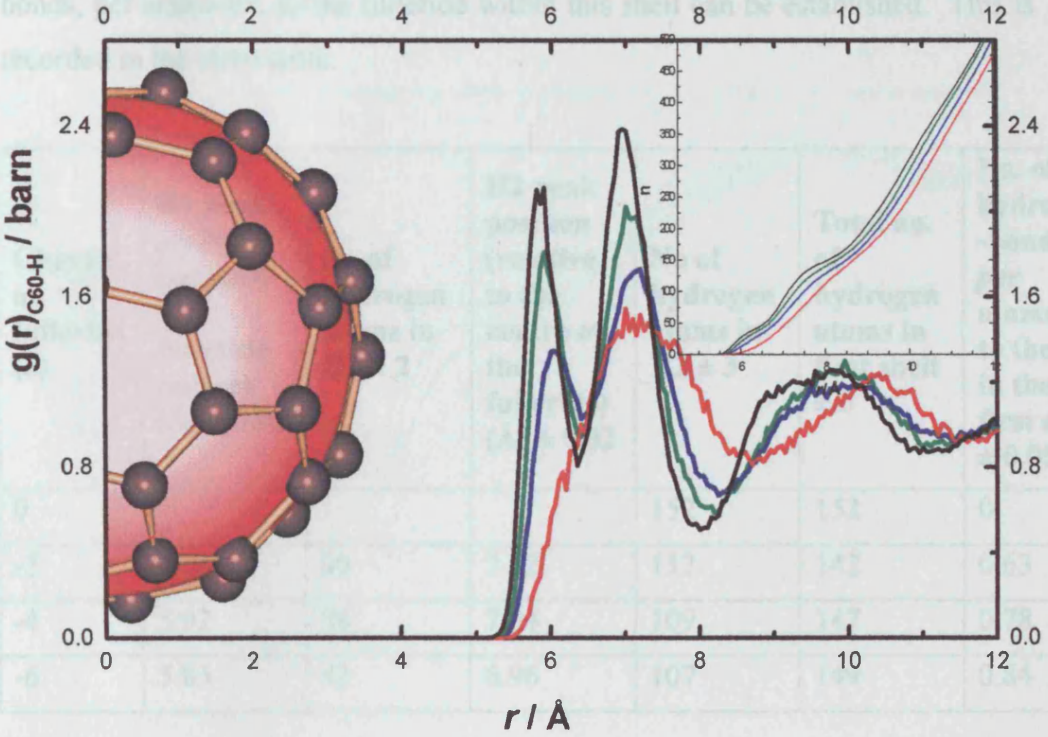

Figure 6.10: $g_{C60\text{-}H}(r)$, partial distribution functions of the distribution of hydrogen around C_{60}^{n-} anions in the solutions $NH_{3(400)}$, C_{60}^{n-}, nK^+, n = 0, 2, 4 and 6. Black – C_{60}^{6-}, green – C_{60}^{4-}, blue – C_{60}^{2-}, red – C_{60}. The corresponding running coordination numbers are shown in the inset.

A distinct orientational organisation of the ammonia molecules is evident within the first solvation shell, and manifests itself as two distinct hydrogen peaks in the $g_{C60\text{-}H}(r)$. This solvent organisation is also present in the second solvation shell and can be seen as an asymmetric peak at about 9Å. Integration of the first two peaks reveal that, on average, each of the first shells contain 3 hydrogen atoms per nitrogen, as expected. In the case of the first shell, the relative intensities of the two hydrogen peaks (below 8Å) vary with the charge on the anion. Table 6.6 records the coordination number of hydrogen atoms corresponding to these two peaks. The number of hydrogen atoms found in the first peak in the $g_{C60\text{-}H}(r)$ (H1 in the table) gives the number of hydrogen-bonds the ammonia molecules complete to the fulleride anion. If this is compared to the number of nitrogen atoms in the first shell, a value for the number of hydrogen-

bonds, per ammonia, to the fulleride within this shell can be established. This is recorded in the same table.

Charge on fulleride (e)	**H1 peak position (relative to fulleride centre) (Å) ± 0.02**	**No of hydrogen atoms in H1 ± 2**	**H2 peak position (relative to the centre of the fulleride) (Å) ± 0.02**	**No of hydrogen atoms in H2 ± 3**	**Total no. of hydrogen atoms in first shell ± 3**	**No. of hydrogen -bonds *per* ammonia to the C_{60} in the first shell. ± 0.05**
0				152	152	0
-2	6.04	30	7.12	112	142	0.63
-4	5.92	38	7.04	109	147	0.78
-6	5.83	42	6.96	107	149	0.84

Table 6.6: C_{60}-hydrogen coordination numbers for the distribution of hydrogen atoms within the first solvation shell. H1 and H2 are the first peak and second peaks in $g_{C60\text{-}H}(r)$ respectively.

These results show that with increasing charge, the number of hydrogen-bonds to the fulleride, per ammonia, in the first shell, approaches 1. With the fulleride charged to a maximum 6-, there is still less then 1 hydrogen-bond per ammonia to the anion. In the case of the uncharged fullerene, nearly all of the hydrogen atoms are further away from the C_{60} than the nitrogen atoms in the first shell ammonia molecules: there are no hydrogen-bonds formed to the C_{60}. This suggests that although the presence of the C_{60} does have an effect on the solvent, this does not result in a significant reorganisation of the solvent to complete the hydrogen-bond. Hydrogen-bonds only form when the fullerene is charged. This explains why the solution enthalpy of the uncharged fullerene in solution is not large enough for the dissolution to be enthalpically favourable.

To examine the solvation further and investigate hydrogen-bond distances, the $g_{CN}(r)$ and $g_{CH}(r)$ are plotted in Figure 6.11.

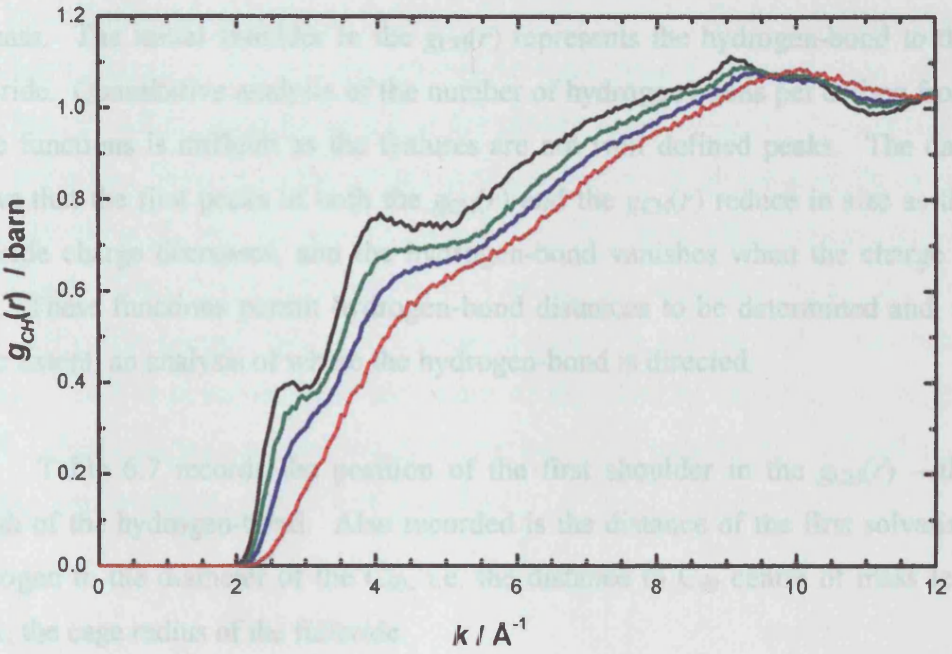

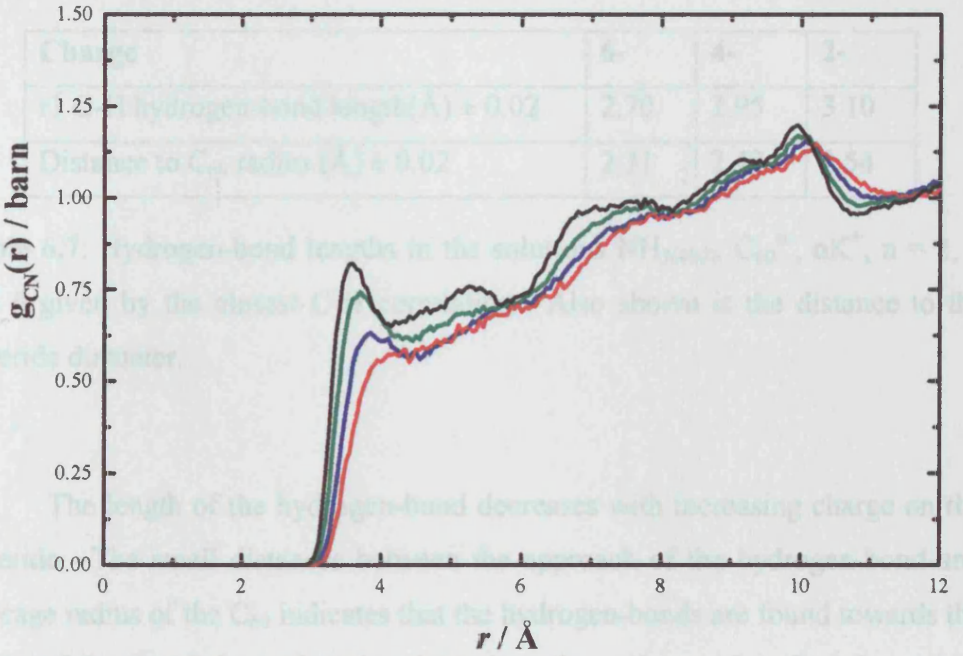

Figure 6.11: $g_{CH}(r)$s and $g_{CN}(r)$s, the distribution the solvent around the carbon atoms in the fulleride solutions $NH_{3(400)}$, C_{60}^{n-}, nK^{+}, n = 0, 2, 4 and 6. Key: C_{60}^{6-} black, C_{60}^{4-} (green), C_{60}^{2-} (blue), C_{60} (red).

With increasing charge there are more clearly defined hydrogen-bonds and initial C-N correlations, consistent with the data centred on the fullerides' centre of mass. The initial shoulder in the $g_{CH}(r)$ represents the hydrogen-bond to the fulleride. Quantitative analysis of the number of hydrogen atoms per carbon from these functions is difficult as the features are not well defined peaks. The data shows that the first peaks in both the $g_{CH}(r)$ and the $g_{CN}(r)$ reduce in size as the fulleride charge decreases, and the hydrogen-bond vanishes when the charge is zero. These functions permit hydrogen-bond distances to be determined and, to some extent, an analysis of where the hydrogen-bond is directed.

Table 6.7 records the position of the first shoulder in the $g_{CH}(r)$ – the length of the hydrogen-bond. Also recorded is the distance of the first solvating hydrogen to the diameter of the C_{60}, i.e. the distance to C_{60} centre of mass less 3.5Å, the cage radius of the fulleride.

Charge	**6-**	**4-**	**2-**
r1 C-H hydrogen-bond length(Å) ± 0.02	2.70	2.95	3.10
Distance to C_{60} radius (Å) ± 0.02	2.31	2.42	2.54

Table 6.7: Hydrogen-bond lengths in the solutions $NH_{3(400)}$, C_{60}^{n-}, nK^{+}, n = 2, 4 and 6 given by the closest C-H correlation. Also shown is the distance to the fulleride diameter.

The length of the hydrogen-bond decreases with increasing charge on the fulleride. The small distances between the approach of the hydrogen-bond and the cage radius of the C_{60} indicates that the hydrogen-bonds are found towards the centre of the 5 and 6 membered carbon rings themselves rather than the carbon atoms themselves.

6.5.5 Intra-Shell Solvent Structure

The investigation of the solvent structure in section 6.5.3 tells us that there is no significant change in the average solvent structure upon the introduction of the fulleride. It is clear from the data that the solvent forms distinct solvation shells around the C_{60}. How the inter-solvent structure varies within these shells can be investigated by plotting the solvent $g(r)$s, averaged over specific regions, not the whole box. The solvent $g(r)$s are determined for the molecules within the first shell, within the second shell, and the area beyond the second shell – the 'bulk' solvent. That is distances from the centre of the fulleride of 0-8Å, 8-12Å and >12Å. This analysis was performed for the solutions containing C_{60}^{6-} and C_{60}^{2-} anions. The results are plotted in Figure 6.12.

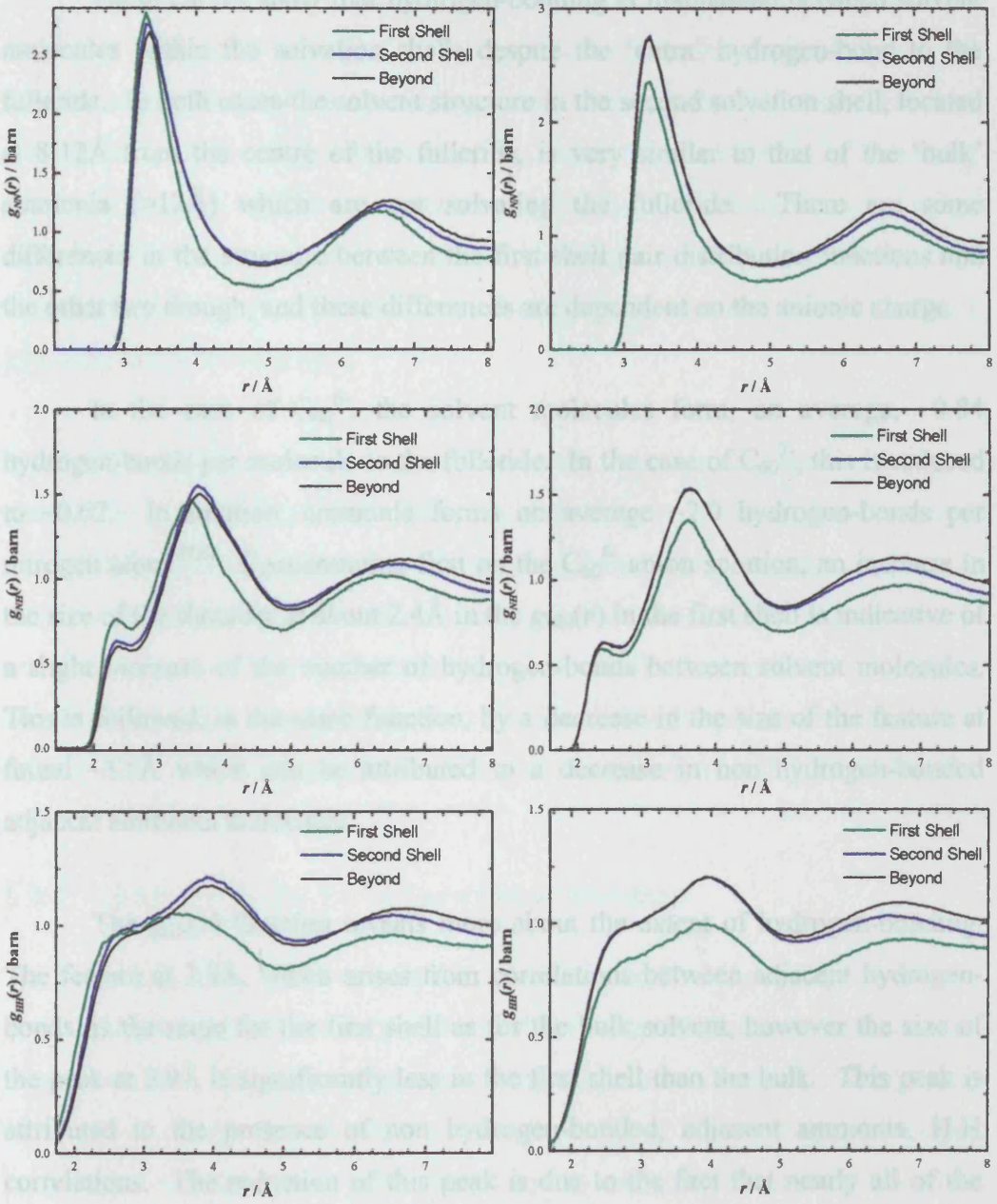

Figure 6.12: Solvent-solvent structure within the fulleride solvation shells for C_{60}^{6-}, $6K^+$, 400 NH_3 (left) and C_{60}^{2-}, $2K^+$, 400 NH_3 (right). The figure plots $g_{NN}(r)$ (top), $g_{NH}(r)$ (middle) and $g_{HH}(r)$ (bottom), for the first (green) second (blue) solvation shells and the volume beyond these shells (black).

These curves show that hydrogen-bonding is maintained between solvent molecules within the solvation shells despite the 'extra' hydrogen-bond to the fulleride. In both cases the solvent structure in the second solvation shell, located at 8-12Å from the centre of the fulleride, is very similar to that of the 'bulk' ammonia (>12Å) which are not solvating the fulleride. There are some differences in the structure between the first shell pair distribution functions and the other two though, and these differences are dependent on the anionic charge.

In the case of C_{60}^{6-}, the solvent molecules form, on average, ~0.84 hydrogen-bonds per molecule to the fulleride. In the case of C_{60}^{2-}, this is reduced to ~0.62. In solution, ammonia forms on average ~2.0 hydrogen-bonds per nitrogen atom.[87,85] Concentrating first on the C_{60}^{6-} anion solution, an increase in the size of the shoulder at about 2.4Å in the $g_{NH}(r)$ in the first shell is indicative of a slight *increase* of the number of hydrogen-bonds between solvent molecules. This is followed, in the same function, by a decrease in the size of the feature at found ~3.5Å which can be attributed to a decrease in non hydrogen-bonded adjacent ammonia molecules.

The $g_{HH}(r)$ function reveals more about the extent of hydrogen-bonding. The feature at 2.9Å, which arises from correlations between adjacent hydrogen-bonds, is the same for the first shell as for the bulk solvent, however the size of the peak at 3.9Å is significantly less in the first shell than the bulk. This peak is attributed to the presence of non hydrogen-bonded, adjacent ammonia, H-H correlations. The reduction of this peak is due to the fact that nearly all of the hydrogen atoms of the ammonia molecules are incorporated into hydrogen-bonds: ~0.84 to the fulleride and ~2.0 to ammonia molecules.

The inter-solvent structure of the solvation shells for the C_{60}^{2-} anion is slightly different. In this case, an examination of the $g_{NH}(r)$ reveals the inter-solvent hydrogen-bonding is reduced slightly within the first shell, compared with the bulk solvent. The decrease in hydrogen-bonding to fulleride in the first shell, compared with the C_{60}^{6-} solution, is confirmed by the existence of the feature at

3.9Å in the $g_{HH}(r)$, attributed to non-hydrogen-bonded ammonia correlations. The feature at 2.9Å in the $g_{HH}(r)$ for the first shell, (from inter-solvent hydrogen-bonded adjacent molecules) is still present, although the intensities of these features are less than in the bulk solvent. In the first shell of the C_{60}^{2-} solution, we have on average 0.62 hydrogen-bonds per ammonia to the fulleride, so although the typical 2.0 hydrogen-bonds are formed within and across the solvent, there are a number of hydrogen atoms that do not form hydrogen-bonds to either the C_{60} or adjacent ammonia molecules.

In conclusion, on average the overall bulk inter-solvent structure is maintained within the fulleride shells, and the ammonia molecules accommodate the fulleride without a large disruption to the inter-solvent structure. Upon an increase in charge, there is a more rigidly bonded inter-solvent structure within the first shell. These results demonstrate how the ammonia molecules accommodate the fullerides using their non-bonded hydrogen atoms to complete hydrogen-bonds to the fullerides whilst maintaining inter-solvent hydrogen-bonds.

6.5.6 Structure of the Potassium Ion in Solution

The structure of the cation in solution is investigated by examining the $g_{KN}(r)$, $g_{KH}(r)$ and $g_{C60\text{-}K}(r)$. Figure 6.13 plots the distribution of nitrogen atoms around a potassium atom. The inset shows the running coordination number. Investigation of the $g_{KH}(r)$ reveals the orientation of the ammonia molecules: they are arranged so that their hydrogen atoms point away from the cation. This is further discussed in the Section 6.6.4, and this solvent arrangement can be seen in Figure 6.16.

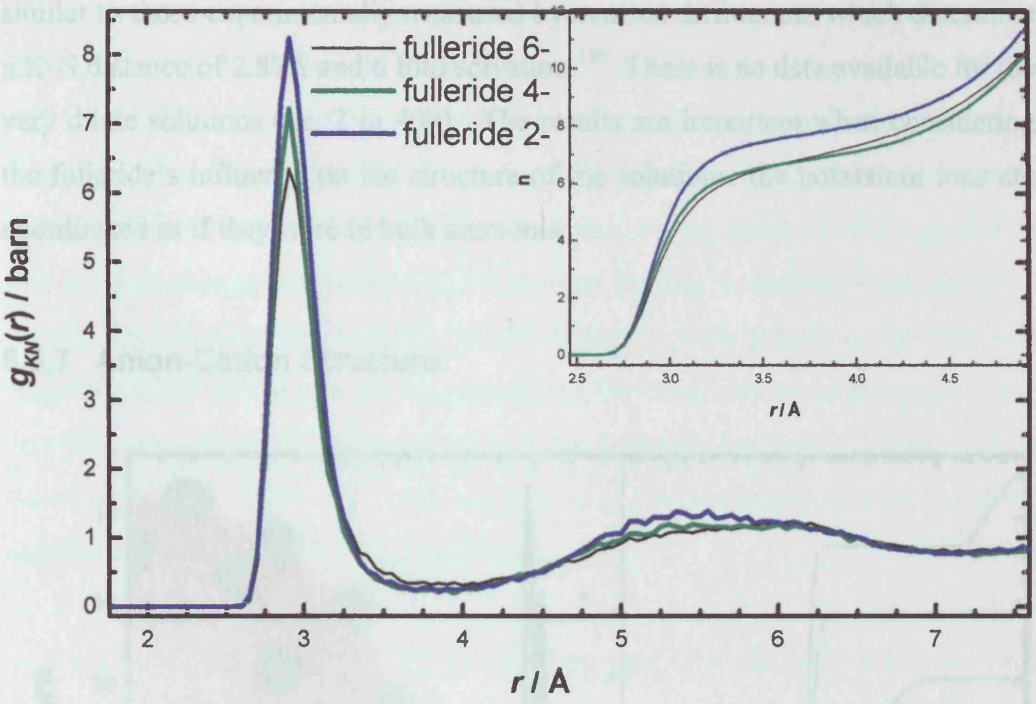

Figure 6.13: Potassium cation solvation structure, $g_{KN}(r)$, for solutions $NH_{3(400)}$, C_{60}^{n-}, nK^+, n = 2 (blue), 4 (green) and 6 (black). The inset shows the running coordination numbers.

In all three cases the cation is strongly solvated by the ammonia molecules. The ammonia directs its electronegative nitrogen atom towards the cation. The average, first shell cation-nitrogen distance is ~2.9Å.

Figure 6.13 reveals that the solvation intensity increases with decreasing concentration of potassium cations in solution. For the systems of 4 and 6 potassium ions, there are ~6.6 ammonia molecules closely solvating them. For 2 ions per fulleride an there is an increased number of ~7.7 ammonia molecules. The increase in coordination number of solvent molecules with decreasing metal concentration is typical of cation solvation in pure metal-ammonia solutions. There is no increase in average potassium-nitrogen distances and the molecules are therefore more tightly packed in the solvation shell for the system containing 2 cations. The results for the solutions containing 4 and 6 potassium ions are very

similar to those experimentally measured by neutron diffraction, which determine a K-N distance of 2.87Å and 6 fold solvation.[148] There is no data available for the very dilute solutions (i.e. 2 in 400). The results are important when considering the fulleride's influence on the structure of the solutions: the potassium ions are coordinated as if they were in bulk ammonia.

6.5.7 Anion-Cation Structure

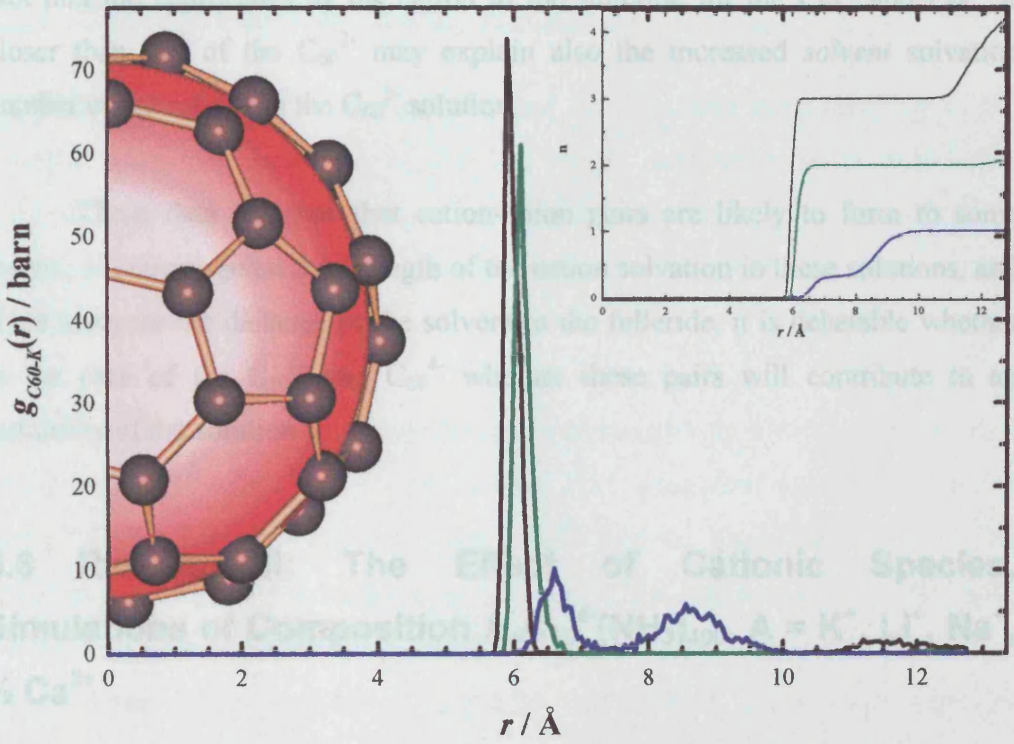

Figure 6.14: Cation–anion structure, $g_{C60\text{-}K}(r)$, for solutions $NH_{3(400)}$, C_{60}^{n-}, nK^+, n = 2 (blue), 4 (green) and 6 (black). The inset shows the running coordination numbers.

Figure 6.14 plots the distribution of potassium atoms around the centre of the fulleride. An examination of the $g_{C60\text{-}K}(r)$s shows that in the three solutions there are some potassium ions closely coordinated to the C_{60} anions. The number of cations closely coordinated to the C_{60} is equal to, or less than, half of those in

the system. The higher the charge on the anion, the closer the approach of the cation. The noise in the data for the $2K^+$-C_{60}^{2-} indicates that the potassium ions are not 'fixed' in this position, although this is not the case in the other two solutions. The closest distance of approach of the cation to the fulleride's centre is 6Å for a C_{60}^{6-} anion which is further than the closest distance of the solvent to this anion (hydrogen-bonds form at 5.83Å from the C_{60}^{6-}s centre). Also, we recall that in this solution, the enthalpy of dissolution is very small, so the fact that roughly half of the cations are coordinated to the fulleride can be expected. The fact that the approaches of the cation to the fulleride for the C_{60}^{4-} and C_{60}^{6-} is closer than that of the C_{60}^{2-} may explain also the increased *solvent* solvation number of the cations in the C_{60}^{2-} solution.

These data suggests that cation-anion pairs are likely to form to some extent. However, given the strength of the cation solvation in these solutions, and if we compare the distance of the solvent to the fulleride, it is debatable whether in the case of the C_{60}^{6-} and C_{60}^{4-} whether these pairs will contribute to an instability of the solution.

6.6 Results III: The Effect of Cationic Species, Simulations of Composition $A_4C_{60}^{4-}(NH_3)_{400}$, A = K^+, Li^+, Na^+, ½ Ca^{2+}

Together with fulleride charge, another major controllable parameter in these solutions is the choice of cation species. There are many metals which dissolve in liquid ammonia releasing their valance electron in solution, including the alkali metals, alkali earth metals, and some lanthanides.[5] Divalent metals have been shown to dissociate two electrons per atom into solution.[129] Within Group 1, different charge densities on the ion result in different solvation coordination numbers and distances, in liquid ammonia. For example, lithium is typically tetrahedrally coordinated[85] and potassium octahedrally coordinated.[148] There are subtle differences in the solubilities of these ions as well as the stabilities of the fulleride salts they form.

This section examines solutions containing the C_{60}^{4-} anion as a function of cation species. The structure of the anion with respect to the solvent, the size of the enthalpy of dissolution, and the nature of the cation solvation and cation-anion pair formation is investigated. Lithium, sodium and potassium are compared from group 1 as well as the divalent calcium which requires only half the number of cations for the reduction of the fulleride.

6.6.1 Crystal Structures Ca_2C_{60}, Na_4C_{60}, Li_4C_{60}, K_4C_{60}

Of these four crystal structures, K_4C_{60} and Na_4C_{60} have been reported in the literature and the structure Li_4C_{60} has been mentioned in a book[7] but crystallographic details were not given, and further reports have not been found in the literature. Ca_2C_{60} has not been reported, and a homogenous crystal did not result from the simulations.

Na_4C_{60} has been experimentally determined to be a bct crystal at high temperatures ($T > 500°C$).[7] Upon cooling this compound has been found to polymerise with the C_{60} molecules connected via four 'single bonds'.[161162] The simulation of Na_4C_{60} here results in a reduction in the *c*-direction, consistent with a bct lattice, and similar to the structure found for the simulation of K_4C_{60}. This shows reasonable agreement to the high temperature phase experimentally measured.[7] The average C_{60}-C_{60} approach is found to be ~9.85 slightly less than in K_4C_{60}, which also concurs with observation (of the high temperature phase).[7] The experimental data was measured for samples formed by the vapour transport technique, and cooling from the elevated temperatures required for this technique results in the polymerisation of the C_{60}s. Perhaps if the crystals were formed using the low temperature liquid ammonia technique, the bct phase would be formed directly and would be stable at room temperature.

The results of the simulation of Li_4C_{60} are also interesting. This system adopts a distinct crystal structure which is different for the other compounds and

is not reported in the literature. Some work has been done on polymerised structure of Li_4C_{60} formed in a similar way to the sodium compound.[163] A stable compound at this composition without any polymerisation, formed using the liquid ammonia technique, has also been mentioned in a book although the lithium positions were not determined.[7] The results are not further reported in the literature. Figure 6.15 shows the structures resulting from the simulation for both Na_4C_{60} and Li_4C_{60}. Both simulations were started from the same positions. One can see the slight shortening of the *c*-direction in Na_4C_{60} crystal, and the rearrangement of the lithium ions in the Li_4C_{60}.

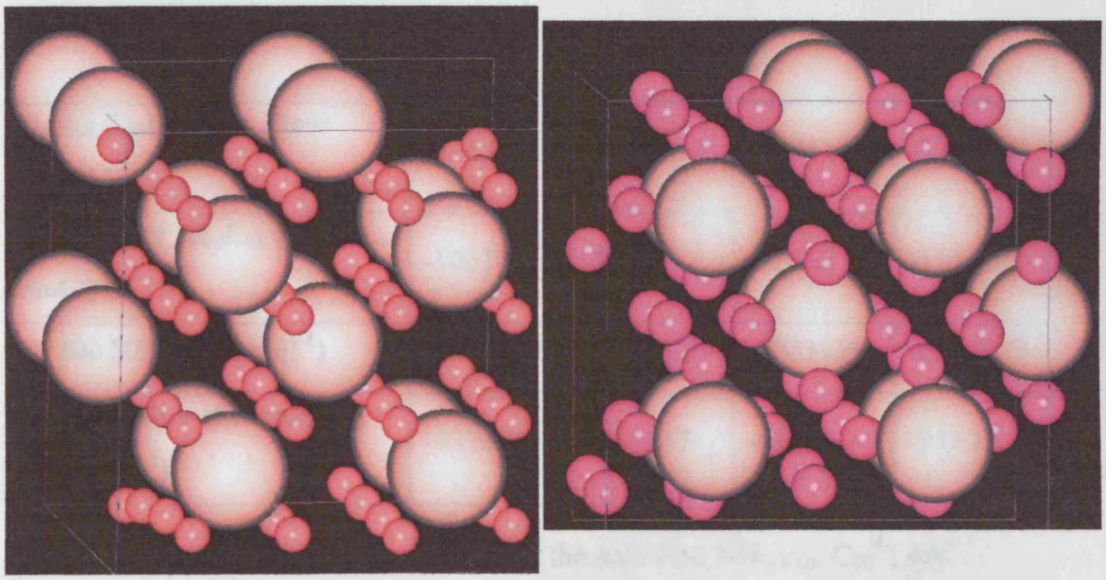

Figure 6.15: Simulation snapshots for the structures Li_4C_{60} (left) and Na_4C_{60} (right). The figures show the entire simulation box.

6.6.2 Enthalpies of Dissolution

The values for the lattice enthalpies, solution enthalpies, and the resulting enthalpies of dissolution are recorded in Table 6.8. These results indicate that all the formation of the solutions is enthalpically favourable with respect to the formation of the salt and pure solvent. The results show that the solutions of lithium and sodium the most stable, and the solution of potassium the least stable. Again caution must be taken in the interpretation of the enthalpy of dissolution results, as the entire phase diagrams of the systems has not been examined. The results are further discussed in the following sections.

	Li	Na	K	Ca
U, $A_{4/2}C_{60}(NH_3)_{400}$ (kcal mol^{-1})	-3183±20	-3113±17	-3006±19	-3236±19
U, 1 unit of $K_{4/2}C_{60}$ (kcal mol^{-1})	-1031±2	-927±5	-923±3	-1120±4
U, 400 NH_3 (kcal mol^{-1})	-2021±20	-2021±20	-2021±20	-2021±20
ΔU Enthalpy of formation (kcal mol^{-1})	-131±28	-155±27	-61±28	-95±28

Table 6.8: Enthalpy of dissolution data for the solutions $NH_{3(400)}$, C_{60}^{4-}, $4A^{+}$

6.6.3 Anion Solvation

The radial distribution functions of the solvent centred on the C_{60} anion are plotted in Figure 6.16.

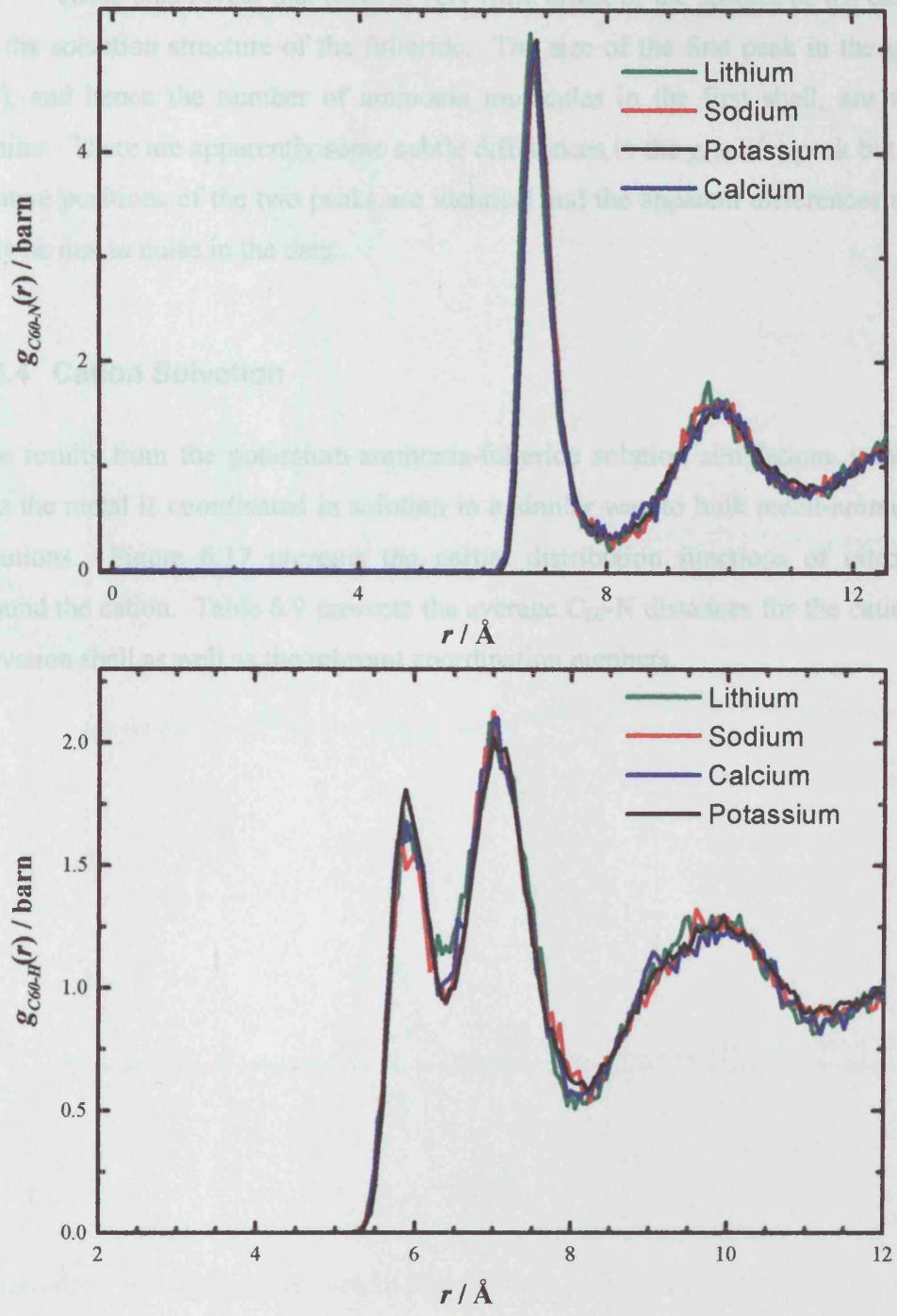

Figure 6.16: $g_{C604-\text{-}H}(r)$ and $gC_{604-\text{-}N}(r)$, distribution function for solutions C_{60}^{4-}, $4A^{+}$, 400 NH_3 where A = potassium (black), sodium (red), lithium (green) and 1/2calcium (blue).

These data reveal that there is very little effect of the species of the cation on the solvation structure of the fulleride. The size of the first peak in the $g_{C60\text{-}N}(r)$, and hence the number of ammonia molecules in the first shell, are very similar. There are apparently some subtle differences in the $g_{C60\text{-}H}(r)$ peak but the relative positions of the two peaks are identical and the apparent differences may only be due to noise in the data.

6.6.4 Cation Solvation

The results from the potassium-ammonia-fulleride solution simulations indicate that the metal is coordinated in solution in a similar way to bulk metal-ammonia solutions. Figure 6.17 presents the partial distribution functions of nitrogen around the cation. Table 6.9 presents the average C_{60}-N distances for the cationic solvation shell as well as the relevant coordination numbers.

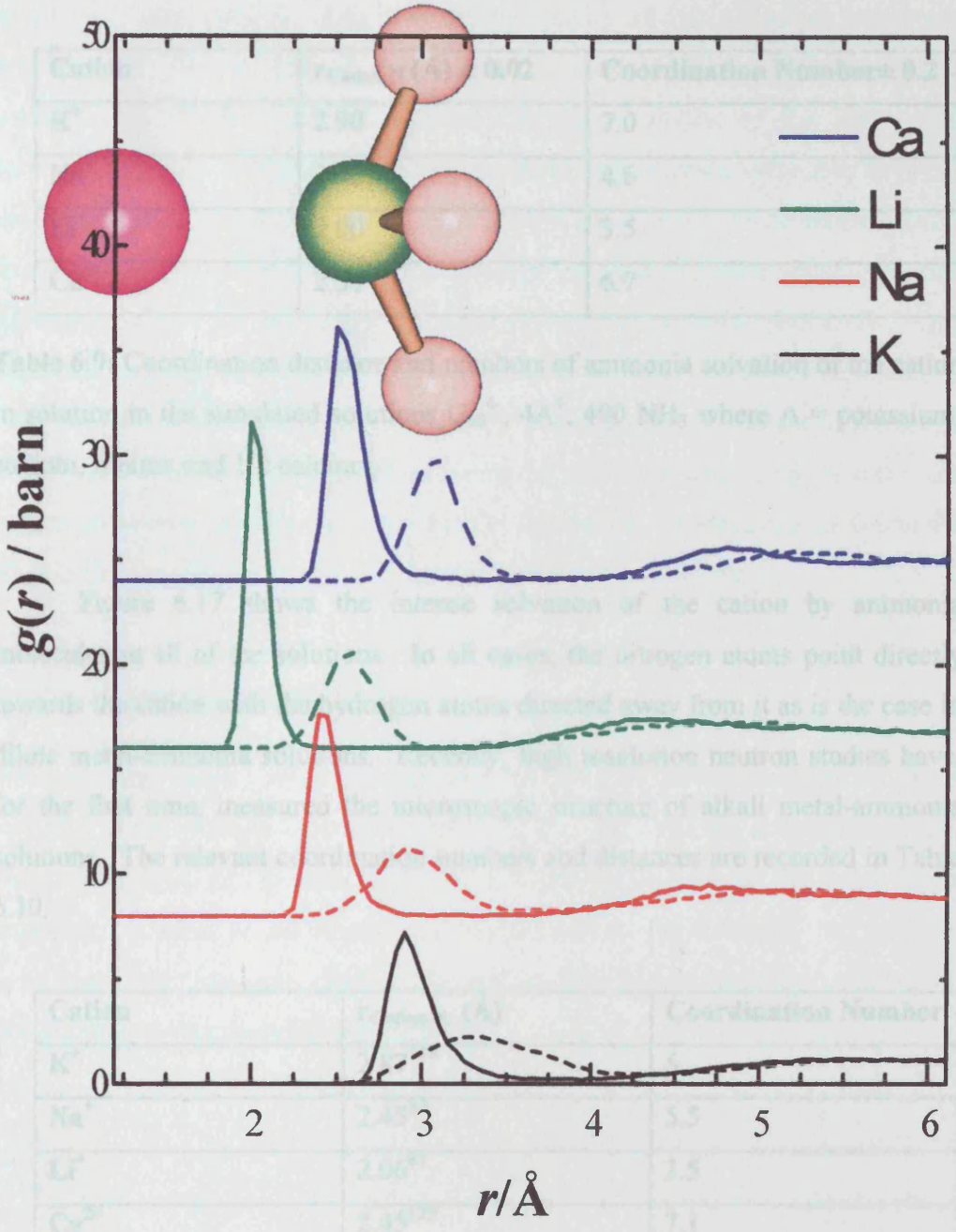

Figure 6.17: Solvation of the cation by ammonia in the solutions C_{60}^{4-}, $4A^{+}$, 400 NH_3 where A = potassium (black), sodium (red), lithium (green) and 1/2calcium (blue). The figure shows both the $g_{AH}(r)$ (dashed) and the $g_{AN}(r)$ (solid). The molecular graphics at the top is a guide to the eye, key: cation – purple, nitrogen – green, hydrogen – white.

Cation	$r_{Cation-N}$ (Å) ± 0.02	Coordination Number± 0.2
K^+	2.90	7.0
Na^+	2.42	4.6
Li^+	2.00	3.5
Ca^{2+}	2.51	6.7

Table 6.9: Coordination distance and numbers of ammonia solvation of the cation in solution in the simulated solutions C_{60}^{4-}, $4A^+$, 400 NH_3 where A = potassium, sodium, lithium and 1/2 calcium.

Figure 6.17 shows the intense solvation of the cation by ammonia molecules in all of the solutions. In all cases, the nitrogen atoms point directly towards the cation with the hydrogen atoms directed away from it as is the case in dilute metal-ammonia solutions. Recently, high resolution neutron studies have, for the first time, measured the microscopic structure of alkali metal-ammonia solutions. The relevant coordination numbers and distances are recorded in Table 6.10.

Cation	$r_{Cation-N}$ (Å)	Coordination Number
K^+	2.87[148]	6
Na^+	2.45[82]	5.5
Li^+	2.06[81]	3.5
Ca^{2+}	2.45[129]	7.1

Table 6.10: Experimentally measured cation coordination distances and numbers in alkali-metal ammonia solutions.

The data in Table 6.10 is very similar to the data obtained for metal-ammonia-fulleride solutions and provides strong evidence that the cations are solvated in the same way in these solutions as they are in metal-ammonia

solutions. This indicates that it is the propensity of this solvation occurring, together with the strength of the fulleride solvation, which allows high ionic concentrations to be achieved without the recombination of the salt. The solvation of both the cation and anion shields the electrostatic attraction between the two species. The overall solution enthalpies are different for different cations in solution. The similarity of the solvation of the fulleride anion means that this difference arises for the differing strengths of the cationic solvation. One difference between the curves which correlates with the solution enthalpies, at least for the monovalent cations, is the width and height of the cation solvation shell. This can also be thought of as due to the charge density of the anions. The higher the charge density, the more tightly defined the coordination shell and the more energetically favourable it is for this coordination to occur.

6.6.5 Cation-C_{60} Correlations

An important factor, when considering the stability to flocculation of these systems, is the strength of recombination of the salt. We get a measure of this from the enthalpy of dissolution. It is also important to examine the cation-anion structure. If most or all cations are coordinated to the fulleride, the fulleride compound may 'salt out'. Partial distribution functions of the cation centred on the fulleride are presented in Figure 6.18.

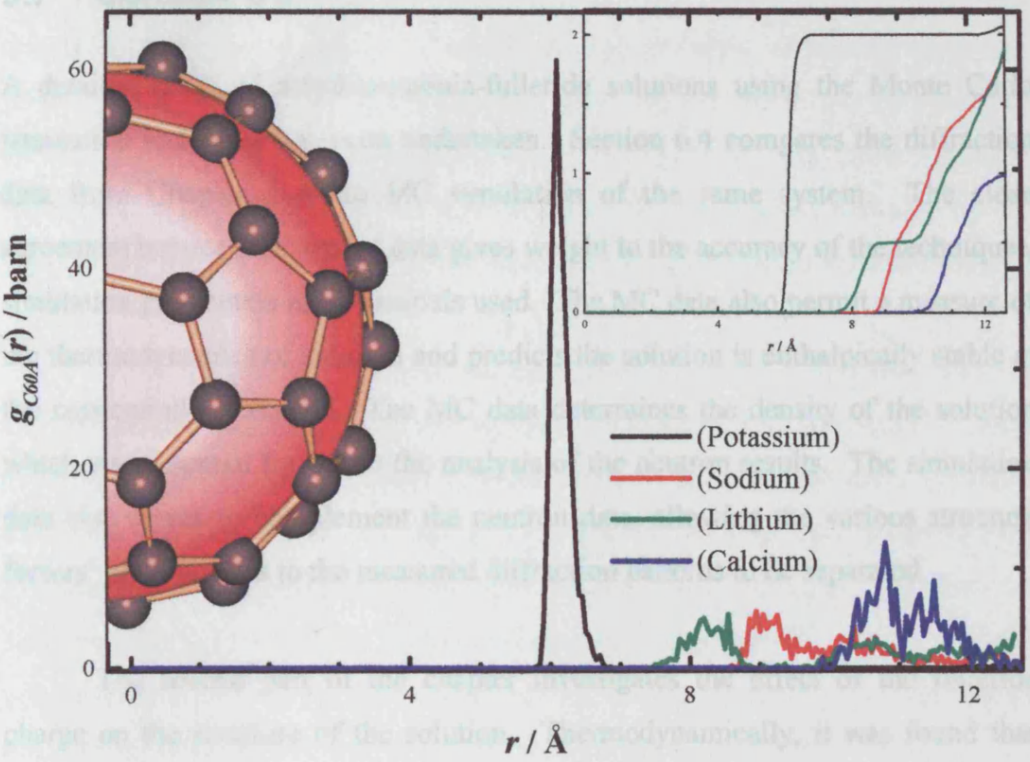

Figure 6.18: Distribution of the cation around C_{60} in the systems: C_{60}^{4-}, $4A^{+}$, 400 NH_3 where n = potassium (black), sodium (red), lithium (green) and 1/2calcium.

Figure 6.18 shows that the potassium ions are more closely coordinated to the C_{60} than any other ion. In fact, the other cations are not found in contact with the anion at all, and indeed, are not within the first ammonia solvation shell of the fulleride. This is reflected in the enthalpy of dissolution, which is much more negative for the sodium-, calcium- and lithium-ammonia-fulleride solutions, than for the potassium-ammonia-fulleride solution. Examining the solution enthalpy of the four different systems, we can see an approximate correlation between this and the distance of cation-anion approach. The reduction in the potassium-ammonia-fulleride solution enthalpy may be due to the fact that the close approach of the potassium to the fulleride reduces the individual solution enthalpy of both the cation and the fulleride.

6.7 Conclusion

A detailed study of metal-ammonia-fulleride solutions using the Monte Carlo simulation technique has been undertaken. Section 6.4 compares the diffraction data from Chapter 5 to an MC simulation of the same system. The close agreement between the sets of data gives weight to the accuracy of the techniques, simulation parameters and potentials used. The MC data also permit a measure of the thermodynamics of solution and predicts the solution is enthalpically stable at the concentrations studied. The MC data determines the density of the solution which was essential for use in the analysis of the neutron results. The simulation data also serves to complement the neutron data, allowing the various structure factors' contributions to the measured diffraction patterns to be separated.

The second part of the chapter investigates the effect of the fulleride charge on the structure of the solution. Thermodynamically, it was found that although the solution enthalpy increased with increasing fulleride charge, this was more than offset by an increase in lattice enthalpy with fulleride charge. This led to the prediction that the K_6C_{60} would be less enthalpically stable than the other solutions, and explains, to some extent, why the C_{60}^{6-} anion was not seen in rubidium-ammonia-fulleride solutions.[6] The thermodynamic analysis also correctly predicts that the C_{60} fullerite crystal itself does not dissolve.

The simulations of the crystal structures for K_4C_{60} and K_6C_{60} result in structures similar to experimental measurements on these compounds, suggesting that classical MC is a useful method for studying the structures of these salts. The lattice enthalpy predicted by the simulated pure fullerite crystal shows close agreement the enthalpy of sublimation measured experimentally.

The accommodation of the fulleride in the ammonia solvent can be attributed to a network of hydrogen-bonding. Two well defined solvation shells form around the C_{60} anions in solution with hydrogen-bonds forming to the fullerides. The 'strength' of these bonds is dependent on the charge on the anion: the higher the charge the shorter the hydrogen-bond length and the larger the

number of bonds per ammonia molecule. The fact that C_{60} itself does not dissolve in ammonia is consistent with its small solution enthalpy. Although there is a solvent reorganisation around the C_{60} molecules, the first shell hydrogen-bond to the C_{60} is not seen for the neutral molecule. The H-bond only forms when the fullerene is charged. This means that the relatively small lattice enthalpy for the C_{60} crystals is not overcome when the molecules are coordinated with ammonia.

As the fulleride is charged, the number of hydrogen atoms per molecule approaches one. A value of one hydrogen-bond per ammonia molecule allows the overall hydrogen-bonding between ammonia molecules within the solvation shells to remain the same as in bulk ammonia. The simulations have permitted the examination of this intra-shell hydrogen-bonding in more detail. Within the solvation shells, inter-solvent hydrogen-bonding is maintained. In this way, the unique structure of the ammonia molecule allows the remaining hydrogen atom, not bonded within the solvent, to complete a hydrogen-bond to the fulleride.

Investigations into the solvation of the potassium cations in the solutions show that the cations are solvated in a very similar way as in bulk metal-ammonia solutions. There is evidence for cation-anion pairs, however, and the extent of these depends on the charge on the anion. However, there is never more than half the number of potassium ions in the system coordinated to the fulleride, nor are the potassium-fulleride distances less than the closest approach of the ammonia molecule to the fulleride.

The final part of this chapter is the investigation of the effect of the species of metal cation on the structure of the solutions. The enthalpy of dissolution for sodium, calcium and lithium–ammonia-fulleride solutions is greater in magnitude than that of the potassium-ammonia-fulleride solutions. This is reflected by the fact that, unlike the potassium system, there are no cation-fulleride contacts seen for the other ions. The actual solvation structure of the fulleride anion is independent of cationic species. The structure of the cation solvation is extremely close to that experimentally measured in recent work for the pure metal-ammonia

solutions. This again supports the conclusion that the cations and fulleride anions are independently and strongly solvated by the ammonia molecules.

Chapter 7

Results III: Nuclear Magnetic Resonance

7.1 Introduction

An application of metal-ammonia-fulleride solutions is as an arena in which to study the fundamental properties of discrete C_{60} anions using solution techniques. These solutions offer a unique possibility for such measurements due to the high concentrations of fullerides attainable, together with the controllability of the charge on the anion. Relatively weak intramolecular contacts in the fulleride compounds have led to the suggestion that studying isolated fullerides is the preferred point of departure for understanding the topical A_xC_{60} salts.[3] This chapter presents the preliminary results of ^{13}C NMR studies of the anions, and confirms the scientific importance of metal-ammonia-fulleride solutions.

NMR provides a measure of the magnetic interaction of a magnetic nucleus with its local electronic environment. When a magnetic nucleus is placed

in magnetic field, it adopts one of a number of allowed orientations of different energies. By applying electromagnetic radiation at the right frequency, it is possible to cause the nucleus to 'flip' between these orientations, if the energy of the photon is the same as the energy gap between orientations. This frequency is called the resonance frequency and is sensitively dependent on the electronic environment of the nucleus. The change in frequency with different electronic environments is measured in terms of a chemical 'shift' between the resonance frequencies of the nucleus of interest (ν), and a reference nucleus (ν_{ref}), by means of a dimensionless parameter, δ:

$$\delta = 10^6 \frac{(\nu - \nu_{ref})}{\nu_{ref}}. \qquad 7.1$$

NMR has been identified as a useful tool in advancing the understanding of the electronic and structural behaviour of fullerenes and fullerides. A comprehensive review of the previous work on solid state NMR of fullerides is available.[164] The small amount of existing solution NMR measurements on the anions is reviewed in a section in a recent review article.[3] ^{13}C NMR measurements of C_{60} were crucial in the early confirmation of the icosahedral structure of C_{60} proposed by Kroto.[165] A single, sharp peak in the NMR spectrum of C_{60} in solution confirmed the equivalence of the 60 carbon atoms, and hence the C_{60}'s spherical geometry. Similarly, the five lines in the ^{13}C NMR spectrum of C_{70} helped establish its structure.[166]

The low quality of the existing data for anions in solution is attributed to the low concentrations, and the instability of the fullerides, in most solutions. Although ^{13}C enriched C_{60} is obtainable, the maximum percentage of ^{13}C is only ~20% and it is very expensive. Natural C_{60} containing ~1.01% ^{13}C is therefore used. To get round the poor concentrations in solution, experimenters have used high-sensitivity instrumentation and extremely long acquisition times. The reactivity of the C_{60} anions with air and oxygen is cited as another hindrance in the attainment of good data.[3] The ^{13}C signal size has so far have been very

small.[116] The measurement shown in Figure 7.1 was the result of 34196 scans! The chemical shift of the C_{60}^{5-} anion has not yet been recorded.

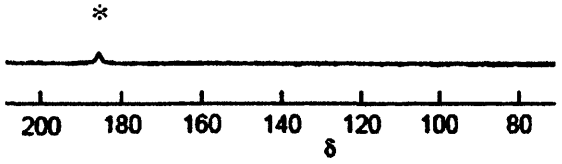

Figure 7.1: The ^{13}C NMR spectra of C_{60}^{4-} reproduced from reference [116].

This chapter presents the ^{13}C NMR spectra for the fulleride anions n = 1 to 5, in potassium-ammonia-fulleride solutions. The results are recently obtained and the implication of the relative positions of the anions' shifts, on their magnetic and electronic properties, is beyond the scope of this thesis, and will not be discussed. Conclusions reflecting the structural properties of the metal-ammonia-fulleride solutions will be made.

7.2 Experimental

The solutions were made and sealed in 5mm diameter high quality, quartz NMR tubes as described in Chapter 3. The measurements were made using a Varian Unity-Plus 500 NMR spectrometer. A pulse delay of 1 second was used. The anions, dissolved in potassium-ammonia solutions were made to typical compositions of $K_nC_{60}(NH_3)_{350}$, and were measured at a temperature of ~223K. The data presented here typically consists of about 200-300 scans. The shifts are referenced externally to TMS at 0ppm.

7.3 Results

The ^{13}C NMR spectra for the fulleride anions, C_{60}^{n-}, where n = 1 to 5 are plotted in Figure 7.2.

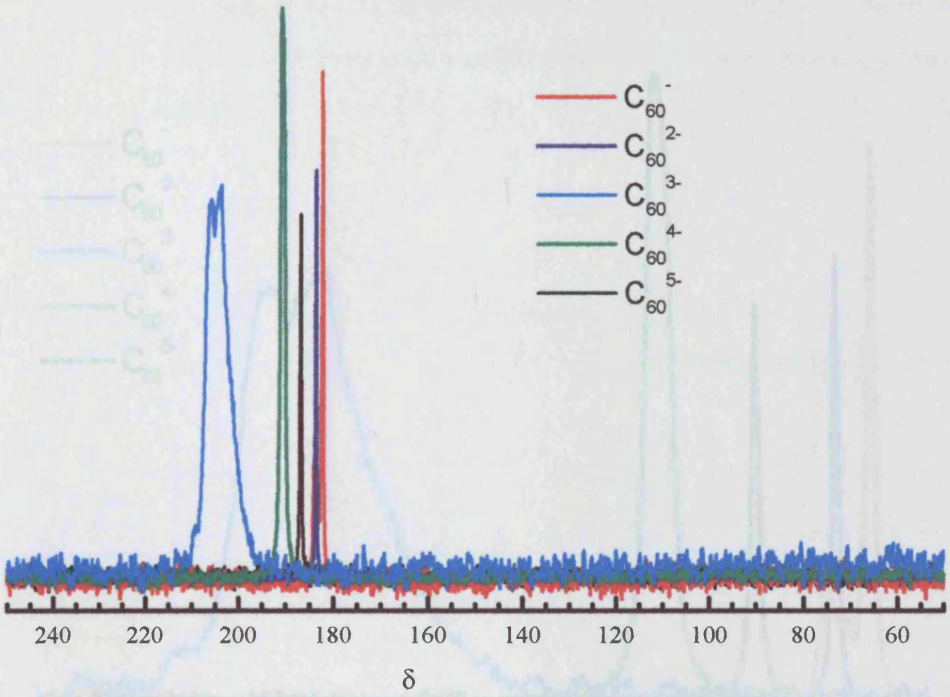

Figure 7.2: ^{13}C NMR spectra for the fulleride anions C_{60}^{n-} where n = 1 to 5, measured in potassium-ammonia-fulleride solutions.

The results presented in Figure 7.2 demonstrate that excellent ^{13}C NMR data on the discrete fulleride anions is possible using metal-ammonia-fulleride solutions. The sizes of the peaks obtained in relatively short counting times are much larger and sharper than any previous measurements. This is due to the high concentrations of fulleride anions that these solutions can accommodate, and the stability of the anions in these solutions. The results show single, sharp, distinct peaks for the fulleride anions C_{60}^{-}, C_{60}^{2-}, C_{60}^{4-} and C_{60}^{5-} indicating the identical environment of all the carbon atoms in these anions. The C_{60}^{3-} does have a significant width. This ion leads to metallic compounds and superconductivity in the solid state, and can perhaps be considered the most interesting of the fulleride anions. This fact is reflected in the non-conformity of its ^{13}C spectrum. The increased width and position is consistent with previous measurements as well as solid state measurements.[3,164] To examine the spectra in more detail, Figure 7.3 shows an enlargement of Figure 7.2.

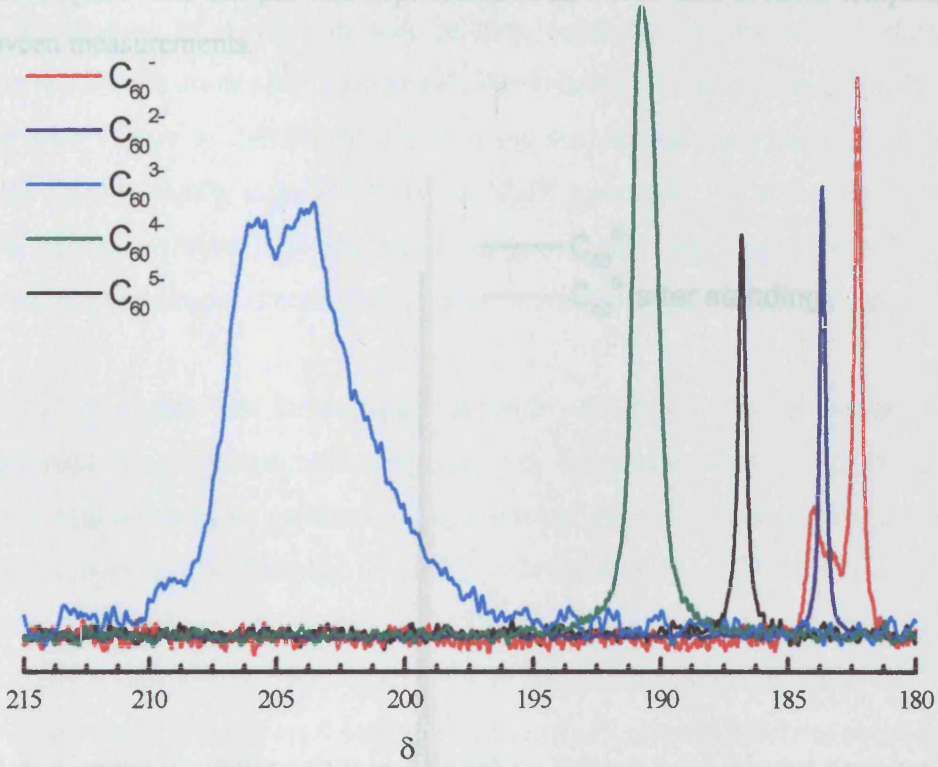

Figure 7.3: ^{13}C NMR spectra for the fulleride anions C_{60}^{n-} where n = 1 to 5, measured in potassium-ammonia-fulleride solutions.

Figure 7.3 confirms the narrow line widths of all the ^{13}C peaks, with the exception of the C_{60}^{3-} anion. The data also shows that the C_{60}^{-} anion spectra has two peaks. Examining the experimental records reveals that this sample had a slight excess of potassium. The smaller peak can be then be attributed to a population of C_{60}^{2-} anions in this solution. This contrasts with previous measurements made on the anions in solution, in which intermediate concentrations of ions, produced averaged peak positions.[3,116] This led to the conclusion that electron transfer on the NMR timescale was evident. This is not the case in metal-ammonia-fulleride solutions, and confirms the sequential nature of the reduction and the stability of the individual anions in these solutions.

Figure 7.4 plots two ^{13}C spectra for the same sample (C_{60}^{5-}) taken three months apart. The sample was kept sealed in an NMR tube at room temperature between measurements.

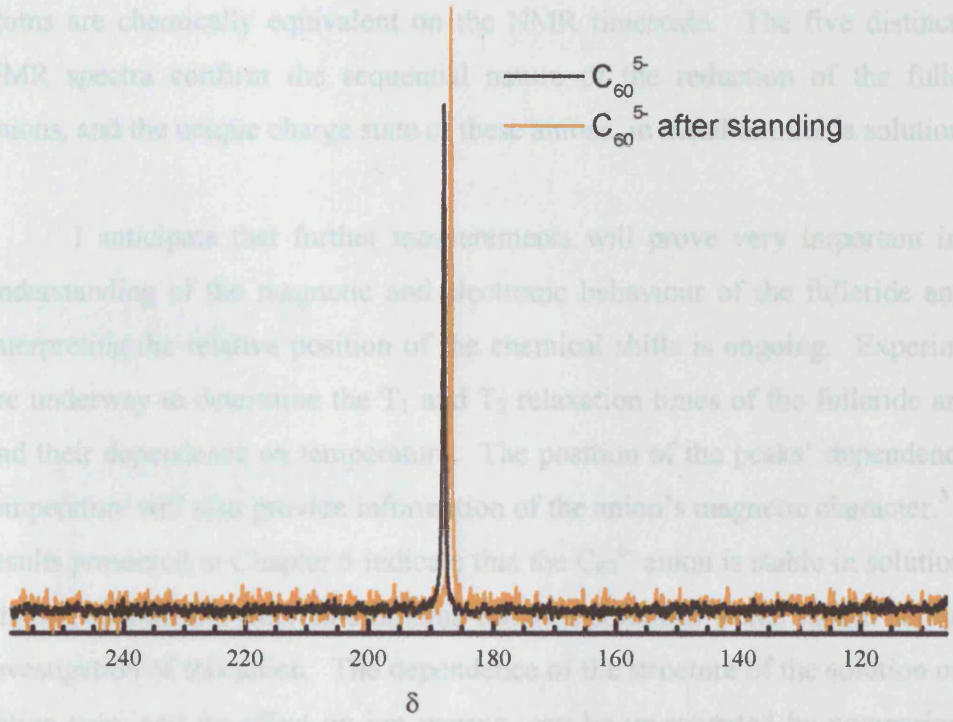

Figure 7.4: The ^{13}C NMR spectra for C_{60}^{5-} anion in potassium-ammonia-fulleride solutions. The two data-sets are from the same sample and are taken 3 months apart. The sample was kept at room temperature (under pressure in the sealed NMR tube) between measurements.

The slight variation of this shift is within the error of the instrument. This result is significant as it shows that there is no decomposition of the fulleride anions even at room temperature. Once the electrons are picked up by the fulleride, and if oxygen and water are isolated from the system, metal-ammonia-fulleride solutions are stable.

7.4 Conclusions

The application of metal-ammonia-fulleride solutions for use in the study of discrete fulleride anions has been clearly demonstrated. The results show that the electronic charge is distributed evenly over the fulleride anions. The carbon atoms are chemically equivalent on the NMR timescale. The five distinct ^{13}C NMR spectra confirm the sequential nature of the reduction of the fulleride anions, and the unique charge state of these anions, in metal-ammonia solutions.

I anticipate that further measurements will prove very important in the understanding of the magnetic and electronic behaviour of the fulleride anions. Interpreting the relative position of the chemical shifts is ongoing. Experiments are underway to determine the T_1 and T_2 relaxation times of the fulleride anions and their dependence on temperature. The position of the peaks' dependence on temperature will also provide information of the anion's magnetic character.[3] The results presented in Chapter 6 indicate that the C_{60}^{6-} anion is stable in solutions of lithium, sodium and calcium-ammonia-fulleride solutions which should permit the investigation of this anion. The dependence of the structure of the solution on the cation type, and its effect on ion pairing, can be investigated by comparing the values of the NMR shifts from solutions containing different metals.

Chapter 8

Conclusions

8.1 Introduction

This project forms the first concerted effort to study metal-ammonia-fulleride solutions. Atomistic techniques have been used to determine the structure of these novel solutions. Experiments and simulations have permitted an exploration of the intricate hydrogen-bonding arrangement developed in these liquids, and its dependence on fulleride charge and cation type. Metal-ammonia-fulleride solutions show great promise as a medium in which to study the fulleride anions, and for use in the manipulation of fullerides.

This project builds upon the experimental work of one previous publication, which proves the reversible, sequential reduction of fullerene C_{60} in metal-ammonia solutions.[6] Surprisingly, since this paper, there had been no further investigation into metal-ammonia-fulleride solutions. This is perhaps due to the immediate difficulty in making and containing the solutions for experimental measurements, which requires high integrity vacuum systems, inert

atmosphere manipulation and low temperatures. However, once these difficulties are overcome, the solutions have been shown here to be rich in scientific interest. Measurements of the ^{13}C NMR spectra for the anions C_{60}^{n-} (n = 1 to 5), afforded by these solutions, will play a vital role in understanding the electronic and magnetic character of fulleride anions and hence fulleride compounds. This work contains the first detailed structural measurements of pure carbon in solution. Understanding carbon solvation is extremely important, and these solutions present the possibility of the manipulation of carbon nanoparticles in solution, via the charge state. This is important in the future of processing and isolating new carbon based materials. This chapter states the main conclusions from this work on the structure of the solutions. Ideas and directions for further work are also discussed.

8.2 The Structure of Alkali Metal-Ammonia-Fulleride Solutions

The overall model of the solutions developed from these studies is that metal-ammonia-fulleride solutions contain both strongly solvated fulleride anions and strongly solvated metal cations. It is the strength of this solvation that maintains the separation of the ions, and prevents the recombination of the salt. The detailed structure is dependent both on anion charge and cation species.

8.2.1 Fulleride Solvation and Hydrogen-Bonding

The accommodation of the fullerides in these solutions arises from a network of hydrogen-bonds. Results from both neutron diffraction experiments and Monte Carlo simulations clearly show two dense, ordered solvation shells around the anions in solution. In the first shell, the ammonia molecules form hydrogen-bonds to the fulleride. This shell typically contains about 40 ammonia molecules arranged so that ~1 of their hydrogen atoms points towards the centre of the fulleride. The hydrogen atoms move closely to the 5 and 6 memebered carbon rings by pointing towards the centre of the rings, rather than towards individual

carbon atoms. The second shell ammonia molecules maintain this overall directionality, forming hydrogen-bonds to the first shell, although the density and ordering is less intense than the first.

The driving force of the arrangement of one hydrogen-bond per ammonia to the fulleride is that it permits hydrogen-bonding between the solvating ammonia molecules. The inter-solvent arrangement is found to be very similar to that found in bulk liquid ammonia. This ability to complete hydrogen-bonds within the shells as well as to the fulleride is perhaps due to the structure of the ammonia molecule: there are three possible hydrogen-bonds per ammonia molecule.

8.2.2 Cation Solvation

Both neutron diffraction and MC results show that the metal cation is also solvated by the ammonia molecules. In these solvation shells, the nitrogen atoms of the ammonia molecules point towards the cation. This arrangement is identical to that found in metal-ammonia solutions. In fact, the actual values of the solvent distances and coordination numbers of the cations in the fulleride solutions, is found to be very similar to those measured in the analogous metal-ammonia solutions.

Cation-anion pairs do form, to some extent, in solution. However, the cation does not approach the fulleride closer than the average distance of the hydrogen-bond of the ammonia to the fulleride. The number of cations coordinated to the fulleride anion was never found to be more than half the total number of cations per fulleride anion. If the charge density on the cation is more than potassium (i.e. sodium, lithium and calcium), no evidence for pairing is found (see section 8.2.5).

8.2.3 Inter-Fulleride Structure

Attempts to investigate the long range inter-fulleride structure using SANS proved in to be vain, although insightful. The small size of the C_{60} molecule means it is at the bottom end of the SANS regime and no SANS scattering was evident. However, the lack of scattering at low-Q provides strong evidence for the lack of large aggregates in solution. An atomistic computer simulation, large enough to adequately investigate the inter-fulleride structure, was not possible due to current limits on computing processing power and memory capacity. The ordering of the fullerides is on an intermediate range length scale, and neither SANS nor wide angle diffraction are completely suitable for its investigation. This highlights the need for the next generation of diffraction instruments to bridge the gap between SANS and atomistic diffraction. Long standing problems, which are dominated by solvent forces, such as the nature of protein folding, will be possible to study *in situ* as well as ordering processes on the nanoscale, such as self assembly from solution.

8.2.4 Dependence of the Structure on Fulleride Charge

The structure of the solutions is dependent on the charge on the fulleride. The length of the hydrogen-bond to the fulleride in the first solvation shell increases with decreasing charge, whilst the number of hydrogen-bonds per ammonia molecule decreases. The volume of the solvation shells also increases with decreasing charge, although in all cases, the shells are found to contain approximately the same number of ammonia molecules. The density decreases accordingly with decreasing charge.

The magnitude of the solution enthalpy increases significantly with increasing charge on the fulleride anion, to some extent explaining the sequential nature of the reduction. However, the strength of the crystal lattice enthalpy of the dissolved salt increases at a faster rate per unit increase of charge. This leads to the prediction that the C_{60}^{6-} is much less soluble than the other ions at the concentrations simulated, in the potassium-ammonia-fulleride solutions. To some

extent this explains why that in rubidium-ammonia this ion is not seen.[6] A calculation of the enthalpy of dissolution also correctly predicts that pure fullerite crystal does not dissolve in liquid ammonia. This can be linked to an absence of a hydrogen-bond formed to the C_{60} in the first shell. The carbons have to be charged in order for the hydrogen-bonds to form and the fulleride dissolve.

8.2.5 Dependence of the Structure on Metal Species

The effect of changing the cation species on the fulleride solvation structure is minimal. However, the stability of the solution does depend on the cation type. Cation-anion pairs are not evident at all in the solutions which contain cations with a higher charge density than potassium, i.e. lithium, sodium and calcium. In these cases, the solvation shells of the cations contain less solvent molecules, as well as shorter cation-nitrogen distances, indicating a tighter solvent packing. The actual magnitude of the enthalpy of dissolution depends on the lattice enthalpy of the dissolved salt. The results indicate that solutions of the higher charge density cations, such as lithium and calcium, are likely to be more stable and will form more concentrated solutions. The solvation structure of the cations in solution agrees very closely with the experimentally determined values of metal-ammonia solutions in all cases.

8.3 The Electronic Nature of the Anions in Solution

An important application of metal-ammonia-fulleride solutions is for use in the fundamental study of the isolated fulleride species. The controllability of the ion and the high concentrations of fullerides in solution offer a unique opportunity. This is demonstrated by the presentation of the five ^{13}C NMR spectra of C_{60}^{n-}, n = 1 to 5. The data will allow a wide range of NMR measurements to be made in order to characterise the anions. The single narrow line widths in the ^{13}C NMR spectra show the chemical equivalence of the carbon atoms in the anions. The results also confirm the presence of high concentrations of one type of anion in these solutions.

8.4 Further Work

There is a wealth of further relevant work that should be completed in order to answer some important key questions about the fullerenes and their properties. The work will further clarify the nature of solvation of the fullerides and carbon derivatives by ammonia, which may prove very important in the future processing and study of carbon nanoparticles.

8.4.1 Simulations

The close agreement between simulation and experiment demonstrates the ability of the potentials and methods used to describe the real solutions. The simulations are therefore an ideal tool for further exploration of these systems. The charge effect can be quantified by filling in the measurements as well as investigating all the anions as a function of cation type. The effect of fulleride concentration on the structure of the solution should also be investigated. This is important in developing the understanding of the enthalpic stability of these solutions. It is possible that salts of ammonia coordinated cations may be more stable than dispersed solutions, particularly for the divalent ions. The simulation studies should be extended to other carbon nanoparticles dissolved in metal-ammonia solutions. The intense coordination of the fullerides suggests that their rotation will be hindered in solution. Molecular Dynamic simulations would allow the extraction of the relevant diffusion constants. *Ab initio* quantum MD simulations will allow the effect of the ammonia solvent on the electronic distribution on the fulleride anions to be investigated.

Simulations of the pure metal-ammonia solutions using the same input potentials and methods would help in the understanding of the ammonia coordination of the ions, and the enthalpy contribution from that solvation. Fulleride salts have received much attention following the discovery of the superconducting K_3C_{60}. Beyond initial calculations, however, classical simulations have not been used to develop the understanding of their structure. The simulation results in this thesis provide a close description of the structure of

the salts. Simulations could be used to understand the positions of the ammonia molecules in the ammoniated salts, for example. Simulations would permit a systematic search for new stable fulleride salts.

An investigation of the form of the empirical potential in EPSR refinement would be very interesting. The EPSR potential established from a diffraction measurement for water at ambient conditions was then used to simulate the structure of water at higher temperatures and pressures. The EPSR modified potential succeeded in recreating features in the data where the (original) reference SCP/E potential failed. The success of the modified potential is thought to be due to an account of a polarisabilty term, absent from the SCP/E potential.[138] The EPSR modified fulleride potentials used in this work may thus be useful in future simulations of fullerides.

The simulations should be also be 'coarse grained' to permit the investigation of the longer range order. This could be done by using the Girifalco's C_{60} potential,[154] to simulate larger systems.

8.4.2 Experiments

Neutron diffraction on GEM at RAL. The introduction of small amounts of ammonia to alkali metal-fulleride salts results in the solvation of both the metal cation and the fulleride anion (see Section 1.8.1). It would be interesting to examine the effect of continuously adding ammonia to the fulleride salt. Would the ammonia continue solvating the ions? At what point would the fulleride dissolve? An experiment will be undertaken on GEM at the ISIS facility. GEM is a wide angle diffractometer with a large angular coverage and hence Q-range. It is used for both crystallography and the study of disordered materials. The low angle banks, recently made available, provide a low-Q limit of ~0.1Å^{-1} and may reveal inter-fulleride correlations. This experiment will link the study of the fulleride solids to the fulleride solutions, and examine the evolution of the fulleride solvation shells.

Extended X-ray Absorption Spectroscopy. EXAFS permits the investigation of the local environment of a specific element in a system, even if that element is relatively dilute. An experiment on rubidium-fulleride-ammonia solutions has been performed on BM29 at the ESRF and the analysis is ongoing. Preliminary results indicate that, starting with the rubidium fulleride salts, the rubidium EXAFS signal changes upon the introduction of ammonia until a certain concentration above which the signal does not change. The study will measure the extent to which the fullerides are coordinated to the rubidium.

Conductivity. The high ionic concentration of metal-ammonia-fulleride solutions implies a high conductivity. This should be measured directly by 4 point conductivity. A suitable conductivity cell has been custom built. Conductivity experiments will also establish the limiting concentration of the fulleride anions. The conductivity will increase, with increasing concentration, until a point at which the addition of the salt does not result in an increase of charge carriers in solution.

Infra-red spectroscopy. The IR spectrum gives an effective 'fingerprint' of the fulleride anions.[6] IR spectroscopy can therefore be used to confirm the presence of a particular anion, in solution, before and after another measurement. This confirmation would add scientific weight to that measurement. Ideally, the same solution could then be used in several different complementary measurements permitting an unambiguous interpretation of the data.

Deposition of thin films. The solutions have been shown to contain monodisperse fullerides and, as such, are suitable mediums for the technique of colloidal deposition from solution. Simple drop coating experiments as well as a more controlled removal of the solvent will perhaps yield ordered films. Using an electric field, it may be possible to control the deposition from the solution. The resulting films structure can be examined using AFM, STM, and SEM.

Investigation into the separation of fullerenes using metal-ammonia-fulleride solutions. The work here shows that the solutions contain monodisperse anions with a control over the electronic structure of the fullerides. Stability of the solutions, in terms of recombination of the salt, is finely balanced. If there is no charge per carbon atom, there is no dissolution. If there is more than ~$6/60^{th}$ per carbon the solution is likely to salt out. The understanding of the solutions may prove important in developing future processes for the separation of fullerenes. If one placed a mixture of two different fullerenes in metal-ammonia solutions, then the fullerene with the higher electron affinity would be preferentially reduced, and hence preferentially dissolve. If the charge per carbon atom was kept low, then a stable solution of this particle should result. This would permit removal and hence separation. Simple initial experiments can take a mixture of C_{60} and C_{70} and examine the ability of the solution to selectively dissolve the particles based on their electronic structure.

Study of the anions. To complement the NMR measurements, several other solution based techniques designed to examine the intrinsic properties of the anions are possible using metal-ammonia-fulleride solutions. Detailed magnetic measurements can be made using sensitive devices such as a Superconducting Quantum Interference Device (SQUID) and are possible if the solutions can be quenched into a glassy state. In solution, Electron Spin Resonance (ESR) measurements should be made.

New systems. Similar solutions using higher amines than ammonia should be investigated. Higher amines have higher boiling points perhaps permitting room temperature manipulation of the fulleride anions. Using methylamine as a solvent, an initial MC simulation shows an interesting competition between the amine and methyl groups in the solvation of the fulleride. The solution based measurements on the fulleride anions should be extended to ions of other new carbon allotropes.

References:

[1]Ruoff, R. S., Malhotra, R., Huestis, D. L., Tse, D. S. & Lorents, D. C. *Nature* **(1993)**, *352*, 140.

[2] Bezmel'nitsyn, V. N., Eletskiĭ, A. V. & Okun', M. V. *Phys.- Uspekhi.*, **(1998)**, *14(11)*, 1091.

[3] Reed, C. A., & Bolskar, R. D. *Chem. Rev.* **(2000)**, *100*, 1075.

[4] Tasis, D., *et al. Chem. Eur. J.* **(2003)**, *9*, 4000.

[5] Thompson, J. C. Electrons in Liquid Ammonia (Clarendon, Oxford 1976).

[6] Fullagar, W. K., Gentle, I. R., Heath, G. A. & White, J. W. *J. Chem. Soc. Chem. Commun.* **(1993)**, *6*, 525.

[7] Andreoni, W. The physics of Fullerene-based and fullerene related materials (Kluwer Academic Publishers, Dordrecht, 2000).

[8] Buffinger, D. R., Ziebarth R. P., Stenger V. A., Recchia, C. & Pennington, C. H. *J. Am. Chem. Soc.* **(1993)**, *115*, 9267.

[9] Forró, L. & Mihály, L. *Rep. Prog. Phys.* **(2001)**, *64*, 649.

[10] Kroto, H. W., Heath, J. R., O'Brien, S. C. & Smalley, R. E. *Nature* **(1985)**, *318*, 162.

[11] Kadish, K. M. & Ruoff, R. S. Fullerenes Chemistry Physics and Technology, (Wiley-Interscience, New York, 2000).

[12] Dresselhaus, M. S., Dresselhaus G., Eklaud, P. C. Science of Fullerenes and Carbon Nanotubes (Academic Press: San Diego, CA, 1996).

[13] Kroto, H. W. *Angew. Chem. Int. Ed. Eng.* **(1997)**, *36*, 1579.

[14] Krätschmer, W., Lowell, D. L., Fostiropoulos, K., Huffman, D. R. *Nature* **(1990)**, *347*, 354.

[15] Tycko, R. *et al. Phys. Rev. Lett.* **(1991)**, *67*, 1886.

[16] David, W. I. F., Ibberson, R. M., Dennis, T. J. S., Hare, J. P. & Prassides, K. *Europhys. Lett.* **(1992)**, *18*, 225.

[17] Heiney, P. A., *et al. Phys. Rev. Lett.* **(1991)**, *66*, 2911.

[18] Heiney, P. A., *J. Phys. Chem. Solids* **(1992)**, *53*, 1334.

[19] Stephens *et al.*, *Nature* **(1991)**, *351*, 632.

[20] Wang, X. B., Ding, C. F. & Wang, L. S. *J. Chem. Phys.* **(1999)**, *110*, 8217.

[21] Haddon, R. C., Brus, L. E., Raghavachari, K., *Chem. Phys. Lett.* **(1986)**, *125*, 459.

[22] Erwin, S. C., Buckminsterfullerenes, (ed. Billups, W., E., Ciufolini, M., A., VCH, New York).

[23] Satpathy, S. *et al. Phys. Rev. B.* **(1992)**, *46*, 1773.

[24] Xie, Q., Pérez-Cordero, E. & Echegoyen, L. *J. Am. Chem. Soc.* **(1992)**, *114*, 3978.

[25] Green, W. H. *et al. J. Phys Chem.* **(1996)**, *100*, 14892.

[26] Fowler, P. & Manolopoulous, D. E., (An Atlas of Fullerenes, Clarendon, Oxford, 1995).

[27] Taylor, R., Hare, J. P., Abdul-Sada, A. K., Kroto, H. W., *J. Chem. Soc. Chem. Commun.* **(1990)**, 1423.

[28] Kawada, H., *et al. Phys. Rev. B.* **(1995)**, *51*, 8723.

[29] Niles, J. C., Wang, X. Q. *J. Chem. Phys.* **(1995)**, *193*, 7040.

[30] Negase, S. & Kobayashi, K. *Chem. Phys. Lett.* **(1994)**, *231*, 319.

[31] Diener M., D. & Alford, J. M. *Nature* **(1998)**, *393*, 668.

[32] Hummelem, J. C., Knight, B., Pavlovich, J., Gonzalez, R. & Wudl, F. *Science*, **(1995)**, *269*, 1554.

[33] http://www.electronicmaterials.ch.ic.ac.uk/ms/reserach.asp

[34] Chai, Y., *et al. J. Phys. Chem.* **(1991)**, *95*, 7564.

[35] Kadish, K. M. & Ruoff, R. S. Fullerenes, Chemistry, Physics and Technology (Wiley-Interscience, New York, 2000).

[36] Tellgmann, R., Krawez, N., Lin, S.-H., Hertel, I. V. & Campbell, E. E. B., *Nature* **(1996)**, *382*, 407.

[37] Murphy T., A., *et al. Phys. Rev. Lett.* **(1996)**, *77*, 1075.

[38] Harneit, W., *Phys. Rev. A.* **(2002)**, *65*, 32322.

[39] Iijima, S. *Nature* **(1991)**, *354*, 56.

[40] Baughman, R. H., *et al. Science*, **(2002)**, *297*, 787.

[41] Weisman, R., B. *Nature Mat.* **(2003)**, *2*, 569.

[42] Beton, P., H., Dunn, A. W. & Moriarty, P. *Appl. Phys. Lett.* **(1995)**, *67(8)*, 1075.

[43] Joachim, C., Gimzewski J. K., *Chem. Phys Lett.* **(1997)**, *265*, 353.

[44] Park, H., *et al. Nature* **(2000)**, *407*, 57.

[45] Licht, S., *et al. Sol. Energy Mater. Sol. Cells* **(1998)**, *51*, 9.

[46] Campbell, S. E., *et al. Nature* **(1996)**, *382*, 520.

[47] Regueiro, M. N., Monceau, P., & Hodeau, J-L. *Nature* **(1992)**, *355*, 237.

[48] Tutt, L. W. & Kost, A. *Nature* **(1992)**, *356*, 225.

[49] Meijer, M. D., Rump, M., Gossage, R. A., Jastrzebski, J. H. T. B. & van Koten, G. *Full. Sci. Techn.* **(1997)**, *5*, 1.

[50] Krätschmer, W., Lowell, D. L., Fostiropoulos, K., Huffman, D. R. *Nature* **(1990)** *347*, 354.

[51] Wang, P., Chen, B., Metzger, R. M., Da Ros, T., Prato, M., *J. Mater. Chem.* **(1997)**, *7(12)*, 2397.

[52] Zhou, D., Gan, L., Luo, C., Huang., C. & Wu, *Solid State Comm.* **(1997)**, *102*, 891.

[53] Frideman, S., *et al. J. Am. Chem. Soc.* **(1993)**, *115*, 6506.

[54] Sijbesma, R., et al., *J. Am. Chem. Soc.* **(1993)**, *115*, 6510.

[55] Karaulova, E. N. & Bagrii, E. I. *Russ. Chem. Rev.* **(1999)**, *68(11)*, 889.

[56] Chilstunoff J, Electrochemistry of Fullerene films, *Thin Solid Films* **(1995)**, *257*, 166.

[57] Koltun, M. *et al. Sol. Ener. Mater. & Sol. Cells.* **(1996)**, *44*, 485.

[58] Mirkin, C. *Tetrahedron* **(1996)**, *52*, 5113.

[59] Janda P *et al.*, *Adv. Mater.* **(1998)**, *10*, 17.

[60] Hou, J. G., *et al. Nature* **(2001)**, *409*, 304.

[61] Katz, E. A. *et al.*, *Thin Solid films* **(2000)**, *368*, 49.

[62] Barazzouk, S., *et al. Adv. Mater.* **(2001)**, *21*, 13.

[63] Lange, F. F. *Science* **(1996)**, *273*, 903.

[64] Von Blaaderen, A., Ruel, R., Wiltzius, P. *Nature* **(1997)**, *385*, 321.

[65] Trau, M., Saville, D. A., Aksay, I. A. *Science* **(1996)**, *272*, 706.

[66] Aizenberg, J., Braun, P. V., Wiltzius, P. *Phys. Rev. Lett.* **(2000)**, *84 (13)*, 2997.

[67] Hoogenboom, J. P., *et al. Nano Lett.* **(2004)**, *4(2)*, 205.

[68] Ruoff, R. S., Malhotra, R., Huestis, D. L., Tse, D. S. & Lorents, D. C. *Nature* **(1993)** *352*, 140.

[69] Scrivenns, W. A., Tour, J. M. *J. Chem. Soc. Chem. Commun.* **(1993)**, 1207.

[70] Ruoff, R. S., *et al. J. Phys. Chem.* **(1993)**, *97*, 3379.

[71] Heyman, D. *Fullerene Sci. Technology* **(1996)**, *5(1)*, 509.

[72] Friedman, H. *et al. J. Am. Chem. Soc.* **(1993)**, *115*, 6506.

[73] Scrivens, W. A., Tour, J. A., Creeck, K. E. & Pirisi L. *J. Am. Chem. Soc.*, **(1994)**, *116*, 4517.

[74] Alargova, R. G., Deguchi, S. & Tsujii, K. *J. Am. Chem. Soc.* **(2001)**, *123*, 10460.

[75] Holten, D., Edwards, P. P., Chemistry in Britain **(1985)**, 1007.

[76] Edwards, P. P. *Phys. Chem. Liq.* **(1981)**, *10*, 189.

[77] Edwards, P.P. *J. Superconductivity*, **(2000)**, *13*, 933.

[78] Mott, N. F., Metal-Insulator Transitions, (Taylor and Francis, London, 1990)

[79] Ogg, R. A. *Phys. Rev.* **(1946)**, *14*, 295.

[80] www.cmmp.ucl.ac.uk/~nts

[81] Wasse, J. C., Hayama, S., Skipper, N. T. & Fisher, H. E. *Phys. Rev. B.* **(2000)**, *61*, 11993.

[82] Wasse, J. C., Stebbings, S. L., Masmanidis, S., Hayama, S., Skipper, N. T. *J. Mol. Liq.* **(2002)**, *96*, 341.

[83] Wasse, J.C., Hayama, S., Skipper, N. T., Benmore, C. J. & Soper, A. K. *J. Chem. Phys.* **(2003)**, *118*, 7486.

[84] Buffinger, D. R., Ziebarth R. P., Stenger V. A., Recchia, C. & Pennington, C. H. *J. Am. Chem. Soc.***(1993)**, *115*, 9267.

[85] Thompson, H. *et al. J. Am. Chem. Soc.* **(2003)**, *125*, 2572.

[86] Hayama, S., Wasse, J. C., Skipper N. T. & Walters, J K. *Mol. Phys.* **(2001)** *99*, 779.

[87] Ricci, M. A., Nardone, F.P., Ricci, F. P., Andreani, C., Soper, A. K. *J. Chem. Phys* **(1995)**, *102*, 7650.

[88] Nicholls, D. Inorganic Chemistry in Liquid Ammonia, (Elsevier, Amsterdam, 1979).

[89] Lide, D. R., CRC Handbook of Chemistry and Physics (CRC Press, Inc. 1994).

[90] Herbard, A. F. *et al. Nature* **(1991)**, *350*, 600.

[91] Kortan, A. R. *et al. Nature* **(1992)**, *355*, 529.

[92] Özda, E. *et al. Nature* **(1995)**, *375*, 126.

[93] Zhu, Q. *et al. Nature* **(1992)**, *355*, 712.

[94] Cooke, S., Glenis, S., Chen, X., Lin, C., L. & Labes, M. M. *J. Mater. Chem.* **(1996)**, *6(1)*, 1.

[95] Fullagar, W. K., Reynolds, P. A. & White, J. W. *Solid. Stat. Commun.* **(1997)**, *104(1)*, 23.

[96] Schön, J. H., Kloc, CH. & Batlogg, B. *Nature* **(2000)**, *408*, 549.

[97] Schön, J. H., Kloc, CH., Siegrist, T., Steigerwald, M., Svensson, C., & Batlogg, B. *Nature* **(2001)**, *413*, 831.

[98] Degiorgi, L. *Adv. In Phys.* **(1998)**, *47*(2), 207.

[99] Margadonna, S. & Prassides, K. *J. Sol. Stat. Chem.* **(2002)**, *168*, 639.

[100] Rosseinsky, M. J. *Chem. Mater.* **(1998)**, *10*, 2665.

[101] Gunnarsson, O. *Rev. Mod. Phys.* **(1997)**, *69(2)*, 575.

[102] www.physik.uni-stuttgart.de/exphys/2.phys.inst./group/nmr/fullerene/fullerene_gallery.html

[103] Bardeen, J., Cooper, L. N. & Schreiffer, J. R. *Phys. Rev.* **(1957)**, *106*, 162.

[104] Ebbensen, T. W., *et al. Nature* **(1992)**, *355*, 620.

[105] Burk, B., Crespi, V. H., Zettl, A. & Cohen, M. L. *Phys. Rev. Lett.* **(1994)**, *72*, 3706.

[106] Schön, J. H., Kloc, CH. & Batlogg, B. *Science* **(2001)**, *293*, 2432.

[107] Grant, P. *Nature* **(2001)**, *413*, 264.

[108] Zhou, O. *et al. Nature* **(1993)**, *362*, 433.

[109] Zhou, O., *et al. Phys. Rev. B.* **(1995)**, *52*, 483.

[110] Margadonna, S., Prassides, K., Shimoda, H., Iwasa, Y. & Mezouar, M. *Europhys. Lett.* **(2001)**, *56*, 61.

[111] Margadonna, S., Aslanis, E. & Prassides, K. *J. Am. Chem. Soc.* **(2002)**, *124*, 10146.

[112] Squires, G., L., Introduction to the Theory of Thermal Neutron Scattering (Cambridge, New York, Cambridge University Press 1978).

[113] Soper, A. K., Howells, W. S. & Hannon, A. C. Atlas-Analysis Time-of-flight Diffraction data from Liquid and Amorphous Samples (Rutherford Appleton Laboratory Report RAL-TR-98-006, 1998).

[114] Kotlarchyk, M. & Chen, S-H. *J. Chem. Phys.* **(1983)**, *79(5)*, 2461.

[115] http://www.isis.rl.ac.uk/largescale/loq/documents/sans.htm

[116] Sun, Y. & Reed, C. A. *Chem. Commun.* **(1997)**, 748.

[117] Rao, A. M. *et al. Science* **(1993)**, *259*, 955.

[118] Kroto, H. W., Allaf, A. W. & Balm, S. P. *Chem. Rev.* **(1991)**, *91*, 1213.

[119]www.isis.rl.ac.uk

[120] Benmore, C. & Soper, A. K., The SANDALS Manual, Rutherford Appleton Laboratory Technical Report (RAL-TR-89-046).

[121] Turner, J. Z., Soper, A. K., Howells, W. S., Hannon, A. C., & Ansell, S. SANDALS Survival Guide (ISIS Facility, RAL, 1995).

[122] http://www.isis.rl.ac.uk/disordered/Manuals/gudrun/gudrn_GEM.htm

[123] Placzek, G. *Phys. Rev.* **(1952)**, *86*, 377.

[124] http://www.ill.fr/YellowBook/D22/

[125] Dewhurst, C. GRASP User Manual (Institut Laue Langevin, Grenoble, France, 2003).

[126] Skipper, N. T. *MONTE User's Manual.* Technical Report, Department of Chemistry, University of Cambridge, UK.

[127] Park, S-H. & Sposito, G. *Phys. Rev. Lett.* **(2002)**, *89(8)*, 85501.

[128] De Carvalho., R. J. F. & Skipper, N. T. *J. Chem. Phys.* **(2001)**, *114(8)*, 3727.

[129] Wasse, J. C., Howard, C. A., Thompson H., Skipper, N. T., Delaplane, R. G. & Wannberg, A. *J. Phys. Chem.* **(2004)**, *121(2)*, 996.

[130] Soper, A. K. *Chem. Phys.* **(1996)**, *202*, 295.

[131] Soper, A. K. *Mol. Phys.* **(2001)**, *99*, 1503.

[132] Soper, A. K. & Bowron, D. T., *EPSR – A User's Guide*

[133] Dixit, S., Crain, J., Poon, W. C. K., Finney, J. L. & Soper, A. K. *Nature* **(2002)** *416*, 829.

[134] Dixit, S., Soper, A. K., Finney, J. L. & Crain, J. *Europhys. Lett.* **(2002)**, *59(3)*, 377.

[135] Thompson, H., Wasse, J. C., Skipper, N. T., Howard, C. A., Bowron, D. T. & Soper, A. K. *J. Phys.: Condens. Matter* **(2004)** *16*, 5639.

[136] Bowron, D. T., Finney, J. L. & Soper, A. K. *J. Phys. Chem. B.* **(1998)** *102*, 3551.

[137] Botti, A., Bruni, F., Imberti, S. & Ricci, M. A. **(2004)**, *120(2)*, 10154.

[138] Soper, A. K., (Local Structure from Diffraction, ed. Billinge, S. J. L. & Thorpe, M. F. Plenum Press, New York, 1998)

[139] Allen, M. D. & Tildesley, D. J. *Computer Simulation of Liquids*, OUP, Oxford, (1987).

[140] ISIS Experimental Report, RAL, RB12053.

[141] Soper, A. K., in Neutron Scattering Data Analysis 1990, pp. 57-67, edited by Johnson, M. W. (IOP Conference Series Number 107, IOP Publishing, Bristol, 1990).

[142] Salmon, P. *Proc. Roy. Soc. A.* **(1994)**, *445*, 351.

[143] Rizzo, R. C. & Jorgensen, W. L. *J. Am. Chem. Soc.* **(1999)** *121*, 4827.

[144] Chandrasekhar, J., Spellmeyer, D. & Jorgensen, W. L. *J. Am. Chem. Soc.* **(1984)**, *106*, 903.

[145] Åqvist, J. *J. Phys. Chem.* **(1990)**, *94*, 8021.

[146] Guo, Y. J., Karasawa, N., Goddard, W. A. *Nature* **(1991)** *351*, 464.

[147] Bowron, D. T. & Finney, J. L. *J. Chem. Phys.* **(2003)**, *118(18)*, 8357.

[148] Wasse, J. C., Hayama, S., Skipper, N. T., Benmore, C. J. & Soper, A. K. *J. Chem. Phys.* **(2000)** *112*, 7147.

[149] Eastoe, J., Esther, R. C., Beeby, A. & Heenan, R. K. *Chem Phys. Lett.* **(1995)**, *245*, 571.

[150] Affholter, K. A. *et al. J. Chem. Phys.* **(1993)**, 99(11), 9224.

[151] Heenan, R. K. The "Fish" Reference Manual (Rutherford Appleton Laboratory Report RAL 89-129, 2001).

[152] ISIS Experimental Report, RAL, RB13345.

[153] Finney, J. L., Bowron, D. T., Daniel, R. M., Timmins., P. A. & Roberts, M. A. *Biophys. Chem.* **(2003)**, *105*, 391.

[154] Girifalco L. A. *J. Phys. Chem.* **(1992)**, *96*, 858.

[155] Klein, M. L. & Cheng, A. *J. Phys. Chem.* **(1991)**, *95*, 6750.

[156] Abramo, M. C., Caccamo, C., Costa, D., Pellicane, G. & Ruberto, R. *Phys. Rev.E.* **(2004)**, *69*, 31112.

[157] Burgess, J. Ions in Solution, (Horwood Publishing Ltd., Westergate, 1999).

[158] Murphy, D. W., et al. *J. Phys. Chem. Solids.* **(1992)**, *53*, 1321.

[159] Kuntscher, C. A., Bendele G. M. & Stephens, P. W. *Phys. Rev. B*, **(1997)**, *55(6)*, 3366.

[160] Touzik, A., Hermann, H. & Wetzig, K. *Phys. Rev. B.*, **(2002)**, *66*, 75403.

[161] Oszlànyi, G. *et al. Phys. Rev. Lett.* **(1997)**, *78*, 4438.

[162] Oszlànyi, G. *et al. Phys. Rev. B.* **(1998)**, *58*, 5.

[163] Wågberg, T., Stenmark, P. & Sundqvist, B. *J. Phys. Chem. Solids.* **(2004)**, *65*, 317.

[164]Pennington, C. H. & Stenger, V. A. *Rev. Mod Phys.* **(1996)**, *68(3)*, 855.

[165] Johnson, R. D. *et al. J. Am. Chem. Soc.* **(1990)**, *112*, 8983.

[166] Ajie, H. *et al. J. Phys. Chem.* **(1990)**, *94*, 8930,